HEAT TRANSFER DURING SPRAY WATER COOLING
USING STEADY EXPERIMENTS

BY

XIAOXU ZHOU

THESIS

Submitted in partial fulfillment of the requirements
for the degree of Master of Science in Nuclear Engineering
in the Graduate College of the
University of Illinois at Urbana-Champaign, 2009

Urbana, Illinois

Master's Committee:

Professor Brian G. Thomas; Chair
Professor David N. Ruzic

HEAT TRANSFER DURING SPRAY WATER COOLING
USING STEADY EXPERIMENTS

Xiaoxu Zhou, MS.
Department of Nuclear, Plasma and Radiological Engineering
University of Illinois at Urbana-Champaign, 2009
Brian G. Thomas, Adviser

Spray water cooling is widely used in many industrial processes to control heat removal from a hot material surface. In order to control heat transfer rates and obtain desired surface temperature distributions, a deeper understanding of fundamental spray cooling dynamics and more accurate estimation of spray heat transfer rates is needed. In this thesis, a new technique combining experiment and computational modeling has been developed for measuring the steady-state heat transfer extracted locally by water sprays or air-mists impinging on the surface of a hot metallic sample.

The experimental apparatus was developed by A. C. Hernandez B., H. Castillejos E, and F. A. Acosta Gat CINVESTAV, Mexico, and is designed to be able to employ spray water to cool the metallic sample accommodated inside a copper coil with an alternating current as induction heating goes on inside the sample. Control of total input power from the wall maintains each desired sample thermocouple temperature. A computational model developed using the commercial finite-element package COMSOL Mutiphysics uses a two-dimensional axisymmetric model of the electromagnetics and heat-conduction equations to balance the heat extracted from the sample surface by the boiling water droplets. Measurement of the RMS current flowing through the copper coil enables the model to estimate the heat extracted to the cooling spray by matching the sample thermocouple temperature measurement. Heat transfer coefficients and fluxes are quantified for spray cooling of a platinum sample at temperatures ranging from 100-1200°C, using typical air-mist nozzles and conditions relevant to steel

continuous casting, and also compared with transient measurement results of spray cooling and Nozaki empirical correlation. The results reveal the flexibility of the technique to investigate different aspects of spray cooling. The spray heat transfer coefficients extracted range from 1 kW/m^{2}K to 27kW/m^{2}K, and heat fluxes rang from 0.5MW/m^2 to 5MW/m^2 as the sample surface temperature varies from 80°C to 1185°C Heat removal hysteresis exists during the spray heating-cooling cycle. The Leidenfrost temperature is found to be around at 850°C.

ACKNOWLEDGEMENT

TABLE OF CONTENTS

List of Tables

List of Figures

x

Nomenclature

A :   Nozaki Correlation Coefficient

$\vec{A}$:   Magnetic Vector Potential

$\vec{A}_0$:   Magnetic Vector Potential Magnitude

$\vec{A}_1$:   Magnetic Vector Potential by Gauge Transformation of $\vec{A}$

$\vec{B}$:   Magnetic Field

C_p :   Specific Heat

$\vec{D}$:   Electric Displacement Field

$\vec{E}$:   Electric Field

f :   Scalar Function / Alternating Electromagnetic Field Frequency

h_{spray} :   Spray Heat Transfer Coefficient

$\vec{H}$:   Magnetic Flux Intensity

j :   Imaginary Unit

$\vec{J}_{ext}$:   External Current Density

$\vec{J}_{ext0}$:   External Current Density Magnitude

$\vec{J}_f$:   Free Current Density

k :   Thermal Conductivity

Q :   Heat Generation Source

Q_w :   Spray Water Flux Rate

t :   Time

T :   Temperature

Ts: Sample Thermocouple Temperature

T_{spray} :   Spray Temperature

V :   Voltage Drop

X: Vertical Direction for Nozzle

Y: Horizontal Direction

Z: Direction along Nozzle

ε_0 :   Free Space Permittivity

ε_r :   Relative Permittivity

μ_0 :   Free Space Permeability

μ_r :   Relative Permeability

ρ :   Density

ρ_f :   Free Charge Density

σ :   Electrical Conductivity

σ_{Pt} :   Platinum Electrical Conductivity

Φ :   Scalar Potential

Φ_0 :   Scalar Potential Magnitude

Φ_1 :   Scalar Potential by Gauge Transformation of Φ

ω :   Alternating Electromagnetic Field Angular Frequency

Chapter 1: Introduction

Spray water cooling has been extensively used in industrial processes, such as steel surface temperature control in continuous casting, rapid cooling of a reactor pressure vessel head in a boiling water reactor, thermal management of electronic devices, titanium alloy machining and aluminum DC casting, to control heat removal from a hot metallic body surface. It features both high efficiency and great flexibility of heat removal.

1.1 Spray Cooling in Secondary Cooling Region of Continuous Casting

Continuous casting transforms molten steel to solid on a continuous basis. Fig. 1.1 shows a schematic of the continuous casting process. Molten steel comes out of the tundish through a nozzle and starts to solidify against mold which is cooled by water flowing through the mold channels. Then the solidified steel shell is pulled down by driven rolls to the secondary spray cooling region to experience further heat treatment until the steel slab solidifies completely [1].

The secondary cooling region achieves steel quality by adjusting spray nozzle operation conditions to obtain a desired strand surface temperature history. It would be helpful to experimentally measure strand surface temperature by pyrometer or other advanced devices. Knowing surface temperature, operators or automated control systems could adjust corresponding spray nozzles conditions to maintain the surface temperature in the desired range. However, real practice present difficult problems associated with the measurement of the strand temperatures. During continuous casting, spray water impinges onto the strand surface and a lot of steam is generated which fills the space around the steel slab due to the high temperature of the steel surface. This steam absorbs some of the light emitted from the steel surface. In addition, scale on the strand surface changes the emissivity. Therefore, the temperature recorded by

pyrometers is often lower than reality. In real casting, the steel slab in the secondary spray cooling region is usually supported by a number of rolls and sprayed by a large number of rows of spray nozzles. Much space is taken by those rolls and nozzles so the space for installation of measurement devices such as pyrometers is unfortunately limited. Thus, it is difficult and expensive to obtain the temperature distribution along the strand surfaces. Only a few temperatures at limited locations are available, which are even unfortunately not reliable. Therefore, there is great demand by steel companies to investigate and quantify spray heat transfer behavior, to implement appropriately the heat transfer information into computational models, to make good predictions of the strand surface temperatures and to validate them by industrial trials.

One of most important aspects related to the adjusting of spray nozzle operation conditions is the spray heat transfer coefficient or spray heat flux extracted from steel strand surface. Accurate control of surface temperature requires systematic understanding of fundamental spray heat transfer behavior both in steady and transient state and accurate quantification of spray heat transfer coefficients for different surface temperature, different surface roughness, different nozzle operation conditions and different nozzle geometry, etc. However, measuring heat transfer coefficients during spray cooling is difficult, and there is a lack of data. To accurately quantify heat transfer during spray cooling, it is essential to have both good spray cooling experiments with accurate measurements, as well as a good computational model of the experiment to extract the coefficients.

1.2 Spray Cooling in Nuclear Engineering

Light water nuclear reactors (LWR) or nuclear pressurized water reactors are usually installed with containment spray systems [2, 3]. The purpose of the containment spray system is to operate during a severe accident, e.g. loss of coolant accident, in a nuclear power plant. It should depressurize the containment by steam condensation on spray droplets, to reduce the risk of hydrogen burning by mixing into the containment atmosphere, and to collect radioactive aerosols from the containment atmosphere. Regarding this application, a lot of experimental and numerical work on spray dynamics, such as direct contact condensation of steam on droplets, droplets size and droplets temperature history, has been done by many researchers [4-14] .

The other application of spray system is to speed up the cooling of the pressure vessel head. After shutdown of a boiling water reactor to "cold standby", the upper head of the reactor pressure vessel (RPV) can be removed if its temperature is below a prescribed limit value. The spray system is installed inside of the pressure vessel head. The spray system in the RPV head is providing streams of subcooled droplets flowing out through nozzles located at a certain distance from the RPV inner walls. The cooling of walls in the RPV is initiated by impinging droplets and then continued by liquid film falling down along the walls due to gravity forces [15].
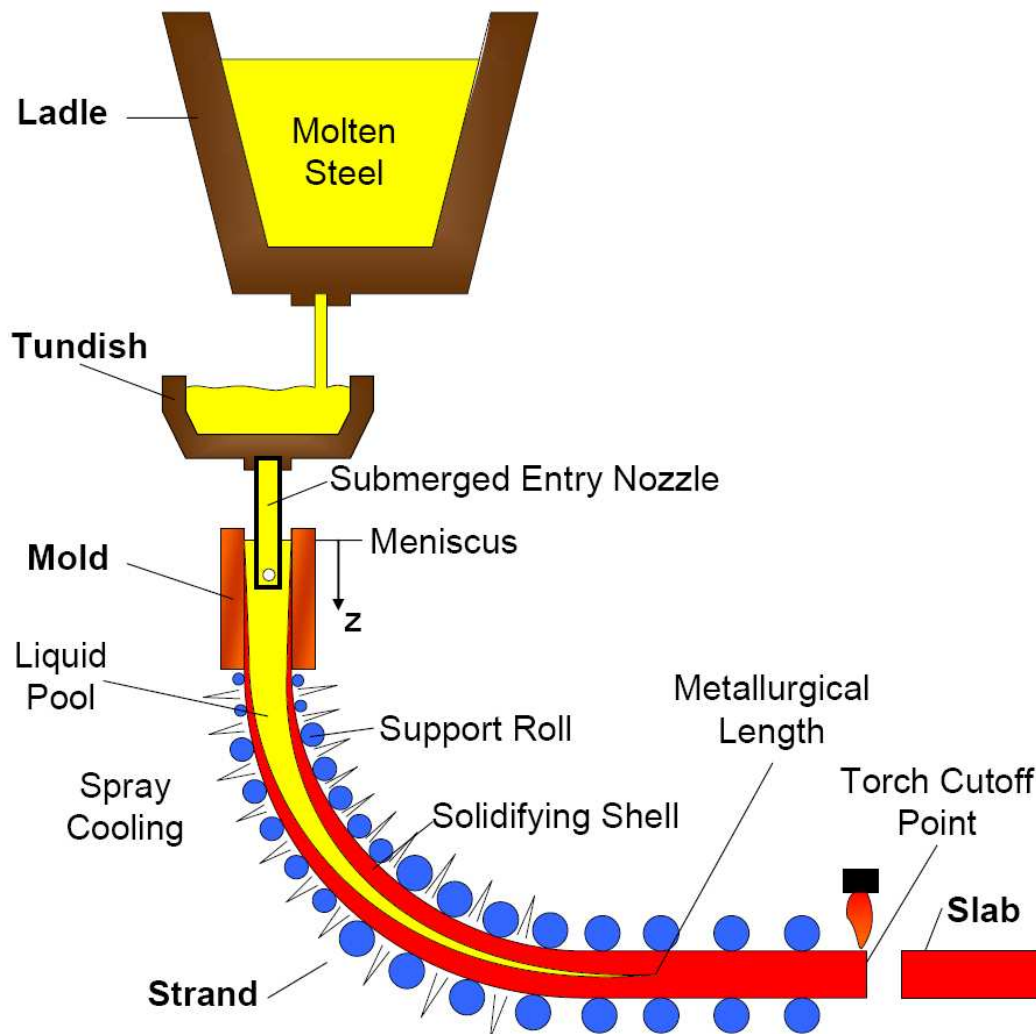
Fig 1.1 Schematic of Continuous Casting [16]

Chapter 2: Literature Review

2.1 Previous Spray Dynamics Investigation and Spray Cooling Experiments

Spray cooling is a technology of increasing interest for electronic cooling, continuous casting secondary cooling and other high heat flux removal applications, and is characterized by high heat transfer, uniformity of heat removal, small fluid inventory, low droplet impact velocity and no temperature overshoot. The mechanisms by which heat is removed during spray cooling are poorly understood, however, due to the complicated spray dynamics, various material surface conditions and its dependence on many parameters that are not easily varied independently. Thus spray cooling is difficult to predict.

Spray dynamics has been investigated by many researchers. McGinnis [17] and Pedersen [18] reported that there is a direct dependency of the heat transfer on the droplet diameter and its initial collision velocity. Wachters [19] found that from low to high Weber number there is a transition from non-wetting to wetting impact for single drops. Choi and Yao [20] investigated the effect of the Weber number on the impaction heat transfer. Sozbir et al. [21] indicated that as the droplets impact the surface with more momentum and the water mass flux increases the Leidenfrost temperature increases. Leidenfrost temperature [22] is the temperature at which boiling curve gives minimum-heat-flux point, as shown in Figure 2.1. Buyevich and Mankevich [23] proposed a model to calculate the critical normal velocity of a single drop which defines if the impinging droplet is either captured by the surface and ultimately evaporated or almost elastically thrown without removing heat. Hatta et al. [24-26] developed mathematical models to describe the velocity and trajectory of drops in mist jets. Hernandez et al. [27] developed a CFD model for simulating the motion of the water droplets and air emerging as a mist from a nozzle under conditions of interest to continuous casting.

Direct experiments measuring spray heat transfer rates have also been investigated by many researchers. Shimada and Mitsutsuka [28] proposed an empirical correlation to predict the spray heat transfer coefficient from the spray flow rate and spray temperature, for nozzles used in secondary cooling in casting. Nozaki [29] introduced an empirical adjustment coefficient to the Mitsutsuka correlation based on in-plant temperature measurements at the straightener. Brimacombe et al. [30] measured heat transfer rates in the secondary cooling zone of any operating continuous steel caster. Sengupta et al. [31] noted that the maximum heat flux and minimum heat flux (Leidenfrost temperature) in these boiling curves for steel casting (600 $^{\text{o}}$C and 1000 $^{\text{o}}$C) are at much higher temperatures than for DC casting of Aluminum (200 $^{\text{o}}$C and 380 $^{\text{o}}$C). Yu [32] presented heat fluxes during quenching 7055 alloy samples in coolant water and in coolant water with oxidization inhibitor. It demonstrated that the heat transfer from the samples bearing the oxidization inhibitor on their surfaces is significantly greater than that of no oxidization inhibitor control. More recently, Choi and Yao [33] studied heat transfer from horizontal sprays. Maximum heat fluxes of up to 2MW/m^2 were measured for wall temperatures of 140 $^{\text{o}}$C ~160 $^{\text{o}}$C, while Leidenfrost temperature was about 250 $^{\text{o}}$C. Mizikar [34] studied three full-cone nozzles, with mass flux up to 19 kg/m^{2}sec, using a stainless steel test sample. The heat transfer coefficient was found to be a linear function of water flux. The angle of spray attack was also studied and it was concluded that angle of spray has a negligible effect on heat transfer rate. In the study of Ciofalo [35], the reported heat transfer rates are much higher than other authors for tests at the same mass flux. More recently, Al-Ahamdi and Yao [36] conducted experimental tests for a cylindrical plate of stainless steel and found that heat transfer is primarily dependent on the local mass flux, and the overflow of the residual water from upstream induces slightly higher heat fluxes and higher Leidenfrost temperature. All these experiments are transient. The

application of steady state techniques is severely limited by the maximum attainable power densities and difficulties in maintaining steady state conditions.

The aim of this work is to design a steady apparatus to measure spray heat transfer rates under various nozzle operating conditions and wide rage of sample surface temperature.

2.2 Previous Modeling of Heat Transfer with Induction Heating

Induction heating is widely used in many industries, in operations such as metal melting, metal hardening, preheating for forging operations, brazing, crystal growing, semiconductor wafer processing, high-speed sealing and packaging, and curing of organic coatings, thanks to its favorable features of fast heating rate (6000 F/s in foils), instant start/stop, precise heat pattern and non-contact heating. It is a complex process involving both electromagnetic and thermal phenomena, which involve eddy current (or electromagnetic field) distribution inside conductive materials and heat generation by Joule heating and heat transfer. The theory of induction heating mainly involves low-frequency Maxwell equations, charge continuity equation, Ohm's law and energy balance equation. Since all of these equations were clear to engineers and scientists, analytical solutions and numerical solutions to specific problems have been proposed and applied.

In 1967, Dodd and Deeds [37] obtained analytical solutions to an electromagnetic field in an infinitely long cylinder of constant permeability when heated by a single circular coil and also under a coil suspended above a half-space of constant permeability. However, due to the high complication in geometry and governing equations of typical induction heating systems, numerical methods instead of analytical solutions were developed by many researchers and applied to model various induction heating problems. Finite element methods were used by Donea et al. [38] and Chari [39] to obtain the electromagnetic vector potential for some

axisymmetric and two-dimensional problems. Meunier et al. [40] calculated the electromagnetic field in the same two-dimensional and axisymmetric configurations for different conditions of supply voltage and current applied to a coil using finite element analysis.

Some models went beyond a calculation of the electromagnetic field. The problem of calculating the temperature distribution in an inductively-heated workpiece was addressed by Baker [41] for one-dimensional heat flow problem. A two-dimensional finite element program for magnetic induction heating was developed by Marchand et al. [42] to solve the non-linear electromagnetic problem in axisymmetric induction heating devices. An efficient finite element procedure was developed for the analysis of induction heat treatment problems involving nonisothermal phase changes by Wang et al. [43]. A mathematical model using the standard finite element method was developed by Chaboudez et al.[44] to deal with numerical simulations of induction heating for axisymmetric geometries. Other applications involving three-dimensional numerical modeling can be found in papers by Jafrai-Shapoorabdi et al [45] and Kim [46]. By now, numerical techniques to solve various induction problems is a mature field and the methods have been integrated into many commercial packages such as ANSYS [47] and COMSOL [48].

2.3 Objectives of the Current Work

Heat removal from a hot metallic body surface is complicated. As shown in Figure 2.1 for a typical pool boiling curve, heat transfer experiences four stages: convection, nucleate boiling, transition boiling and film boiling, as the metallic body surface temperature increases. In the nucleate boiling regime, as the surface temperature increases, heat transfer rate increases due to the rapid increase in the number of active nucleation sites where bubbles can form, departure

and taking heat out. This stage goes until it reaches a peak heat flux rate, the vapor streams moves upward so fast that the liquid downflow to the surface is unable to sustain a higher evaporation rate and a layer of vapor forms. Further increase of temperature decreases heat transfer rate due to the low thermal conductivity of the thickening vapor layer. At the Leidenfrost temperature, the lowest heat flux is reached, which is also called Leidenfrost effect. Above the Leidenfrost temperature, radiation becomes significant and heat flux goes up [49].

The vapor layer, which plays a major role in Leidenfrost effect, takes time to form. In previous transient experiments [50], metallic surfaces experienced fast cooling (~30°C/s) with gradually establishing a vapor layer at high temperature and layer vanishing at low temperature. Surface temperature and heat transfer conditions between the coolant and the metallic surface were changing simultaneously. Therefore, the heat flux extracted from the experiments involved a complex spray dynamics process. It is very difficult to identify how spray heat removal rate changes only with surface temperature in transient experiments. To gain this understanding, it is necessary to study surface temperature effect and vapor effect on spray heat transfer rate individually.

The objective of this work is to develop a controlled laboratory apparatus to maintain a specified metallic surface temperature for a long time by a power controller in order to obtain stable heat transfer condition between the coolant and the surface. Then, a computational model is to be developed and used to calculate spray heat removal rate. Finally, spray heat flux for the surface temperature ranging from 100 ^{o}C to 1200°C is to be obtained using this methodology for a typical nozzle used in a continuous casting spray zone.

Figures
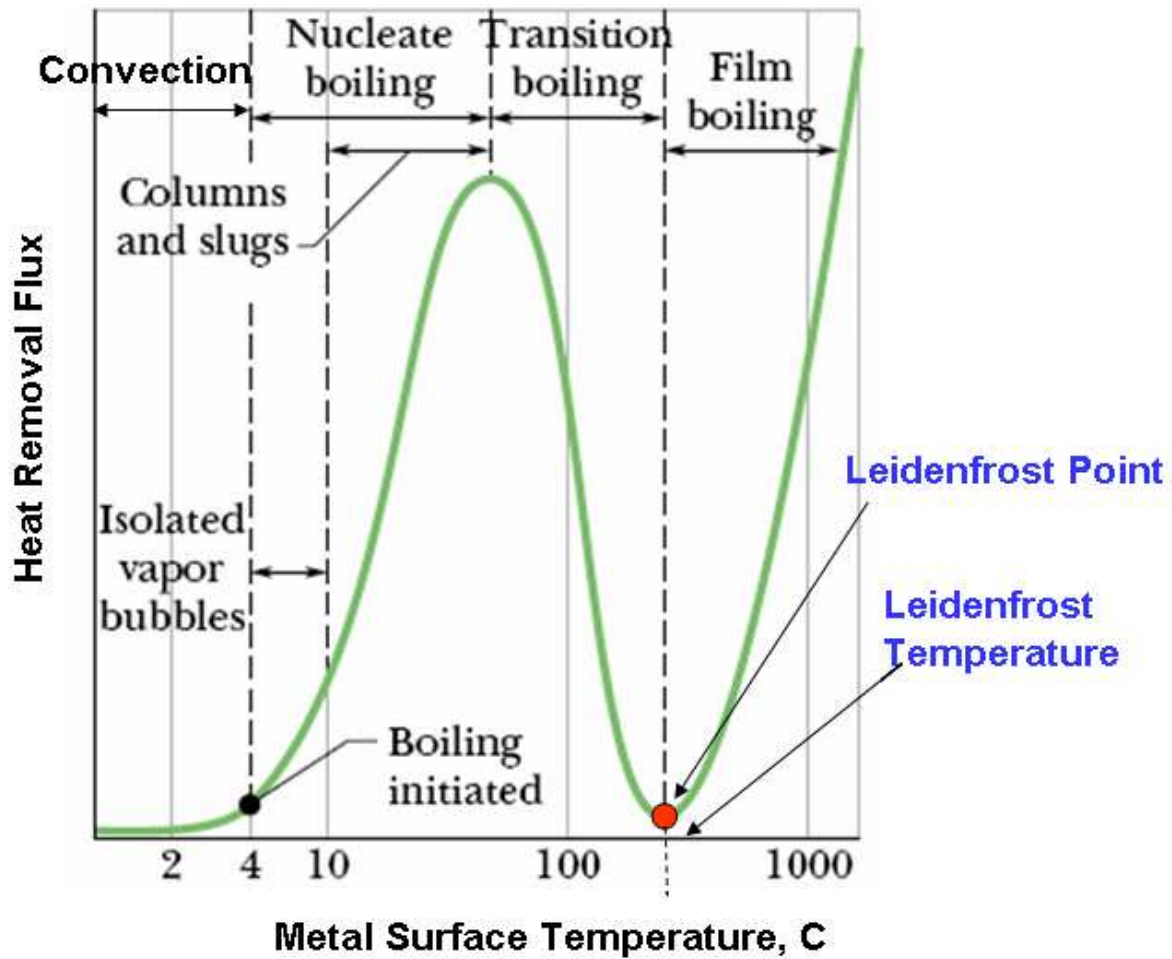
Fig. 2.1 Typical Pool Boiling Curve Showing Different Regimes of Heat Transfer [51]

Chapter 3: Measurements Using Steady Experimental Apparatus

3.1 Experimental Apparatus Setup

The steady-state measurement of spray water cooling heat transfer in this work is performed at the Laboratory of Process Metallurgy at CINVESTAV, Ramos Arizpe, Mexico. A complete 3D schematic of the experimental apparatus is shown in Figure 3.1. The entire experimental measurement system consists of:

- a cooling water reservoir and a pump, which stores water and drives it to cool the entire high frequency generator system;

- power generator, which supplies and controls power for induction heating;

- cooling water flow rate reader, which records the flow rate of cooling water;

- temperature monitor, which records and monitors the sample thermocouple temperature;

- thermocouples, which record temperatures at specified locations;

- induction copper coil, which induces eddy current in the sample and heats it up;

- ceramic body, which accommodates the induction coil and the sample;

- plastic cylinders, which prevent ceramic body from spray water cooling;

- quartz glass window, which also prevents ceramic body from spray water cooling;

- ammeter, which records the total current going through the induction coils;

- nozzle, which provides water spraying;

- data acquisition system, which collects and stores experimental data.

This system starts initially with starting the pump. The cooling water is pumped out of the cooling water reservoir to flow through the whole system, cooling the electric and electronic circuits of the power generator and the induction copper coil. The cooling water flow rate through the copper coil can be read from the water flow rate reader. Two K-type thermocouples

are installed inside the pipes to measure the cooling water temperature going out of and entering the reservoir. The cooling water flow rate and these two measured temperatures are used to estimate the cooling water heat transfer coefficient inside the copper coil.

A cylindrical platinum sample that is 8mm in diameter and 2.5mm in height is accommodated inside a cylindrical ceramic body with a copper coil going around. This copper coil provides induction heating with a 2.53kHz alternating current going through it. Figure 3.2 shows the induction copper coil which is machined to have two loops, separated by around 0.5mm apart. The coil is flat if seen from the top and half circular if seen from the front. The assembly of the platinum sample, copper coil, ceramic body and a plastic cylinder is clearly shown in Figure 3.3. The plastic cylinder is designed to keep the sample dry, so that there is no uncontrolled heat loss from leaking water. A R-type thermocouple is welded to attach it to the center of the platinum sample back surface and used to measure the platinum temperature which is called sample thermocouple temperature (Ts). Another two K-type thermocouples are installed at 11.5mm and 27.5mm, respectively, from the sample frontal surface along the axisymmetric line of the ceramic body. The wires of three thermocouples go through the ceramic body and come out of the back surface.

The plastic cylinder accommodating the sample, copper coil and ceramic body is covered by another plastic cylinder. The front of the ceramic is covered by a circular quartz glass window, as shown in Figure 3.4, which resists high temperature, with a circular hole a little bit larger than the sample. This hole is machined to allow the spray to reach the sample frontal surface while preventing spray from reaching elsewhere of the ceramic body. The complete experimental assembly is shown in Figure 3.5. The employment of double plastic cylinders and quartz glass

window ensures the ceramic body and induction copper coil is kept away from being spray cooled.

An ammeter, as shown in Figure 3.1, is attached to the coil after it comes out of the ceramic body and is used to measure the total RMS current going through the coil. This measurement of total current can be used to calculate the heat generated by induction for computational modeling. Heat is generated both inside the sample and copper coil, while the sample frontal surface is cooled using spray water ejected by a Delavan nozzle. The nozzle, as shown in Figure 3.5, is mounted 190mm directly towards the sample frontal surface and it is movable along both horizontal (Y direction) and vertical (X direction) directions and also back and forth (Z direction). This flexibility allows convenient adjusting of nozzle position respect to the sample. The specific water and air flow rates through the nozzle are obtained by manual controlling of valves installed at the water and air pipes.

The following measurements are collected and recorded by a data acquisition system consisting of analog/digit transformer, personal computer and LabView, as shown in Fig. 3.1.

- Total applied input power,
- Two thermocouples inside the cooling water pipe, measuring water temperature difference between entering and leaving the coil,
- Two thermocouple measurements of the ceramic body,
- Thermocouple measurement of the sample,
- Cooling water flow rate,
- Total current through the copper coil,
- Water and air flow rates for the nozzle,
- Water and air pressures for the nozzle.

3.2 Nozzle and Spray Characteristics

The nozzle employed during the experiments reported here was manufactured by Delavan Spray Technologies of Goodrich Company. It is a W19822 type nozzle, shown in Figure 3.6, which is designed to produce a rectangular flow pattern with an obelisk impact density distribution. Also presented in Figure 3.6 are three locations, where the sample was positioned, to investigate heat transfer rate behavior along spray length (Y direction).

The water flux rates at these three locations are shown in Figure 3.7. These flux rates were obtained in the following way. First, the nozzle was aligned using a laser to orient its center axis with a tube located at (0, 0mm) in the transverse plane (replacing the sample)., The tube had the same 4-mm diameter as the sample and was connected to a bottle which collected the water spray that impacted and entered the tube for 3 min. for a specified set of nozzle operating conditions (nozzle water flow rate and air flow rate). The water flux rate was obtained by dividing the volume of the collected water by the operating time and the tube cross section area. The tube was moved to two other locations (9mm, 18mm), moving in the width direction (perpendicular to the fan-shaped spray jet), and the water flux rates were measured the same way. For the nozzle water flow rate of 3.5 lpm, only the 0mm location was measured.

As expected, water flux rate decreases as the tube (or sample) is moved away from the spray center line in the Y direction. The water flux rates measured here repeat part of the complete footprint measurements of water flux rate obtained by Vapalaphti and et al. such as shown in Figure 3.8 for two different operating conditions[50]. For details of these experimental measurements, please refer to the reference 50. The footprint pattern is highly dependent on water and air pressures in addition to fluid flow rates, which dominate the formation of droplets, the number of droplets, droplet velocity and droplet size distributions. Note that the footprint

pattern is not symmetrical, and the three points in this work appear to be in the low-flux side. The results are consistent, however. The spray jet width of ~20mm in Figure 3.8 is consistent with the very-low water flux rate measured in the current work. Values are roughly 2.5 times smaller than in the previous work, which is consistent, considering the 2.3 times lower total water flow rates. All these parameters characterize air-mist or water spray dynamics and play a major role in spray heat transfer. Heat transfer coefficients were extracted from wet experiments for various nozzle operating conditions, then correlated with nozzle flow rates and flow pressures to quantify the spray dynamics. The three sample locations are also labeled in Figure 3.8(a).

3.3 Experimental Procedure

Two types of heat transfer experiments are performed independently with the apparatus described in Section 3.1: dry experiments to check and calibrate the system, and wet experiments to measure spray cooling heat transfer.

Dry experiments are done without air-mist spray coming out of the nozzle. The sample front surface experiences only natural convection and thermal radiation. It requires less power in induction heating due to small heat extraction ability from the sample front surface compared to wet experiment. Therefore, the signals of total current and sample thermocouple temperature are more stable. Figure 3.9 shows a typical sample thermocouple temperature and corresponding total current histories in a dry experiment. To run a measurement, the operator first enters a desired sample thermocouple temperature into the sample thermocouple temperature monitor. Then the power generator machine responds and adjusts the power demanded in induction heating to maintain the sample thermocouple at the specified temperature. The sample is firstly heated from 200 ^{o}C to 1200 ^{o}C and then cooled down from 1200 ^{o}C to 200 ^{o}C in steps of 100 ^{o}C

in a complete heating-cooling cycle. At each sample thermocouple temperature, 5min is allowed for the sample to reach thermal stabilization. As shown in Figure 3.9, the total measured currents are very close to each other for the same sample thermocouple temperatures during both heating and cooling. There is no hysteresis in the RMS current measured.

Wet experiments are done with air-mist spray coming out of the nozzle, impinging upon the exposed front surface of the Platinum sample, and extracting heat. The sample thermocouple temperature entered into sample thermocouple temperature monitor ranges from 200 ^{o}C to 1200 ^{o}C. As before, the sample is firstly heated from 200 ^{o}C to 1200 ^{o}C and then cooled down from 1200 ^{o}C to 200 ^{o}C at steps of 100 ^{o}C in a complete heating-cooling cycle. Therefore, twenty three sample thermocouple temperatures are examined for each nozzle operating condition in wet experiment. Figure 3.10 shows a typical sample thermocouple temperature history as well as the measured RMS current. The blue stairway-like curve shows the sample thermocouple temperature while the pink curve shows the total measured current. As shown in Figure 3.10, the total current during heating is a lot higher than during cooling for the sample thermocouple temperatures ranging from 200 ^{o}C to 700 ^{o}C.

As mentioned above, there is no current hysteresis in the dry experiments. This indicates that this hysteresis comes out of the spray heat transfer dynamics, which sequentially introduces a hysteresis in the RMS current. As the sample thermocouple temperature displayed in the monitor is tuned to a new one from a previous temperature, it usually takes 25s to reach the target temperature, while the total current overshoots, comes back after about 20s and then becomes stable. Eight minutes are spent for each sample thermocouple temperature in ensuring the sample to reach steady state. Two examples of zoom-in graphs are given in Figure 3.11 and 3.12. The overshooting during heating and undershooting during cooling of the total current is

obvious at these low sample thermocouple temperatures. For the example of heating, the controller tries to heat the sample to the target temperature of 300 ^{o}C set by the operator. Firstly, the controller supplies a larger power to heat up the sample from 200 ^{o}C to 300 ^{o}C. Then, the sample heats up so quickly and easily that the controller finds the sample does not need so much power and decides to decrease the input power to induction heating. Therefore, overshooting of the total power comes along with this control process. After overshooting, the total current decreases gradually and reaches steady state. It is also obvious that the sample thermocouple temperature and the total current approach steady state near the end of stage at each sample thermocouple temperature.

Figure 3.13 shows the corresponding measurements of the nozzle water flow rate, air flow rate, water flow pressure and air flow pressure for the example wet experiment described in the above section. The water flow rate and air flow rate were manually controlled during the experiment. Compared to the air flow rate, the water flow rate (4.6lpm) is relatively more stable. Every time after the air flow rate was adjusted to 104 lpm, it kept increasing gradually. The air flow rate was then adjusted back to 104 lpm shortly after each step change in sample thermocouple temperature. Therefore, the jumps in the current and the air flow rate appear to roughly coincide. The signals of water and air flow pressures are affected by adjusting the air flow rate and both show similar shapes to that of the air flow rate..

3.4 Completed Experiments

The experiments with different nozzle operating conditions completed during June 2009 at the Laboratory of Process Metallurgy at CINVESTAV, Mexico are shown in Table 3.1. Eight cases have been done. The dry experiment was done with the nozzle water completely off. The

wet experiments were preformed by orienting the W19822 nozzle at three different locations relative to the sample for three different nozzle operating conditions. Complete details for cases 1 and 4 were presented in the previous section. The measured RMS current, total power and sample thermocouple temperature for each case (1~8) are presented in the graphs and attached in Appendix A. For cases 1-4, the sample thermocouple temperature was increased from 30°C to 1200 ^{o}C (heating), and then cooled, as mentioned previously. For cases 5-8, the sample thermocouple temperature was adjusted from 1200 ^{o}C to 30 ^{o}C at the end of the heating stage and then increased back to 1100 ^{o}C. The measured RMS current hysteresis still exists for these cases. For the cases of wet experiments (2-8), the shapes of the measured RMS current for both heating and cooling look similar.

Tables

Nozzle Position (X=190mm, Z=0mm)	Case	Nozzle Operating Conditions		Measured Spray Water Flux Rate (liter/s-m^2)	Time for Each Sample thermocouple Temperature Measurement
		Water Flow Rate, lpm	Air Flow Rate, lpm		
Y=0mm (dry)	1	0	0	0	5min
Y=0mm (wet)	2	2.5	125	11.61	8min
	3	3.5	95	15.20	
	4	4.6	104	20.18	
Y=9mm (wet)	5	2.5	125	2.37	8min
	6	4.6	104	3.32	
Y=18mm (wet)	7	2.5	125	0.03	8min
	8	4.6	104	0.26	

Table 3.1 Experiments Completed with Different Nozzle Operating Conditions

Figures
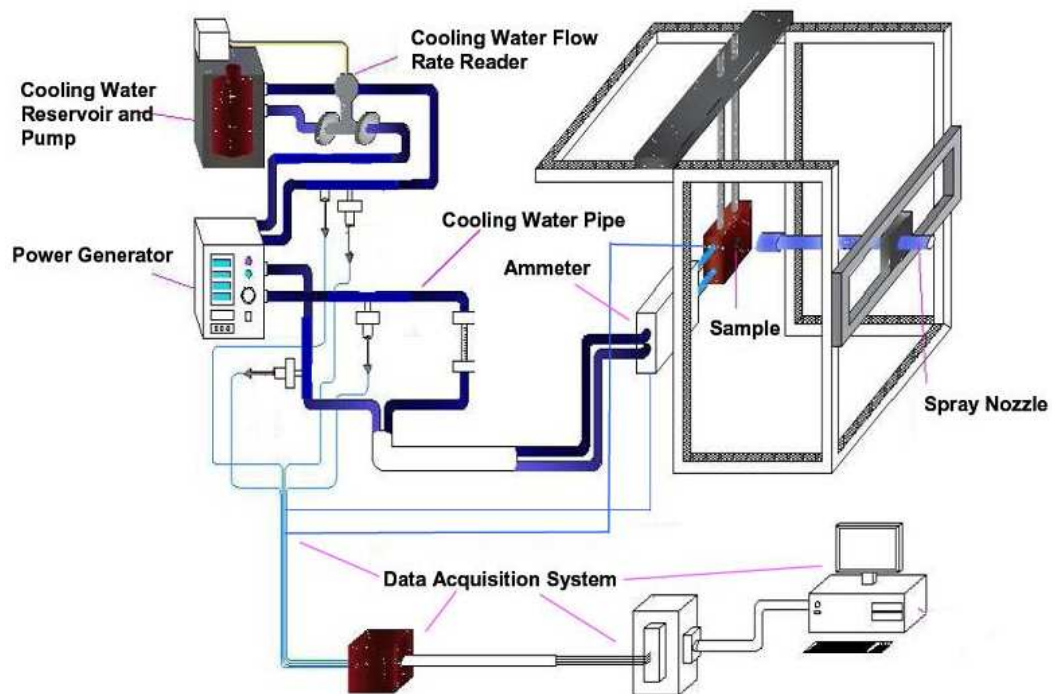
Fig. 3.1 3D Schematic of Experimental Apparatus (Provided by Researchers of the Laboratory of Process Metallurgy at CINVESTAV, Mexico)
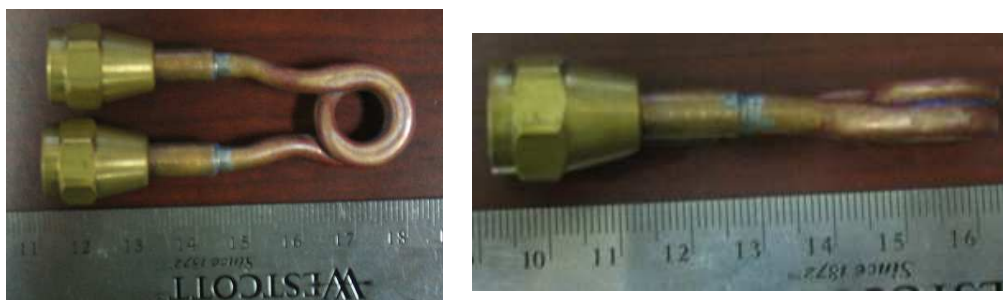
Fig. 3.2 Front View and Top View of Induction Copper Coil
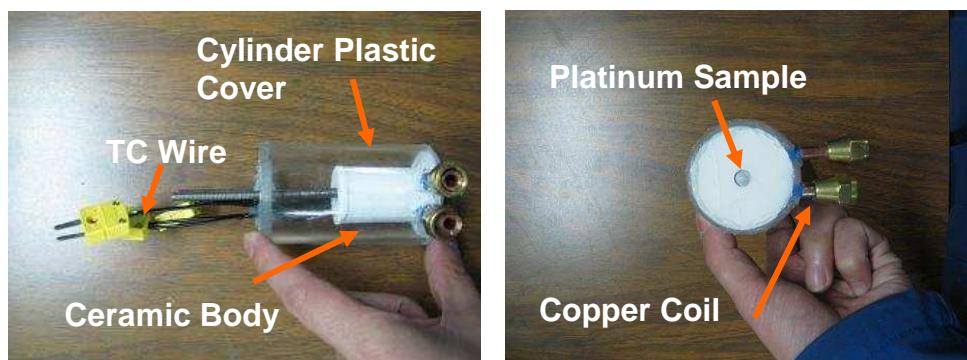
Fig. 3.3 Side View and Front View of the Box

Fig. 3.4 Front View of the Quartz Glass Window
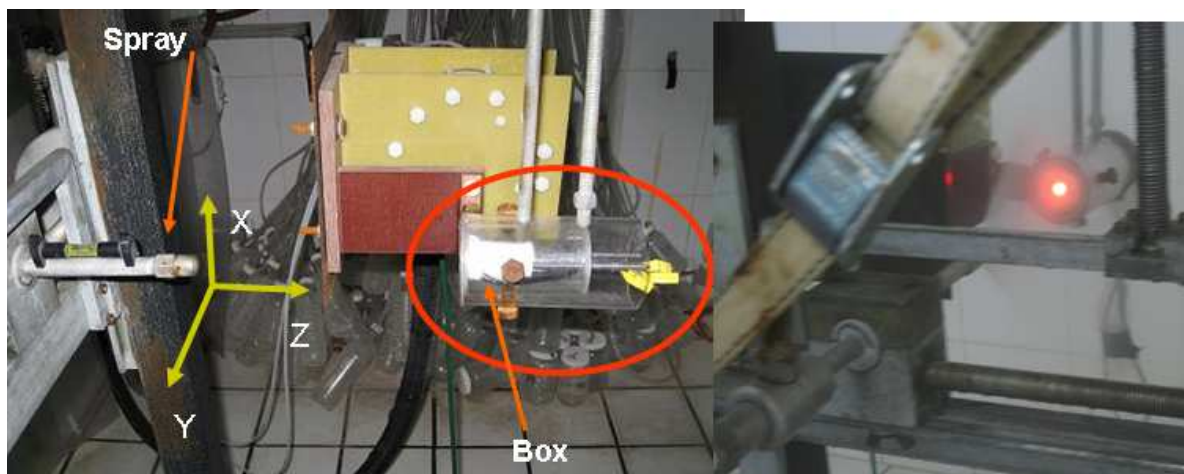
Fig. 3.5 Views of the Disposition of Spray Nozzle and Cylindrical Plastic Box in the Experimental Set-up

Fig. 3.6 Delavan Nozzle W19822 and Three Sample Locations (Y=0, 9, 18mm) Investigated During Experiments
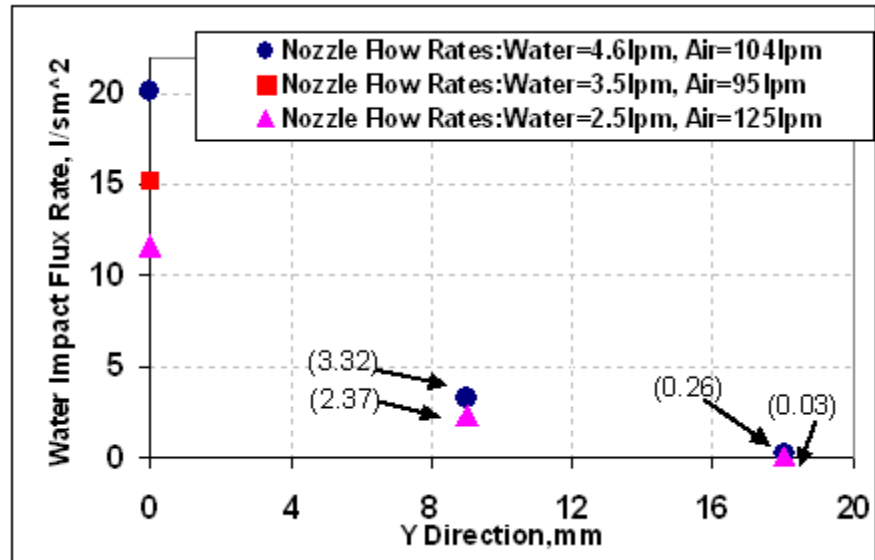
Fig. 3.7 Water Flux Rates for the Three Locations along Y Direction
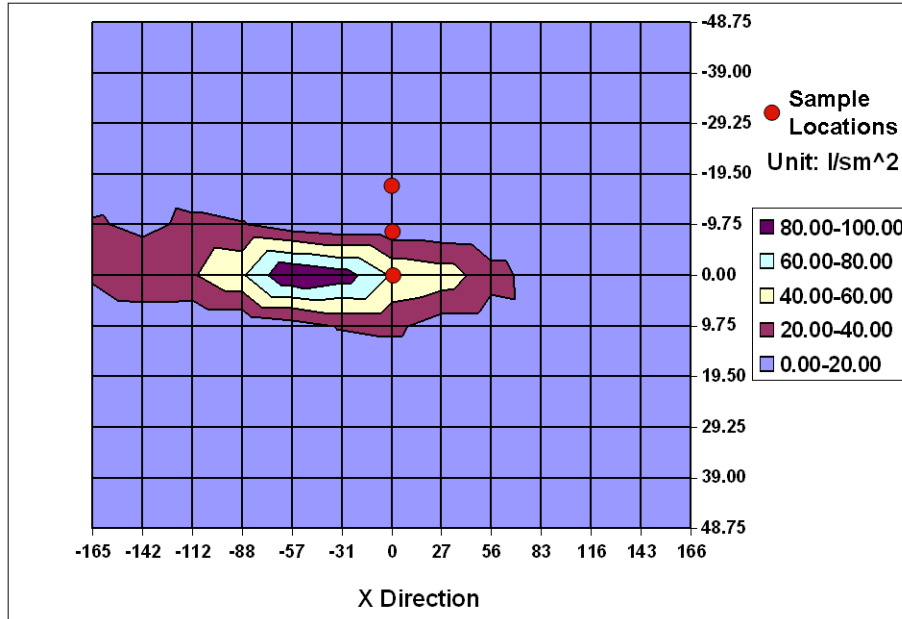
(a) Nozzle Operating Conditions: Water flow rate: 10.72 lpm, Water pressure: 160 PSI, Air flow rate: 53.99 g/min, Air pressure: 126 PSI (X, Y axis are in mm)
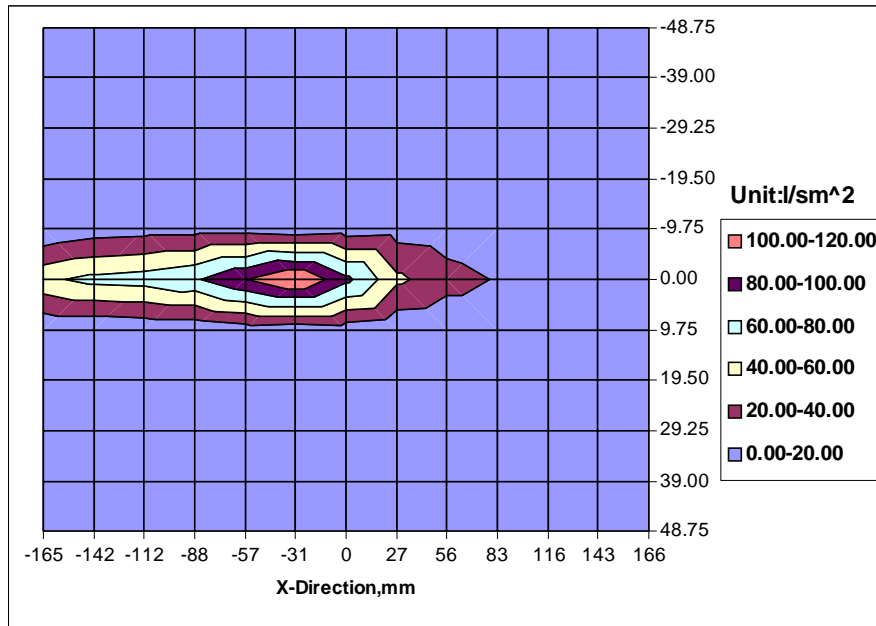
(b) Nozzle Operating Conditions: Water flow rate: 10.84 lpm, Water pressure: 130 PSI, Air flow rate: 51.14 g/min, Air pressure: 105PSI (X, Y axis are in mm)

Fig. 3.8 Water Flux Rate Footprint Measurements of the Nozzle W19822 [50]
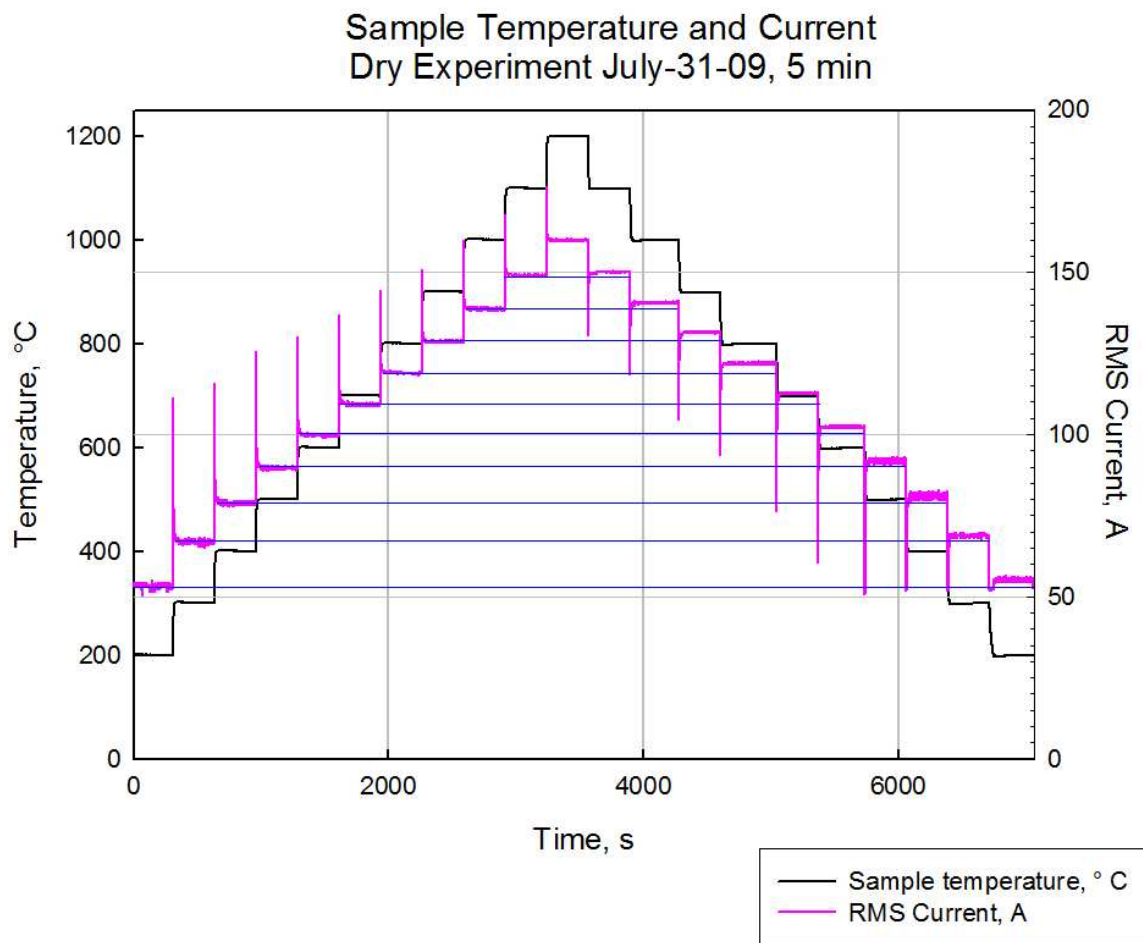
Fig. 3.9 Typical Dry Test Measurements
(Sample Thermocouple Temperature and RMS Current, Case 1)
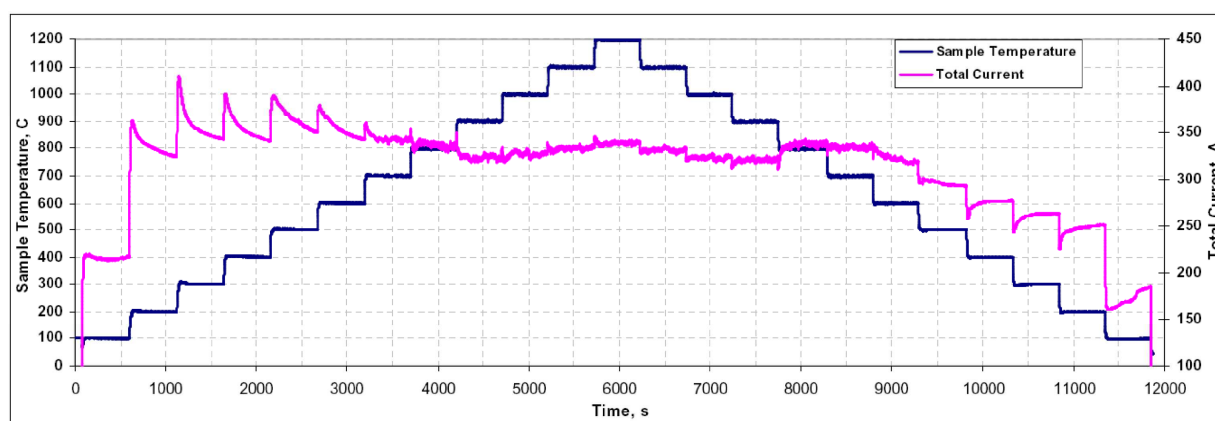
Fig. 3.10 Typical Sample Thermocouple Temperature and Total Current History in a Wet Run
(Case 4, water flow rate: 4.6lpm; air flow rate: 104lpm)
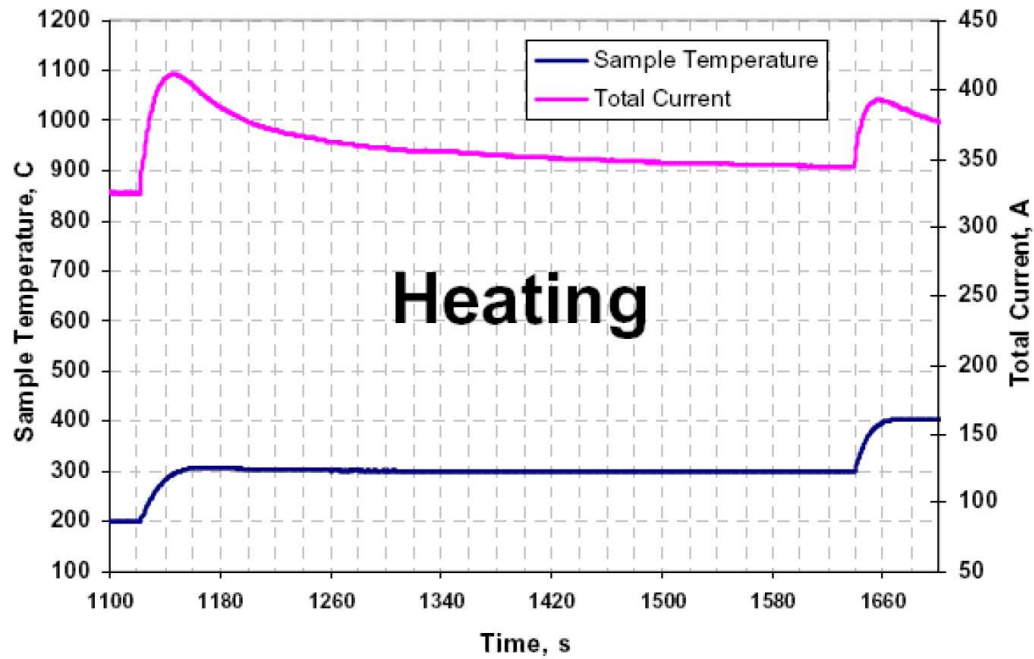
Fig. 3.11 Close-up of Sample Thermocouple Temperature at 300 ^{o}C in Heating
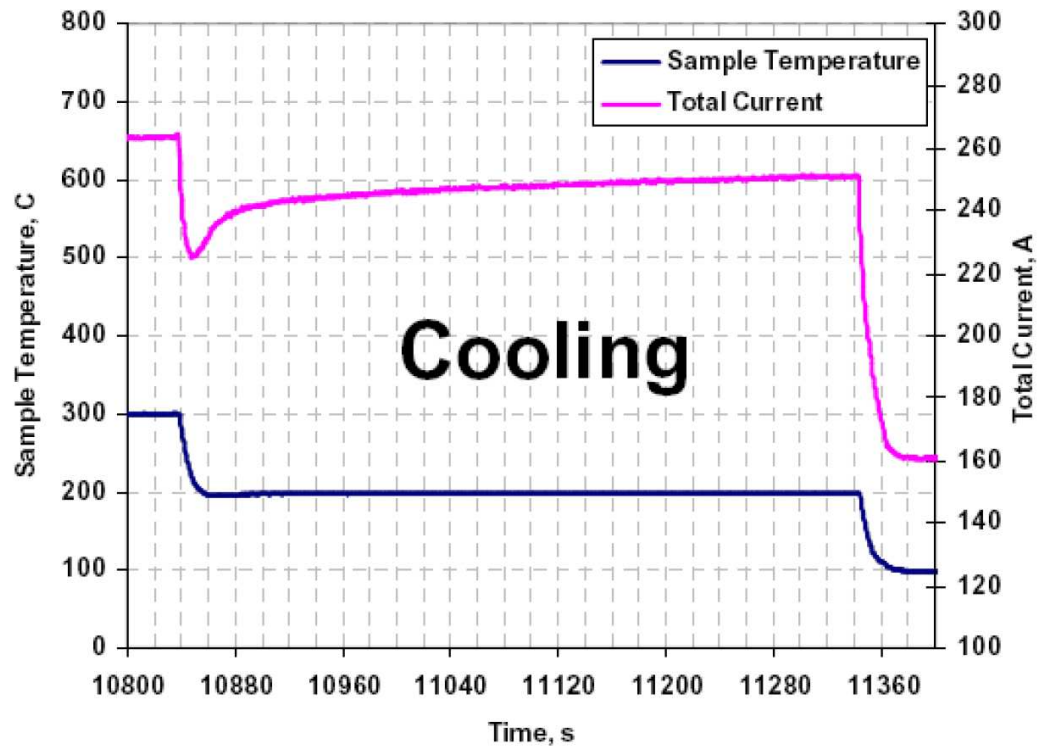
Fig. 3.12 Close-up of Sample Thermocouple Temperature
and RMS Current at 200 ^{o}C in Cooling
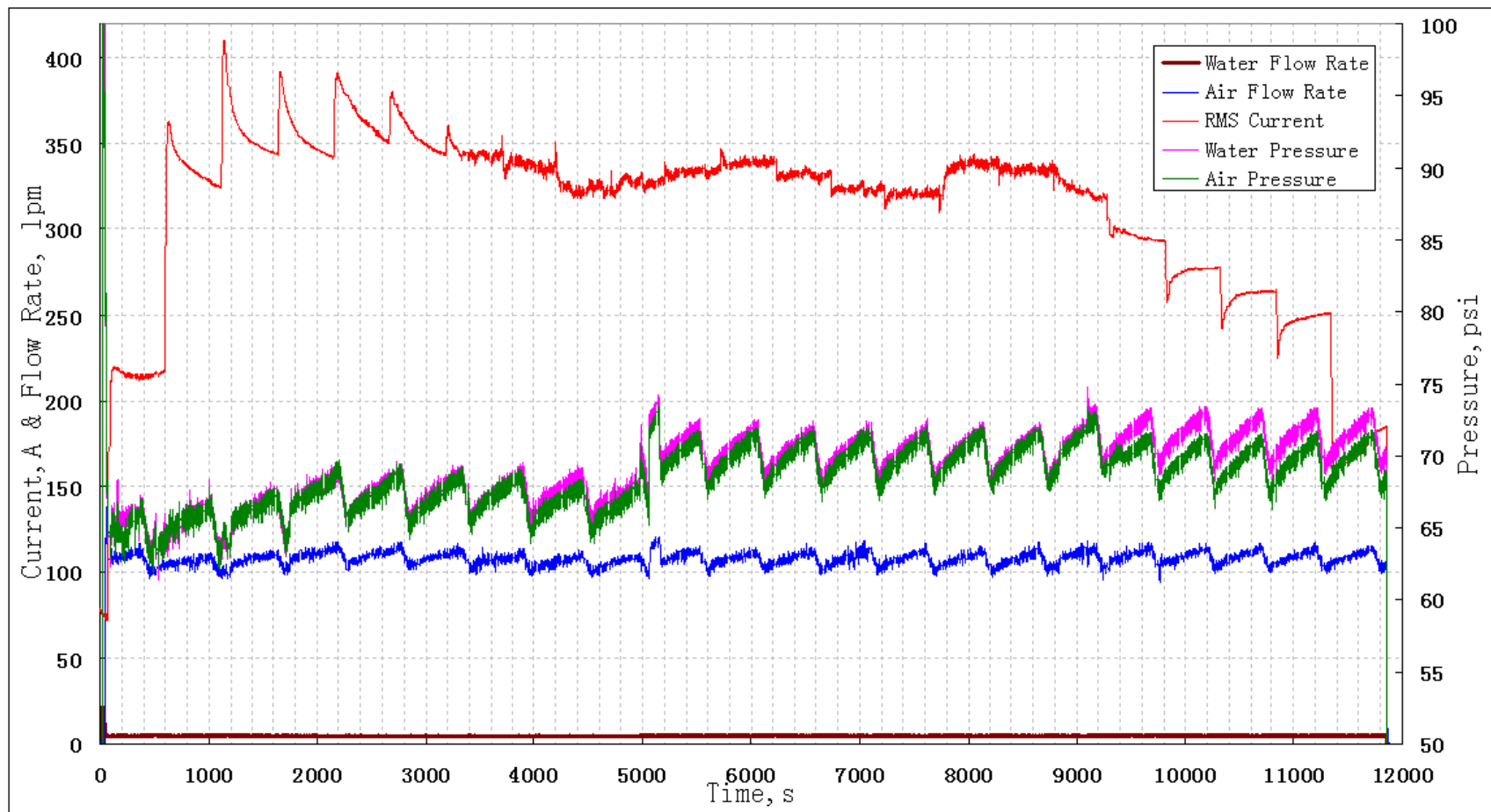
Fig. 3.13 Typical Measurements of Nozzle Water Flow Rate, Air Flow Rate, Water Flow Pressure, Air Flow Pressure and Associated RMS Current (Case 4)

Chapter 4: Computational Modeling of Experimental Apparatus

4.1 Introduction

The experimental measurements, as mentioned above, are mainly temperatures, RMS current and cooling water flow rate. Spray heat transfer rates cannot be measured directly from this steady experimental apparatus, and it is also very difficult to extract spray heat transfer rates just by hand-calculation since the total generated heat distributions inside the sample and the copper coil are unknown. Therefore, a computational model was developed to relate all of the many different measurements together, so that the best possible estimate of the surface heat flux from spray cooling can be determined.

It should be appreciated that the phenomenon associated with the experiments is not merely heat transfer but the coupling between AC power electromagnetics, heat generation, and heat conduction, which is conventionally called induction heating. Induction heating is a multiphysics problem. Varying magnetic flux field is excited by high-frequency alternating current going through the copper coil (which is also called an induction coil). Then an eddy current is induced inside conductive materials through the interaction between the magnetic flux and electrical conductivity. Finally, power is generated by Joule heating. It is necessary to quantify the magnetic flux spatial distribution in order to assess accurately the distribution of heat generation. Then, the heat generation is input to a heat conduction model to predict the temperature distribution, based on the spray cooling heat transfer, which is found by trial and error, as described below.

4.2 Induction Heating Equations

4.2.1 AC Power Electromagnetics Equation Derivation

Maxwell's equations are four partial differential equations that relate the properties of electric and magnetic fields to their sources, charge density and current density [53]. The charge continuity equation and four Maxwell equations are listed below:

- Gauss's law:
$$\nabla \cdot \vec{D} = \rho_f \tag{4.1}$$

- Gauss's law for magnetism:
$$\nabla \cdot \vec{B} = 0 \tag{4.2}$$

- Ampere's law with Maxwell's correction:
$$\nabla \times \vec{H} = \vec{J}_f + \frac{\partial \vec{D}}{\partial t} \tag{4.3}$$

- Faraday's law of induction:
$$\nabla \times \vec{E} = -\frac{\partial \vec{B}}{\partial t} \tag{4.4}$$

- Charge Continuity equation:
$$\nabla \cdot \vec{J}_f + \frac{\partial \rho_f}{\partial t} = 0 \tag{4.5}$$

Only three of these five equations are independent. Equations (4.3) and (4.4) combined with either Gauss's law or the charge continuity equation form such an independent system.

In induction heating, it is assumed that all the materials have linear, isotropic electrical properties, so the following constitutive equations for electromagnetism are used:

$$\vec{D} = \varepsilon_r \varepsilon_0 \vec{E} \tag{4.6}$$

$$\vec{B} = \mu_r \mu_0 \vec{H} \tag{4.7}$$

Ohm's law:
$$\vec{J}_f = \sigma \vec{E} + \vec{J}_{ext} \tag{4.8}$$

The Maxwell equations consist of a set of coupled first-order partial differential equations relating the various components of electric and magnetic fields. In electromagnetism it is convenient to introduce magnetic vector potential and electric scalar, obtaining a smaller number of second-order equations, while satisfying some of the Maxwell equations identically. The definitions of these potentials are shown below.

$$\vec{B} = \nabla \times \vec{A} \tag{4.9}$$

and equation (4.2) is satisfied automatically.

$$\vec{E} = -\nabla \Phi - \frac{\partial \vec{A}}{\partial t} \tag{4.10}$$

and equation (4.4) is satisfied automatically.

Note: the magnetic and electric potentials are not uniquely defined from the two equations above. Introducing two new potentials:

$$\vec{A}_1 = \vec{A} + \nabla f \tag{4.11}$$

$$\Phi_1 = \Phi - \frac{\partial f}{\partial t} \tag{4.12}$$

gives the same magnetic and electric fields:

$$\vec{E} = -\nabla \Phi - \frac{\partial \vec{A}}{\partial t} = -\nabla(\Phi_1 + \frac{\partial f}{\partial t}) - \frac{\partial(\vec{A}_1 - \nabla f)}{\partial t} = -\nabla \Phi_1 - \frac{\partial \vec{A}_1}{\partial t} \tag{4.13}$$

$$\vec{B} = \nabla \times \vec{A} = \nabla \times (\vec{A}_1 - \nabla f) = \nabla \times \vec{A}_1 \tag{4.14}$$

This variable transformation is called a gauge transformation in classical electromagnetics. To obtain a unique solution, it is essential to choose a gauge, which will be discussed later. The physical meaning of each variable is listed here for reference:

- $\vec{A}$: magnetic vector potential,

- $\vec{B}$: magnetic field,

- $\vec{D}$: electric displacement field,

- $\vec{E}$: electric field,

- $\vec{H}$: magnetic flux intensity,

- $\vec{J}_f$: free current density,

- $\vec{J}_{ext}$: external current density,

- Φ : scalar potential,

- ρ_f : free charge density,

- $\varepsilon_0, \varepsilon_r$: free space permittivity and relative permittivity,

- μ_0, μ_r : free space permeability and relative permeability,

Plugging (4.6), (4.7), (4.8), (4.9), (4.10) into (4.3) gives:

$$\nabla \times (\mu_r^{-1}\mu_0^{-1}\nabla \times \vec{A}) = -\sigma\frac{\partial \vec{A}}{\partial t} - \sigma\nabla\Phi + \vec{J}_{ext} - \varepsilon_r\varepsilon_0\nabla\frac{\partial \Phi}{\partial t} - \varepsilon_r\varepsilon_0\frac{\partial^2 \vec{A}}{\partial t^2} \qquad (4.15)$$

The external current density for a sinusoidally driven system may therefore be written:

$$\vec{J}_{ext} = \vec{J}_{ext0}\, e^{j\omega t} \qquad (4.16)$$

where $\vec{J}_{ext0}$ is the magnitude of the external current density and $\omega = 2\pi f$ is angular frequency.

The magnitude of the external current density is in the following form:

$$\vec{J}_{ext0} = -\sigma\nabla V \qquad (4.17)$$

where V is voltage drop across a circuit. (Note V is externally applied voltage drop and is different from scalar potential.)

The other variables in equation (4.15) can be written in the same form as external current density. Therefore, equation (4.15) can be simplified into:

$$\nabla \times (\mu_r^{-1}\mu_0^{-1}\nabla \times \vec{A}_0) - \omega^2 \varepsilon_r \varepsilon_0 \vec{A}_0 = -j\omega\sigma \vec{A}_0 + \vec{J}_{ext0} - (\sigma + j\omega\varepsilon_r\varepsilon_0)\nabla\Phi_0 \quad (4.18)$$

Using the gauge transform $f = -\dfrac{j}{\omega}\Phi$ to simplify this equation gives:

$$\vec{A}_0' = \vec{A}_0 - \frac{j}{\omega}\nabla\Phi \quad (4.19)$$

$$\Phi_0' = 0 \quad (4.20)$$

Then, scalar potential vanishes from equation (4.18) and it becomes:

$$\nabla \times (\mu_r^{-1}\mu_0^{-1}\nabla \times \vec{A}_0') - \omega^2 \varepsilon_r \varepsilon_0 \vec{A}_0' = -j\omega\sigma \vec{A}_0' + \vec{J}_{ext0} \quad (4.21)$$

Apply the following Coulomb gauge to equation (4.21),

$$\nabla \cdot \vec{A}_0' = 0 \quad (4.22)$$

and assuming free space and relative permeability is independent of space, equation (4.21) can be written as:

$$\nabla^2 \vec{A}_0' + \omega^2 \mu_r \mu_0 \varepsilon_r \varepsilon_0 \vec{A}_0' = j\omega\sigma\mu_r\mu_0 \vec{A}_0' - \mu_r\mu_0 \vec{J}_{ext0} \quad (4.23)$$

Compare the second term on the left hand side with the first term on the right hand side, for the AC frequency (2.53e5 Hz) used in experiments, the following equation is true for platinum and cooper:

$$\left| (\omega^2 \varepsilon_r \varepsilon_0)\mu_r\mu_0 \right| << \left| (j\omega\sigma)\mu_r\mu_0 \right| \quad (4.24)$$

Therefore, it is reasonable to neglect the second term on the left hand side. Then equation (4.23) becomes:

$$-\frac{1}{\mu}\nabla^2\vec{A}_0 = -j\omega\sigma\vec{A}_0 + \vec{J}_{ext0} \tag{4.25}$$

Where $\mu = \mu_r\mu_0$ and index denoting gauge transformation is omitted. The equation above is the most compact form for most induction heating problem. The first term on the right hand side is the magnitude of eddy current density which generates heat inside conductive materials. The power density produced by Joule heating is in the form of:

$$Q(W/m^3) = \frac{\left|\vec{J}_{tot0}\right|^2}{2\sigma} \tag{4.26}$$

where

$$\vec{J}_{tot0} = -j\omega\sigma\vec{A}_0 + \vec{J}_{ext0} \tag{4.27}$$

The total heating power is obtained by integrating the local heat generation over the total volume.

4.2.2 Heat Conduction Equation in Induction Heating

Heat conduction is the other phenomenon associated with induction heating problem. Here is the heat conduction equation:

$$\rho C_p \frac{\partial T}{\partial t} = \nabla \cdot (k\nabla T) + Q \tag{4.28}$$

where Q is the heat source for induction heating, which differs for different materials:

- $Q(W/m^3) = \dfrac{\left|-j\omega\sigma(T)\vec{A}_0 + \vec{J}_{ext0}\right|^2}{2\sigma(T)}$, for induction coil

$$\bullet \ Q(W/m^3) = \frac{\left|-j\omega\sigma\vec{A}_0\right|^2}{2\sigma(T)}, \text{ for sample}$$

$\bullet \ Q(W/m^3) = 0$, for free space or nonconductive materials

Note: electrical conductivity is usually dependent on temperature for most materials.

4.3 Model Domains and Geometry Dimensions

The box used in the experiments consists of the ceramic body, induction coil, sample, air and quartz glass. The ceramic body is axisymmetric in shape. To simplify the problem, it is convenient to assume the induction coil to be axisymmetric too. Therefore, a 2-D axisymmetric domain including the ceramic body, induction coil, sample, air and quartz glass was developed using COMSOL, as shown in Figure 4.1. The platinum sample and the two induction coils are accommodated inside the ceramic body which is surrounded by air. The geometry dimensions are clearly labeled in this figure. The thickness and the radius of the platinum sample are 2.5mm, 4mm, respectively. The height and the radius of the ceramic body are 40mm, 13.5mm, respectively. The induction copper coil is a hollow coil with a thickness of 0.5mm. The inner loop radius of the induction coil is 5.00mm. The thickness of the quartz glass is 0.5 mm. The radius of the whole domain is 60mm and the height of the whole domain is 120mm. Both dimensions are set to be large enough to assure the magnetic potential could be approximated to be 0 at the far-away boundaries.

Since induction heating is a coupled problem involving two separate phenomena, it is necessary to identify the modeling domains for the equations for both types of physics. As shown in Figure 4.1, the AC power electromagnetics is active in the whole domain while the heat

conduction is active in parts of the red region which consists of ceramic, induction coil, sample and quartz glass.

4.4 Induction Heating Boundary Conditions

Boundary conditions for both AC power electromagnetics and heat conduction are shown in Figure 4.2. Axisymmetry is assigned to both equation systems at the axisymmetric line.

For the AC power electromagnetics, the remaining three boundaries are set to be magnetic potential insulation. Actually, it is also reasonable to assign electric insulation to these boundaries, since the magnetic potential distribution is almost the same for both kinds of boundary conditions.

For the heat conduction problem, the top and right boundaries contact air, and there is no fan blowing the ceramic body. Thus, natural convective heat transfer coefficient is employed at these boundaries. This coefficient is estimated to be 10 W/m^{2}K. Actually, the convective heat transfer at these boundaries does not influence temperature distribution very much in the wet experiments modeling, since the heat taken away by the air is relatively very small compared to that taken away by the spray cooling.

The front surface of the platinum sample is exposed to spray cooling and heat flux through it may be not be uniformly distributed. It is necessary and more accurate to use a convection heat transfer coefficient to account for spray cooling behavior. This coefficient is the quantity that should be extracted from this computational model. Since the spray can impact onto quartz glass, a heat transfer coefficient should be assigned to the quartz glass surface. During wet tests modeling, this heat transfer coefficient is estimated by using the following Nozaki empirical correlation [29].

$$h(W/m^2K) = A*1570*Q_w^{0.55}(l/m^2s)(1-0.0075T_{spray}(^oC)) \qquad (4.29)$$

The water flux rates for different locations along the spray width are measured and shown in Figure 3.7 for different spray water flow rates. The heat transfer coefficients are estimated, by the Nozaki correlation with A=1, for the locations at the center point and the point 9mm away from spray centerline for two different spray water flow rates of 4.6 lpm and 2.5 lpm. For each the water flow rate, the front window heat transfer coefficient (h_front) is estimated by averaging two heat transfer coefficients at these two points. 5500 W/m^{2}K is for the spray water flow rate of 4.6 lpm and 4000 W/m^{2}K is for 2.5 lpm. For the spray water flow rate of 3.5 lpm, 5000 W/m^{2}K is roughly estimated and used. In Section 5.3.2, this heat transfer coefficient will be investigated in terms of parametric study.

The heat transfer coefficient for the cooling water circulating through the copper coils is estimated by the Sleicher & Rouse empirical relationship [54] which relates coil surface temperature, cooling water temperature and cooling water velocity, as shown below.

$$h = (5+0.015\,\mathrm{Re}_{film}^{(0.88-\frac{0.24}{4+\mathrm{Pr}_{surf}})}\,\mathrm{Pr}_{surf}^{\frac{1}{3}+0.5\exp(-0.6\mathrm{Pr}\_surf)})*k_{water}/D \qquad (4.29)$$

where $\mathrm{Re}_{film} = \dfrac{\rho VD}{\mu}$ and $\mathrm{Pr}_{surf} = \dfrac{Cp\mu}{k}$, for $0.1 < \mathrm{Pr} < 10^5$ and $10^4 < \mathrm{Re} < 10^6$. The water properties used to calculate Reynolds number are evaluated at the temperature from averaging the coil surface temperature and the cooling water temperature. The water properties used to calculate Prandtl number are evaluated at the wall temperature. The cooling water temperature is estimated by averaging two thermocouple measurements. These thermocouples were installed inside the pipe before the cooling water entering the induction coil and also after the cooling water leaving the coil, respectively. In the dry tests modeling all the heat transfer coefficients except that

cooling water are calibrated to be 10 W/m^{2}K. In addition, thermal radiation is taken into account for the platinum front surface.

4.5 Solution Methodology

COMSOL Multiphysics (version 3.5) [48] is well known for its strong ability in multiphysics modeling. Its AC/DC module provides the user with the access to solve induction heating problem in both 2-D and 3-D geometries.

For calibration of dry experiments: start with a steady-state simulation at a given sample thermocouple temperature. Then perform a transient induction heating simulation to reach the next sample thermocouple temperature with measured total current history used in the model. Then compare the modeling result of sample thermocouple temperature history with measured sample thermocouple temperature history to calibrate the model. The details of the calibration procedure will be discussed in section 5.1.

For wet experiments, the most important parameter is the spray heat transfer coefficient. For each sample thermocouple temperature with a certain total current, an estimated value of spray heat transfer coefficient is input into COMSOL to calculate the temperature prediction at the location where the sample thermocouple is located. This temperature prediction is improved by adjusting the spray heat transfer coefficient until the prediction matches the measurement. Then, local heat flux is integrated over platinum surface to obtain the total heat flux extracted by the spray cooling.

4.6 Materials Properties

Some non-temperature-dependent material properties used in this experiment are listed in Table 4.1. There are several temperature-dependent material properties: platinum thermal conductivity, platinum emissivity, platinum and copper electrical conductivities, which directly affect the temperature distribution. Figures 4.3, 4.4, 4.5 and 4.6 show their dependence on temperature. Platinum emissivity is taken from the Platinum Metals Review website [55] and is less than 0.2 for surface temperatures below 1400 ^{o}C. Some literature [56~62] presents platinum emissivity graphs obtained by experimental measurements, which are very close to those shown in Figure 4.4 for the same platinum surface temperature. The data in Figure 4.4 is input to COMSOL as a look-up table with temperature.

Platinum electrical conductivity can be modeled as a function of temperature [55]:

$$\sigma_{Pt}(ohm^{-1}m^{-1}) = \frac{1}{1.04 \times 10^{-7}(1+0.0038(T(^{o}C)-20))} \qquad (4.29)$$

and this relation is input into global equation option of COMSOL to account for temperature dependence of platinum electrical conductivity. For the copper electrical conductivity [63] and platinum thermal conductivity [55], it is handled in another way. Preliminary results show that temperature differs by less than 5 ^{o}C for all sample thermocouple temperatures in the copper coils and this causes only a very small variation in copper electrical conductivity, as indicated in Figure 4.6. Temperature differs by less than 100 ^{o}C in the platinum sample and this causes a very small variation in platinum thermal conductivity, as indicated in Figure 4.3. Therefore, to speed up computation, it is reasonable to assume a constant copper electrical conductivity and a constant platinum thermal conductivity at each sample thermocouple temperature.

The ceramic manufacturer reports ceramic thermal conductivity to be 0.58 W/m without the level of porosity and the specified temperature at which it was measured. These two

parameters are very important in determining ceramic thermal conductivity. It will be obtained by dry experiments calibration. And it should be further validated with the ceramic thermal conductivity experiments done in CINVESTAV. These will be discussed in some sections later.

4.7 Induction Heating Model Validation with Previous Model

It is necessary to validate any sophisticated computational model with a test case with a known solution in order to examine its features, flexibility and functionality, and to prove it has been formulated correctly. Most induction heating examples presented in previous work have a complicated geometry or do not mention essential materials properties, so are not good test cases. A good test case should have a simple geometry and complete information to allow re-modeling. A simple example [64] of a 1-D axisymmetric transient induction heating problem presented by ANSYS meets these requirements. The simplified geometry of this problem considers only a finite length strip of the long round billet, essentially reducing the problem to a one-dimensional study shown in Figure 4.7. Boundary conditions are given in Figure 4.8. The current was applied as a current density source term in the rectangular (annular) region representing the cylindrical coil with zero applied current density elsewhere. Figure 4.9 shows the overlapping results of ANSYS and the current model in COMSOL for the outer surface and center billet temperature histories. The two models match very well.

Tables

	Cp (J/kgK)	Density (kg/m3)	Electrical conductivity (1/m*ohm)	Thermal Conductivity (W/m·K)
Copper Coil	385	8960	Temp dependent	400
Platinum	133	21450	Temp dependent	Temp dependent
Cooling Water	4187	988	1	--
Ceramic	740	1762	1	Refer to section 5.1

Table 4.1 Material Properties for Modeling

Figures
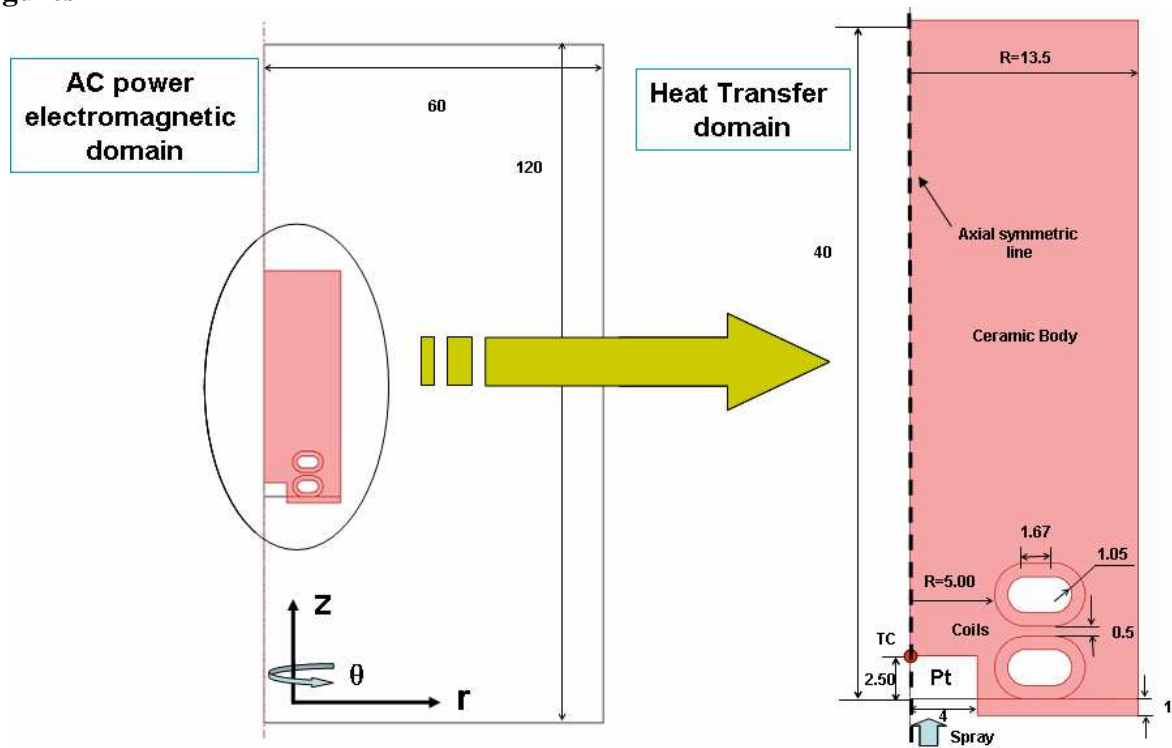
Fig. 4.1 AC Power Electromagnetic and Heat Transfer Modeling Domains and Geometry Dimensions in COMSOL
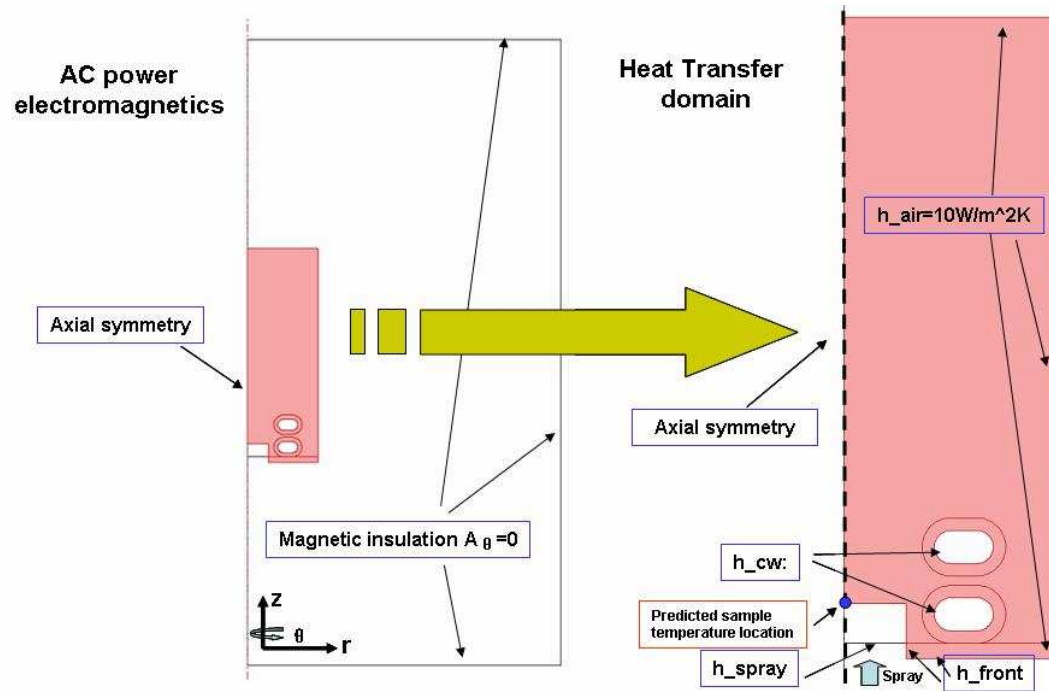
Fig. 4.2 AC Power Electromagnetic and Heat Transfer Boundary Conditions in COMSOL
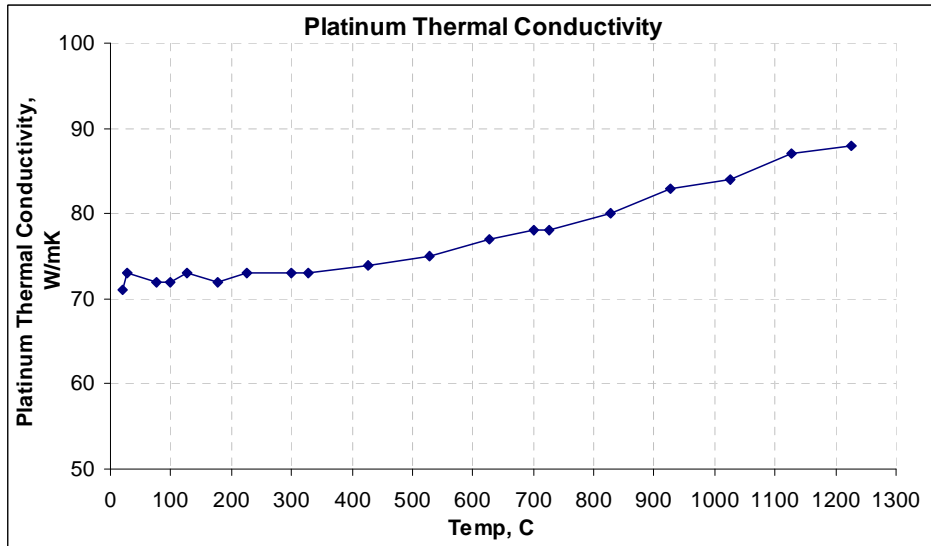
Fig. 4.3 Temperature Dependent Thermal Conductivity of Platinum [55]
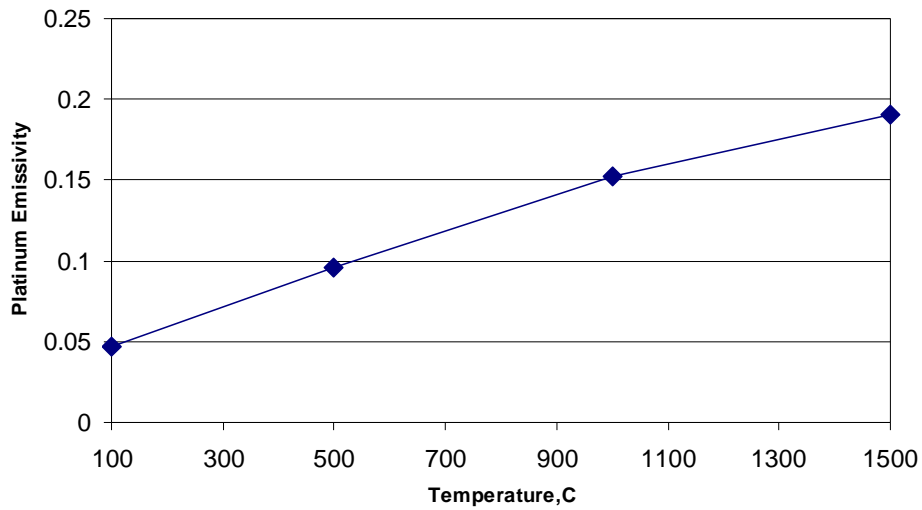
Fig 4.4 Temperature Dependent Platinum Emissivity [56~62]
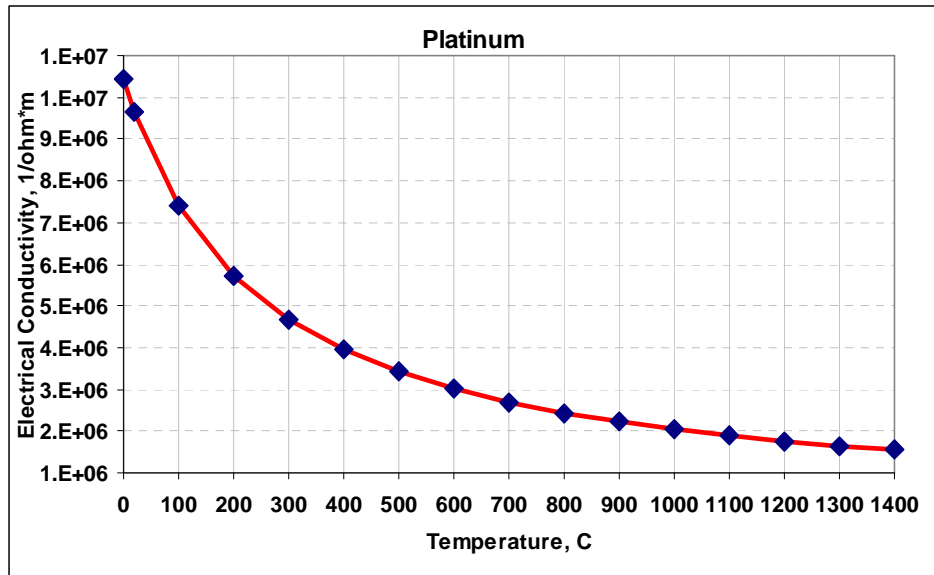
Fig. 4.5 Temperature Dependent Electric Conductivity of Platinum [55]
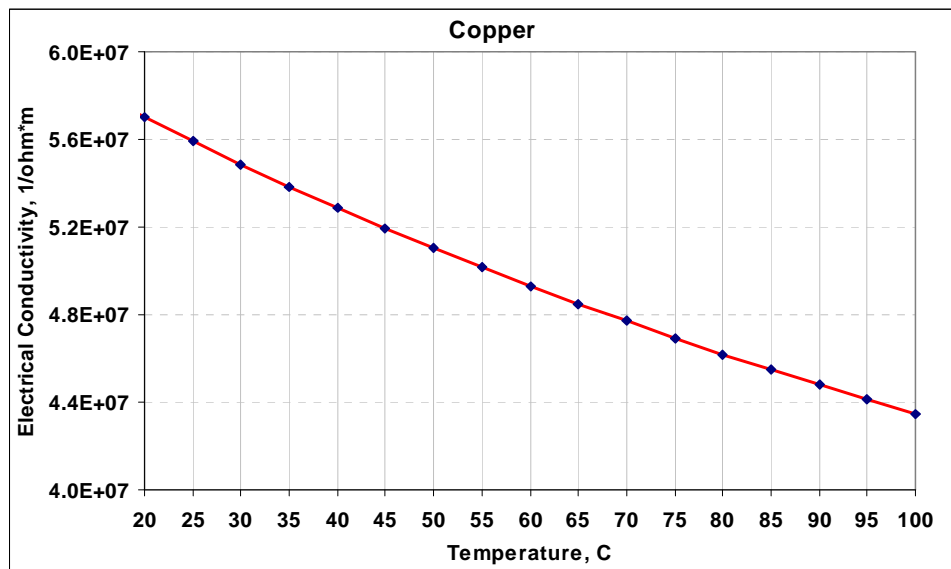
Fig. 4.6 Temperature Dependent Electrical Conductivity of Copper [63]
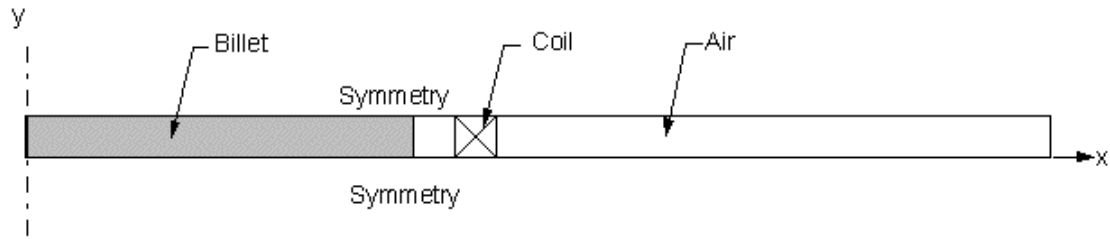
Fig. 4.7 Schematic of Problem Domain [64]

• Boundary conditions for heat transfer
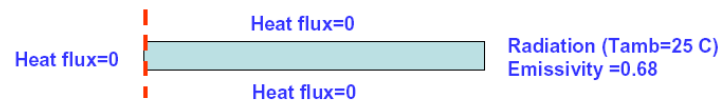
• Boundary conditions for electromagnetics
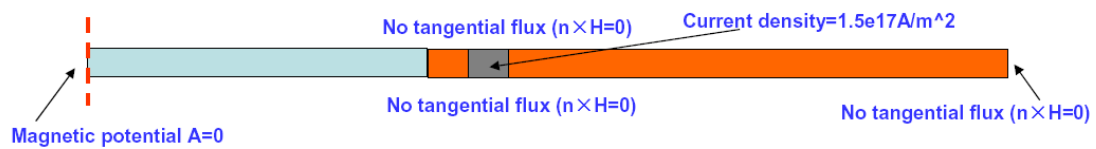
Fig. 4.8 Heat Transfer and Electromagnetic Boundary Conditions
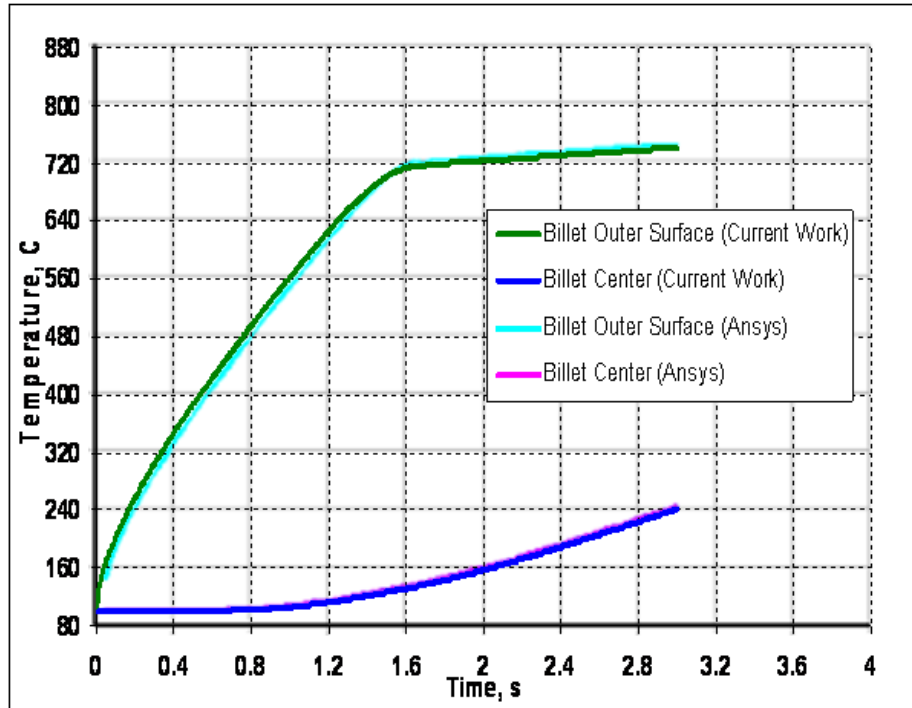
Fig.4.9 Test Problem Temperature Histories (Comparing Current Work with COMSOL model

and previous ANSYS Model [64] for both Billet Outer Surface and Center)

Chapter 5: Interpretation of Experiments with Model

5.1 Model Calibration

5.1.1 Model Calibration by Matching Dry Experiments Measurements

Owing to uncertainties in the materials properties and inaccuracies in representation of the 3-D geometry with a 2-D model, calibration was performed to enable the model to accurately predict the experiment behavior as closely as possible. As shown in Fig. 3.2, the induction coil, actually, has a very complicated 3D shape. It consists of several parts, with roughly 70% two-loop and 30% one-loop which are connected with a helix shaped part. The current 2-D axisymmetric modeling geometry assumes two 100% circular loops. Using the actual measured loop inner radius, this domain intuitively creates larger heat generation in the sample than that of the real coil. Preliminary study shows that increasing the loop inner radius decreases the total heat generated in the sample. Therefore, the model was calibrated by increasing the loop inner radius appropriately to generate the same heat in the sample as that of the real coil.

In addition to the loop inner radius, the ceramic thermal conductivity is also very important. For a given inner radius, heat generated inside the sample is determined by the measured induction current. In contrast with the high and uncertain spray heat extraction rates of the "wet" experiments, the dry experiments involve small, well-characterized natural convection and radiation boundary conditions. Thus, the sample thermocouple temperature prediction is controlled by the ceramic thermal conductivity. The larger the conductivity, the more heat is taken away through the ceramic and the smaller the sample thermocouple temperature is. Therefore, the ceramic thermal conductivity also needs calibration to make temperature prediction match the sample thermocouple measurement. Calibrating the transient model predictions to match all of the dry experimental measurements of thermocouple temperature

histories at different currents provides a good opportunity to determine both the best larger inner loop radius and the best temperature-dependent ceramic thermal conductivity function to use in all simulations.

The first step for calibration is to investigate the effect of the loop inner radius on a typical predicted transient sample thermocouple temperature history, chosen to be the 800$^{\text{o}}$C step. A different coil loop inner radius (5.0mm, 5.5mm, 5.8mm, and 6.0mm) is used to create each modeling domain. For simplification, a different constant ceramic thermal conductivity is used for each loop radius which is chosen by adjusting to match the steady temperature measurements by the sample thermocouple. Firstly, a steady state simulation is done to match the sample thermocouple temperature measurement at 700 $^{\text{o}}$C to obtain a reasonable initial temperature distribution. With the material properties in Table 4.1 and measured total current history, (in Figure 5.1), a transient simulation of 100s is then performed for each inner radius.

The transient sample thermocouple temperature results for this calibration step are shown in Figure 5.1 and the calibrated ceramic thermal conductivities are included in the legend. The loop inner radius controls the heat generation which in turn controls the predicted transient temperature evolution shape. For the inner radius of 5.0mm (which is also the actual inner radius), the sample thermocouple temperature jumps from 700 $^{\text{o}}$C to 815 $^{\text{o}}$C in 15s, overshooting the measured temperature before dropping gradually to the steady temperature of 800 $^{\text{o}}$C. As the coil inner radius increases, this unrealistic peak weakens. Smaller radius gives larger overshoot while larger radius gives longer transient time. As shown in Figure 5.1, the 5.8mm inner radius gives the best match of transient temperature shape.

The next step for calibration is to find a temperature dependent ceramic thermal conductivity, with the inner radius of 5.8mm. The following calibration methodology is taken.

(1) Calibrate step by step from the sample thermocouple temperature of 100 to 1200 ^{o}C; 12 steps in total (j=1, 2, …, 12). (2) Before calibration for the step j+1, ceramic conductivity should have been calibrated for temperature less than Ts(j)+30 ^{o}C. When calibrating for the step j+1, find a conductivity at the temp of Ts(j+1)+30 ^{o}C by matching the prediction with the steady thermocouple measurement of Ts(j+1). Then the conductivity is calibrated for the temp range of 20 ^{o}C ~ Ts(j+1)+30 ^{o}C. Temperature predictions for steps before j+1 are not affected by step j+1 calibration. (3) Move calibration on until j=12. The calibrated ceramic thermal conductivity is shown in Figure 5.2.

Then, with the calibrated temperature dependent ceramic thermal conductivity, the measured current (as shown in Figure 5.3), cooling water heat transfer coefficient of 2.96 W/m^{2}K inside the coil, and the natural convection heat transfer coefficient of 10W/m^{2}K, the model is run to predict transient temperature histories. The model predictions and the measurements of the sample thermocouple temperature are shown in Figure 5.4. The differences between predicted steady temperature and measured steady sample thermocouple temperature are shown in Table 5.1. Both transient and steady predictions match measurements very well.

The calibrated inner radius and temperature dependent ceramic thermal conductivity will be used in model simulations of the wet experiments.

5.1.2 Ceramic Thermal Conductivity Validation with Experiments

The ceramic manufacturer reports ceramic thermal conductivity to be 0.58 W/m. The calibrated ceramic thermal conductivity is distributed around this value. It is necessary to check the validity of the calibrated curve. An experiment regarding ceramic thermal conductivity measurement was done in CINVESTAV.

Figure 5.5 and 5.6 show a photo and a schematic of the apparatus to measure ceramic thermal conductivity. A cylinder ceramic body, which was made using the same ratio of ceramic powder to water as that in spray cooling experiments, rests on a thin metallic sheet. The sheet was heated up by a Bunsen burner. A thermocouple was welded into the sheet to measure and monitor sheet temperature. The other eight thermocouples were installed along the axial axis of cylinder ceramic body and used to measure temperature inside ceramic. The positions of thermocouples are listed in Table 5.2. The top surface of the cylinder ceramic body was exposed to natural convection in the laboratory environment. The lateral surface was insulated by a ceramic fiber. For each experiment the apparatus was run for around three hours to ensure steady state heat transfer was reached inside ceramic. Typical temperature measurements are shown in Figure 5.7.

A 2-D axisymmetric heat conduction model was created using COMSOL. Figure 5.8 shows the modeling geometry, dimensions and boundary conditions. The model consists of a ceramic body and an insulator. The radius of the ceramic body is 13.1mm and the height is 40mm. The thickness of the insulator is roughly estimated to be 25mm. The bottom surface of the ceramic body was heated by a thin metallic sheet which was heated up by a Bunsen burner. Since the metallic sheet is thin and has much larger thermal conductivity than ceramic, it is reasonable to assume its temperature is uniform across the interface between the sheet and the ceramic body. And, it is good to assume the contact between the sheet and the ceramic body was intimate so that the ceramic body bottom surface has the same uniform temperature as that of the sheet. The geometry is 2-D axisymmetric, so axisymmetry boundary condition is assigned to the left boundary. The remaining boundaries were exposed to natural convection in the laboratory

and used appropriate convective heat transfer coefficient to make best match between the temperature measurement and prediction.

The convective heat transfer coefficient is estimated by empirical correlations [65] ranging from 4 to 20W/m^{2}K. And 17W/m^{2}K is chosen by calibration requirement. Due to lack of the insulator thermal conductivity and non-perfect contact between the insulator and the ceramic cylinder, it is tricky to deal with the insulator thermal conductivity. During the tests, it was found that the insulator surface was not hot ($< 40^o$C). This can be a criterion needed to be satisfied in modeling. The value of the insulator effective thermal conductivity is estimated to be 0.02W/mK. The temperature predictions with using the calibrated ceramic thermal conductivity for five experimental tests with different metallic sheet temperature are compared with measured temperatures and shown in Figure 5.9 (a), (b) and (c). All modeling results give insulator surface temperature less than 40 ^{o}C, which is reasonable. The temperature prediction curves match the measurements very well.

5.2 Example Modeling of Wet Experiments

As already discussed in Section 3.2.1, the sample thermocouple temperature and RMS current during each wet experiment is much closer to steady state near the end of each sample thermocouple temperature stage. Thus, it is convenient and reasonable to do steady state induction heating analysis for each sample thermocouple temperature.

An example analysis for the sample thermocouple temperature equal to 700 ^{o}C is given here. The nozzle operating conditions for this sample thermocouple temperature are for case 4: water flow rate equals to 4.6lpm; air flow rate equals to 104lpm; nozzle is centered towards the sample. The total current is 484.6 A, which is the average value of last 30 seconds at the sample

thermocouple temperature 700 ^{o}C. Material properties discussed in the Section of 4.5 are used. Calibrated ceramic thermal conductivity is used. Spray heat transfer coefficient is 7100 W/m^{2}K.

Modeling results of this steady state induction heating analysis are shown below.

(a) Magnetic Potential Distribution

Figure 5.10 shows the magnetic potential distribution calculated in the entire modeling domain. Magnetic potential is mainly confined around the conductive materials region and goes to zero as the boundaries are approached.

(b) Magnetic Flux Density Distribution

Figure 5.11 shows the magnetic flux density distribution in the entire model domain. The skin effect is clearly shown in both induction coils and the sample. The magnetic field is strongest in the ceramic between the sample and lower loop of coil, but is more important in the edge of sample and copper. As induced currents flowing in conductors generate magnetic field which opposes the primary field, the net magnetic flux is reduced as the depth increases, causing a decrease in current flow.

(c) Induced Current Distribution

Figure 5.12 shows the induced current density distribution inside conductors (sample and induction coils).

(d) Heat Source Distribution

Figure 5.13 shows the heat generation by induction heating inside conductors. Heat is mainly generated in the surface layers (skins) of the induction coils and the sample, which are closest to each other. Even though magnetic flux is highest in the ceramic layer between these two skins, the low electrical conductivity prevents heat generation there.

(e) Temperature Distribution

Figure 5.14 shows the temperature distribution for the entire heat transfer domain. Temperature in the ceramic region far from the sample is relatively smaller than that at the sample. Large temperature gradients are observed at the ceramic region close to the sample. The temperature inside the copper coil does not vary very much (~5 $^{\circ}$C), which means it is reasonable to use constant material properties for each sample thermocouple temperature.

(f) Sample Frontal Surface Temperature Distribution

Figure 5.15 shows the temperature distribution along the sample front surface where spray impinges. The temperature is not uniform, as it increases towards the heated edges of the sample. The difference between the maximum and minimum temperatures is around 55 $^{\circ}$C. This temperature difference should be taken into account when quantifying the relation between spray heat transfer rates and sample surface temperatures.

5.3 Further Study of the Model

5.3.1 Mesh Investigation

Computational modeling accuracy depends on mesh quality. The mesh size should be sufficiently fine to capture significant variations of physical quantities of interest everywhere the computational domain, including regions with sharp changes in gradient. A mesh refinement study was conducted for the steady-state example case (case 4) discussed in Section 5.2 by simulating again with a finer mesh. The previous coarse mesh (11,968 elements) and new fine mesh (39,701 elements) are shown in Figure 5.16, which also shows that the element size in the critical high-gradient region near the sample edge decreases from 0.1 mm to 0.06 mm width. All other conditions stay the same. Some heat transfer results are shown in Table 5.3. Spray heat transfer coefficient, generated heat in the sample and the coils, heat going into the spray and the

heat going to the cooling water almost do not change. The fine-mesh sample thermocouple temperature prediction increases by 4 ^{o}C. The sample front surface temperature distributions for these two meshes are shown in Figure 5.17 and also differ by around 4 ^{o}C. These results obviously show that the previous coarse mesh quality is good enough. The coarse mesh requires only 4% computation time of the fine mesh, so was used in all subsequent simulations.

5.3.2 Parametric Study of the Model

Simulations were performed to investigate the accuracy of the methodology developed in this work to extract heat transfer coefficients from the experimental measurements. Specifically, the important parameters in the model were varied in three separate studies to determine the importance of uncertainty in the coil geometry, the window heat transfer coefficients, and the ceramic thermal conductivity function. The cooling water heat transfer coefficient inside the coils and the copper electrical conductivity had almost no effect on the steady state heat transfer results, so were not investigated further.

(a) Geometry Parametric Study

As discussed in section 3.1, the 3-D geometry of the induction coil is very complicated. But this special shape provides an access to modeling in 2-D. Preliminary modeling suggests heat transfer results are sensitive to the distance between the sample and the coil. Therefore, it is necessary to do parametric study to investigate the effect of geometry variation on the heat transfer results of modeling wet experiments.

The gap size between the two copper coil loops is measured to be around 0.5mm, as shown in Fig. 4.1. Actual measurements of the gap ranged from 0.4 to 0.6mm, so domains were created using all three of these gap sizes. An example case with a sample thermocouple

temperature of 900 ^{o}C is selected from case 4 during heating to illustrate the effect of variation of the gap size on the heat transfer results. Steady state simulation is run with a total current of 456A, a ceramic thermal conductivity of 0.35W/mK, and adjusting spray heat transfer coefficient to match the sample thermocouple temperature measurement The heat transfer results for all three different gaps are shown in Table 5.4. Compare these results, spray heat transfer coefficient varies by less than 3%; the heat generated inside the sample varies by 3%; the heat generated inside the copper coils almost does not change, the heat taken away by the spray cooling varies by less than 4%; and the heat going into cooling water almost does not change. All results suggest the variation of gap size between the copper coil loops does not change heat transfer results significantly, so long as the predictions match the measured sample temperature. Thus, a constant gap size of 0.5mm was used in all subsequent simulations.

(b) Front window heat transfer coefficient study

As discussed in Section 4.4, the spray heat transfer coefficients at the front quartz glass window are estimated using the Nozaki empirical correlation (given in Equation 4.29) for each flow rate with the empirical adjustment coefficient A=1. Heat transfer coefficients are estimated using the measured spray water flow rates at two points (0 and 9mm in Fig. 3.6). Uncertainty in this estimate arises from interpolating between these points for different nozzle orientations, in addition to the Nozaki correlation itself. Therefore, a parametric study was done to find how much the variation of this coefficient will affect the final heat transfer results.

The same example case as that in Section 5.2 is taken here. Three different front window heat transfer coefficients of 7000 W/m^{2}K, 5500 W/m^{2}K and 3000 W/m^{2}K are investigated. The spray heat transfer coefficient is adjusted to match the prediction of the sample thermocouple

temperature measurement, keeping other parameters the same. Some heat transfer results are shown in Table 5.5. Even though the front window heat transfer coefficient changed by 27%, the spray heat transfer coefficient changes by less than 0.6% Heat removed by the cooling water and front window remain almost constant. Thus, the significant variations of the front window heat transfer coefficient have negligible effect on the heat transfer results.

(c) Ceramic Thermal Conductivity Parametric Study

Another set of temperature dependent ceramic thermal conductivities were obtained by performing the dry experiment (case 1) calibration with increase in sample surface radiation using a platinum emissivity of 1, which triples the surface heat transfer removal rate by for the surface temperatures above 800 ^{o}C. The re-calibrated conductivity curve (curve 2) is shown in Figure 5.18 together with the ceramic thermal conductivity curve (curve 1) calibrated with radiation taken into account properly. The effect of changing to curve 2 on the spray heat transfer coefficient results obtained from the wet experiments was then investigated.

Three sample thermocouple temperatures of 400 ^{o}C, 800 ^{o}C and 1200 ^{o}C during heating from the wet experiment with the water flow rate of 4.6 lpm and the sample located in the spray centerline are taken as examples to find the effect of different ceramic thermal conductivity on the heat extraction rates results. Steady state analysis is used. Spray heat transfer coefficients are adjusted to match the sample thermocouple measurements with the same method as used for curve 1.

Heat transfer results are shown in Table 5.6. Spray heat transfer coefficients and heat fluxes are very close for two curves at the sample thermocouple temperatures of 400 ^{o}C and 800 ^{o}C. This is because the conductivity is very close for these two curves for temperatures below ^{o}C

850. From 850 $^{\circ}$C to 1230 $^{\circ}$C, the conductivity in Curve 2 is increased greatly to double the conductivity of Curve 1. However, the spray heat transfer coefficient differs by only 3.9% while the spray heat flux differs by 8.2%. These results demonstrate that spray heat extraction ability is not strongly dependent on the ceramic thermal conductivity. This is because the heat extraction ability by the spray from the sample front surface is much larger than that conducted into the ceramic. Therefore, any reasonable uncertainty in the ceramic thermal conductivity should not have much effect on the accuracy of the heat transfer coefficients extracted from the wet experiments using the current modeling methodology.

5.3.3 Thermocouples Effect during Induction Heating

It is interesting and necessary to know if the thermocouple measurements are affected by the magnetic field. Specifically, will Faraday induction or induction heating happen in the thermocouples? And how do these two phenomena affect thermocouple measurements?

An experiment was done at CINVESTAV to clarify these mysteries. The experiment setup is shown in Figure 5.19. The ceramic body is changed to a ceramic rod which is inserted into the induction coil. The contact between the rod and the coil is avoided by insulating the rod with insulation tape. Two thermocouples (TC2, TC3) are located at the same positions as those in the spray cooling experiments. The platinum sample is excluded from the ceramic rod to avoid introducing another heat source which may affect thermocouple measurements. The experiment was done without spraying and with controlling total power. The total current and two thermocouple measurements are shown in Figure 5.20. Interesting phenomena are observed in Figure 5.20. TC2 and TC3 measurements increase as the total current increases. TC2 measurement almost follows total current measurement while TC3 increases gradually. Since

there are no other heat sources, thermocouple measurements are definitely affected by magnetic fields.

Two hypotheses can explain this problem: 1) Faraday induction induces voltage in the thermocouple wires, which is captured and represented in temperature measurement. 2) Induction heating really exists inside the thermocouple wires or bead.

Hypothesis one can be eliminated by the following reasoning. Reason 1: if hypothesis one is true and it is the only one that causes the problem, TC2 and TC3 signals should have glitches similar to those in current signal and TC2 and TC3 should go flat where the current signal goes flat. However, there is only one glitch in TC2 signal and no obvious glitch in TC3 signal in Figure 5.21(a). And as shown in Figure 5.21(b) TC3 increases gradually as current stays flat. Reason 2: if hypothesis one is true, there will be a voltage induced in the TC wire. This voltage is an AC voltage with 2.5 MHz frequency. Thermocouple measurement has no way to respond to such a high frequency. Then the average value is measured, where average value is 0 and does not affect thermocouple measurement. Therefore, hypothesis one is not the cause.

Hypothesis two is highly possible since thermocouple wires and bead are conductive materials where induction heating should exist. A simple model is created to simulate this experiment. As shown in Figure 5.22, thermocouple bead and thermocouple wire are added to the ceramic rod domain. For the sake of simplification, thermocouples are along the axial direction instead of being perpendicular to it. No thermocouple wire cover is considered and perfect contact between thermocouple and ceramic is assumed. The thermocouple beads consist of Chromel and Alumel. The properties of these two materials are shown in Table 5.7. Thermocouple wire (0.48mm in diameter) uses the average value of these two materials. AC power electromagnetics is active in entire domains while heat transfer is only active in the

ceramic rod and thermocouples domains. A heat transfer coefficient of 10 W/m^{2}K is used at natural convective boundaries. The total current measurement history is input in COMSOL. Transient simulation results of TC2 and TC3 are shown in Figure 5.23. The simulated TC2 curve shape follows the measured TC2 curve, especially for the glitches (as shown in the close-up Figure 5.24) and the large decrease instantly after the current was turned off. The simulated TC3 curve increases gradually just like the measured TC3 curve behaves. The reason for no perfect match between the measurements and simulations is this model is oversimplified. The thermocouples, in reality, cut across the cylinder ceramic body instead of going along the axial direction, which is taken in the model. However, the model as well as the results effectively proves hypothesis two is right.

A serious problem comes as the hypothesis two is confirmed that if the induction heating in sample thermocouple will affect the sample thermocouple temperature measurement. Three thermocouples are added to spray cooling experiment model domain, as shown in Figure 5.25. Here, the average values of thermocouple materials properties are used. An example case with a sample thermocouple temperature of 700 ^{o}C from a wet test is taken. The total current is 484.6A. The spray heat transfer coefficient is 7900W/m^{2}K, and the ceramic thermal conductivity is 0.35W/mK. Temperature predictions with and without thermocouples, at the positions where thermocouples are located, as well as measurements are compared in Table 5.8. Sample thermocouple temperature predictions are not affected whether thermocouples is active in modeling. TC2 and TC3 give closer predictions with thermocouples active in the modeling domain. Heat generated in the sample is 288W; heat generated in TC1, TC2 and TC3 is 0.04W, 0.052W and 1.9E-4W, respectively. Heat generation in TC1 is much smaller than that in the sample. Therefore, there is no need to worry TC1 measurement is affected by itself.

Since the thermocouple orientation and heat transfer conditions between thermocouple and ceramic body are very complicated, it is very difficult and unrealistic to simply create thermocouples in the modeling domain and expect accurate predictions. For convenience and simplicity, the thermocouples in the ceramic in the modeling of the wet experiments were ignored and only TC1 measurement was matched.

Tables

Prediction	Measurement	Error
103	100	3
187	200	−13
294	300	−6
398	400	−2
499	500	−1
603	600	3
704	700	4
813	800	13
920	900	20
1013	1000	13
1101	1100	1
1197	1200	−3

Table 5.1 The Differences between Predicted and Measured

Steady Sample Thermocouple Temperatures

TCs	1	2	3	4	5	6	7	8
Position, mm	3	5	10	15	20	25	30	40

Table 5.2 Locations of the Thermocouples along Axisymmetric Line

Mesh (No. of Elements)	Coarse	Fine
	11968	39701
Computation Time, s	40	1140
Sample Thermocouple Temperature Prediction, C	700	704
Spray Heat Transfer Coefficient, W/m^2K	6880	6880
Generated Heat in Sample, W	262	262
Generated Heat in Coils, W	185	184
Heat into Spray, W	225	225
Heat into Cooling Water, W	204	203

Table 5.3 Heat Transfer Results Comparison by Using Different Meshes

Gap size, mm	0.4	0.5	0.6
Spray Heat Transfer Coefficient, W/m^2K	5440	5350	5300
Generated Heat in Sample, W	274	270	266
Generated Heat in Coils, W	167	166	165
Heat into Spray, W	238	234	230
Heat into Cooling Water, W	186	185	184

Table 5.4 Heat Transfer Results for Three Different Gap Sizes

Front Window Heat Transfer Coefficient, W/m²K	7000	5500	4000
Spray Heat Transfer Coefficient, W/m^2K	7080	7100	7140
Heat into Spray, W	228	229	230
Heat into Cooling Water, W	210	210	211
Heat Taken from the Front Window, W	14	13	12

Table 5.5 Heat Transfer Results for Three Different Front Window Heat Transfer Coefficients

	Spray HTC, W/m^2K			Spray Heat Flux,W/m^2		
Ts(Current)	Curve 1	Curve 2	Relative Difference	Curve 1	Curve 2	Relative Difference
1200(480.9A)	3560	3700	3.9%	4.16	4.5	8.2%
800(474.9A)	5830	5820	-0.2%	4.34	4.4	1.4%
400(484.1A)	13100	13150	0.4%	4.42	4.44	0.5%

Table 5.6 Heat Extraction Comparison for the Two Calibrated Ceramic Curves for Sample

Thermocouple Temperatures of 400 °C, 800 °C and 1200 °C at Heating

	Chromel	Alumel
Conductivity,1/ohm*m	1.40E+06	3.40E+06
Conductivity,W/mK	19.3	29.7
Cp,J/kgK	448	502
rho,kg/m^3	8730	8600

Table 5.7 Material Properties for Chromel and Alumel

	With TCs	Without TCs	Measurements
TC1=	698	698	699
TC2=	134	112	151
TC3=	36	34	61

Table 5.8 Thermocouples Predictions and Measurements at the Sample of 700 °C

Figures
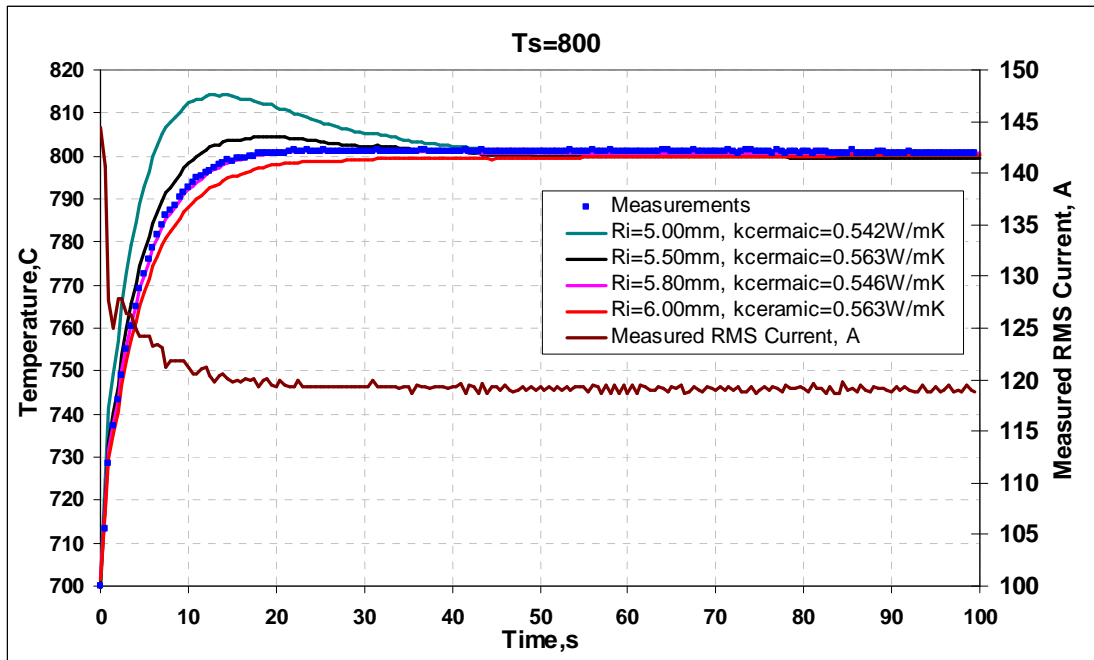
Fig. 5.1 Transient Simulation of Sample Thermocouple Temperature

for Different Coil Loop Inner Radius
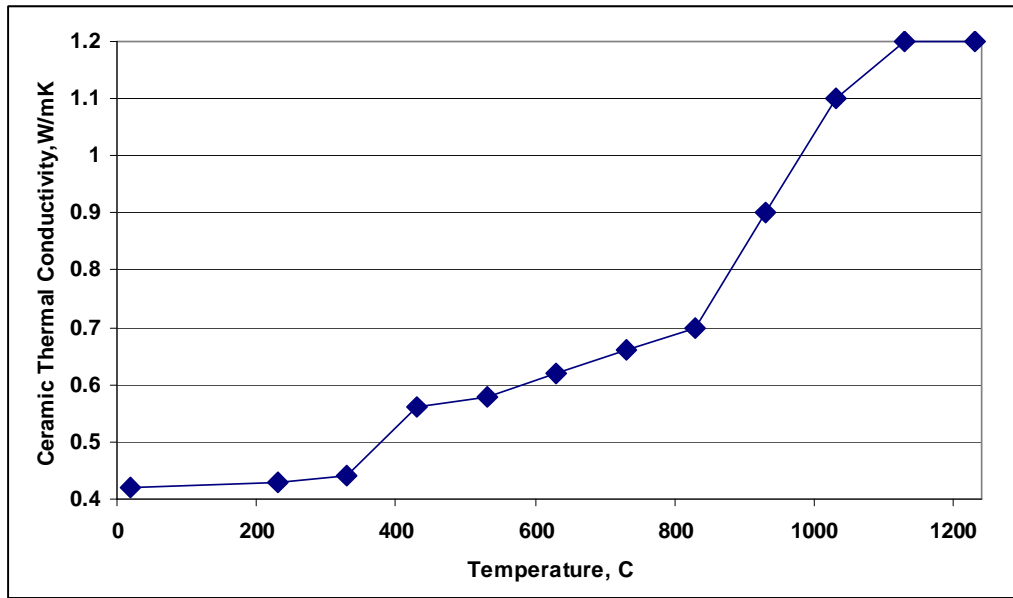
Fig. 5.2 Calibrated Temperature Dependent Ceramic Thermal Conductivity
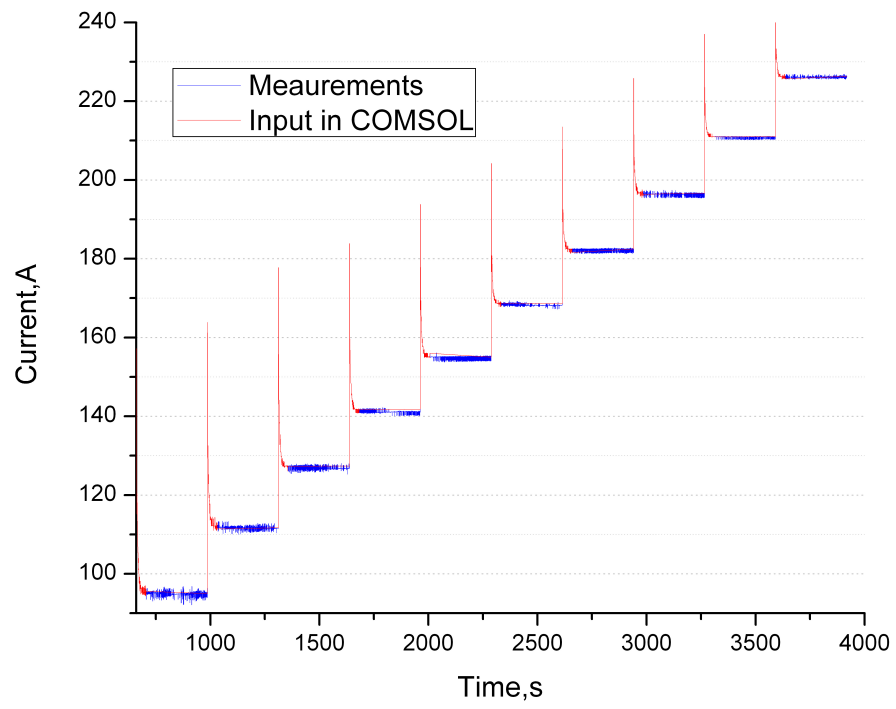
Fig. 5.3 Measured Current from Dry Experiment and the Current Used in COMSOL
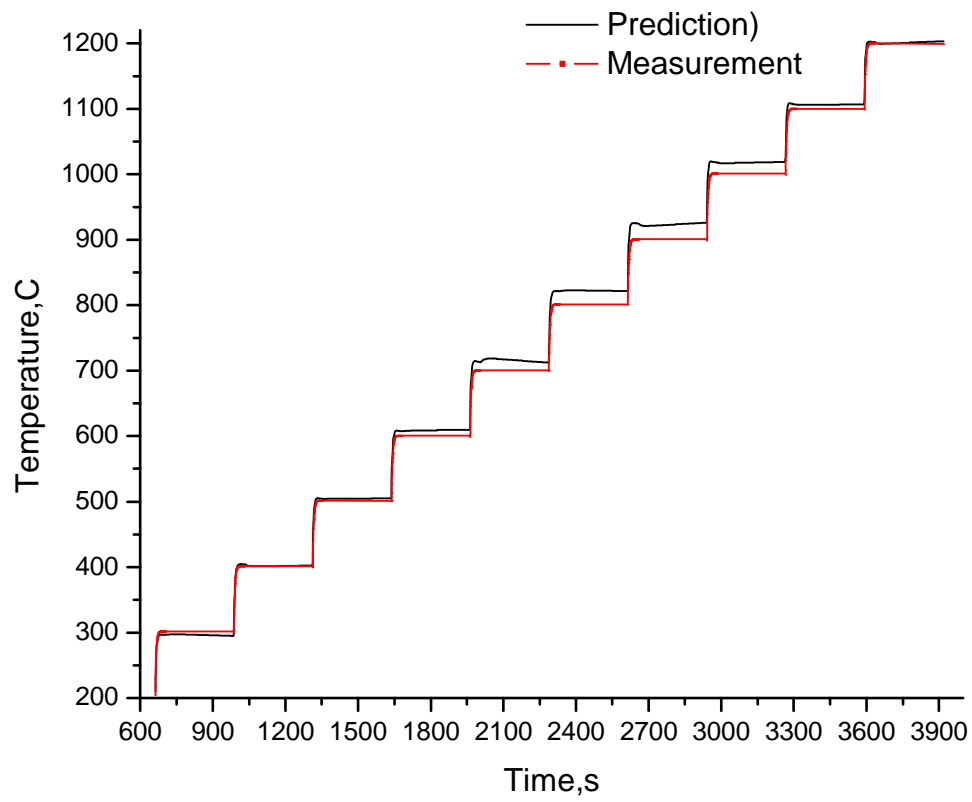
Fig. 5.4 Comparison between Sample Thermocouple Temperature Measurements and

Predictions for Dry Experiment
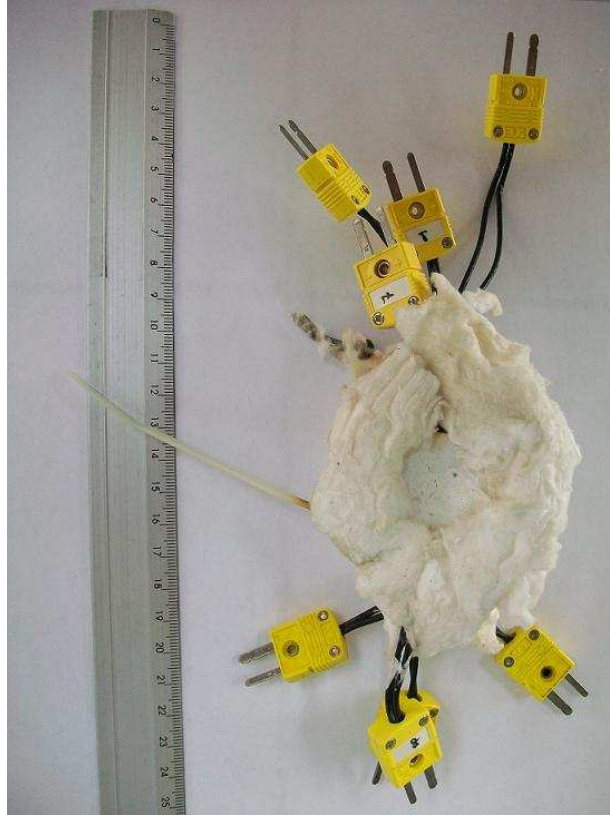
Fig. 5.5 Ceramic Thermal Conductivity Measurement Assembly (Cylinder Ceramic Body, Insulator and Thermocouples)
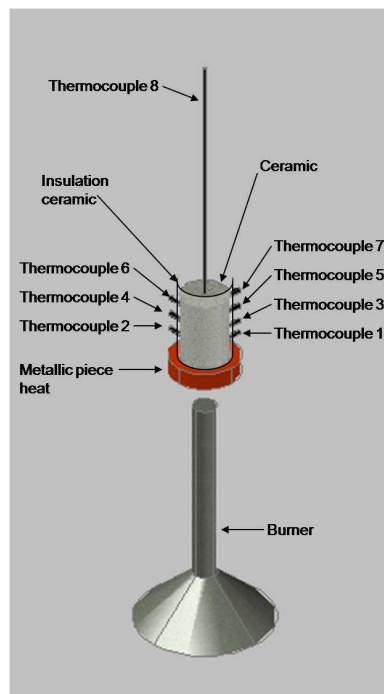
Fig. 5.6 3-D Schematic of the Assembly
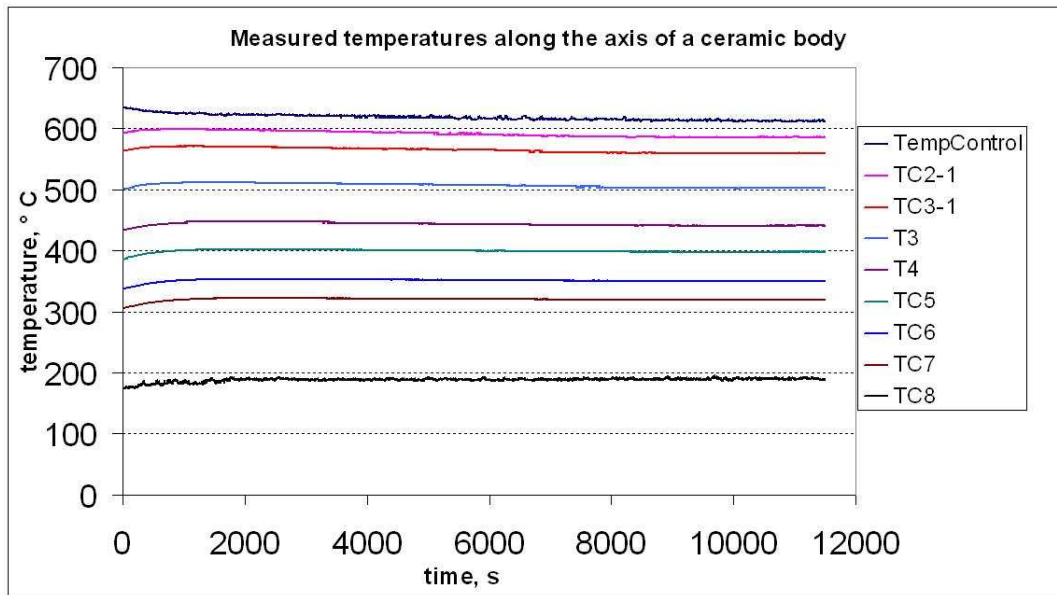
Fig. 5.7 Typical Thermocouple Measurements
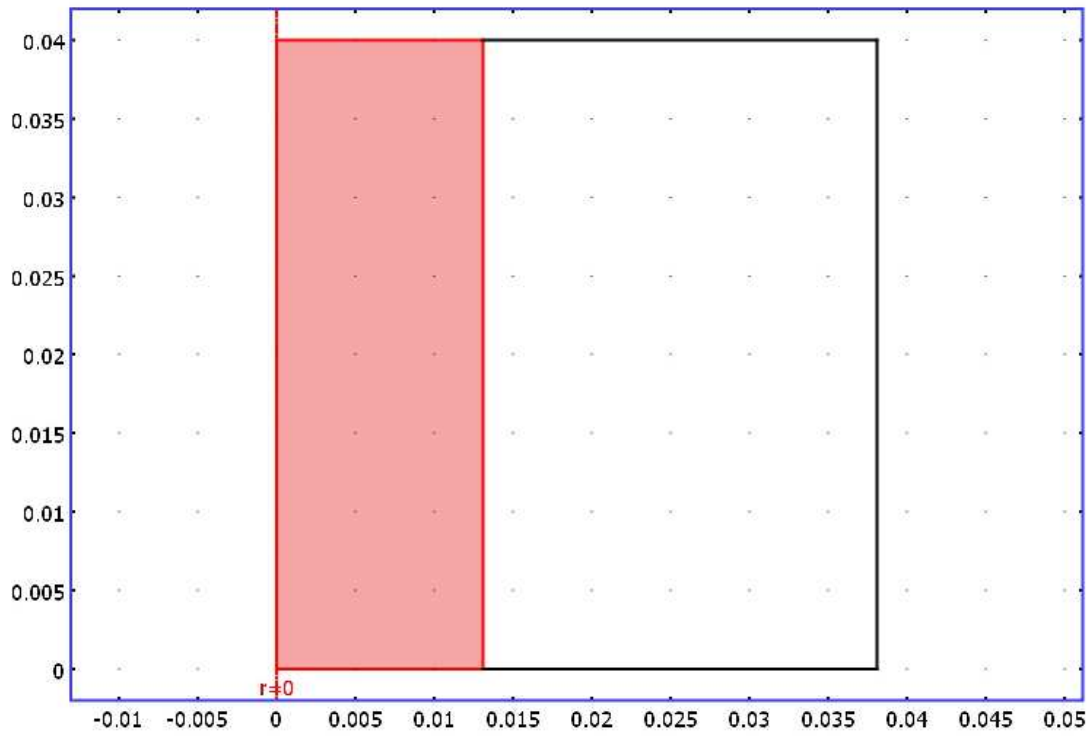
Fig. 5.8 Ceramic Measurement Experiment Modeling Domain, Dimensions (m) and Boundary Conditions in COMSOL
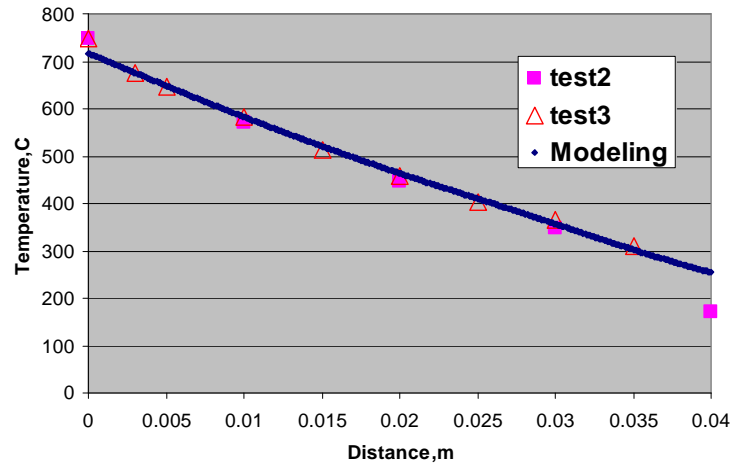
(a)
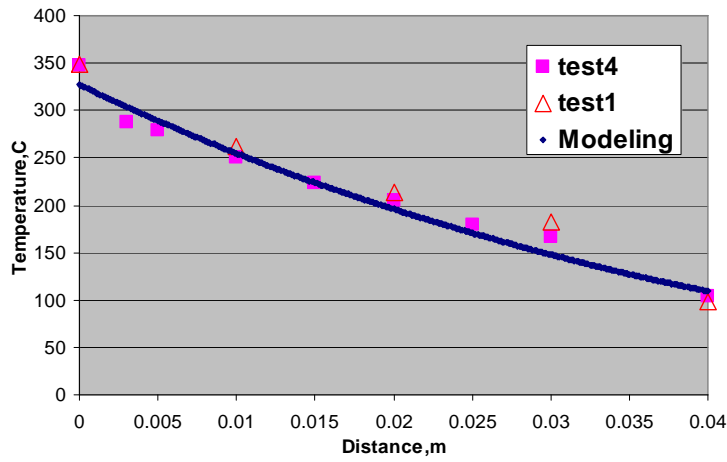
(b)
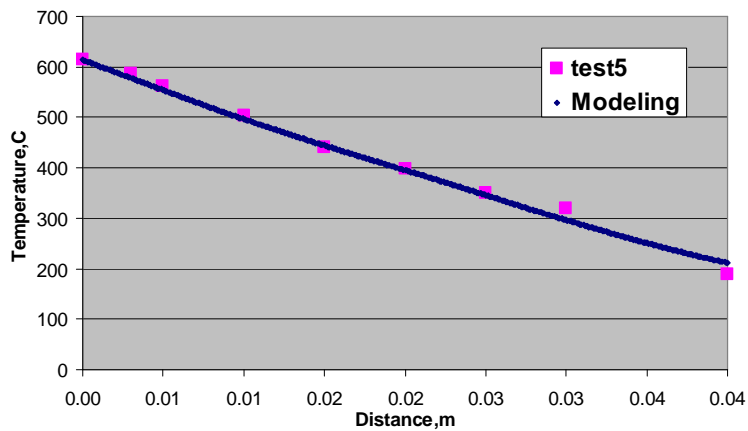
(c)

Fig. 5.9 Thermocouple Temperatures Comparison between Model Prediction and the
Measurements for Five Tests
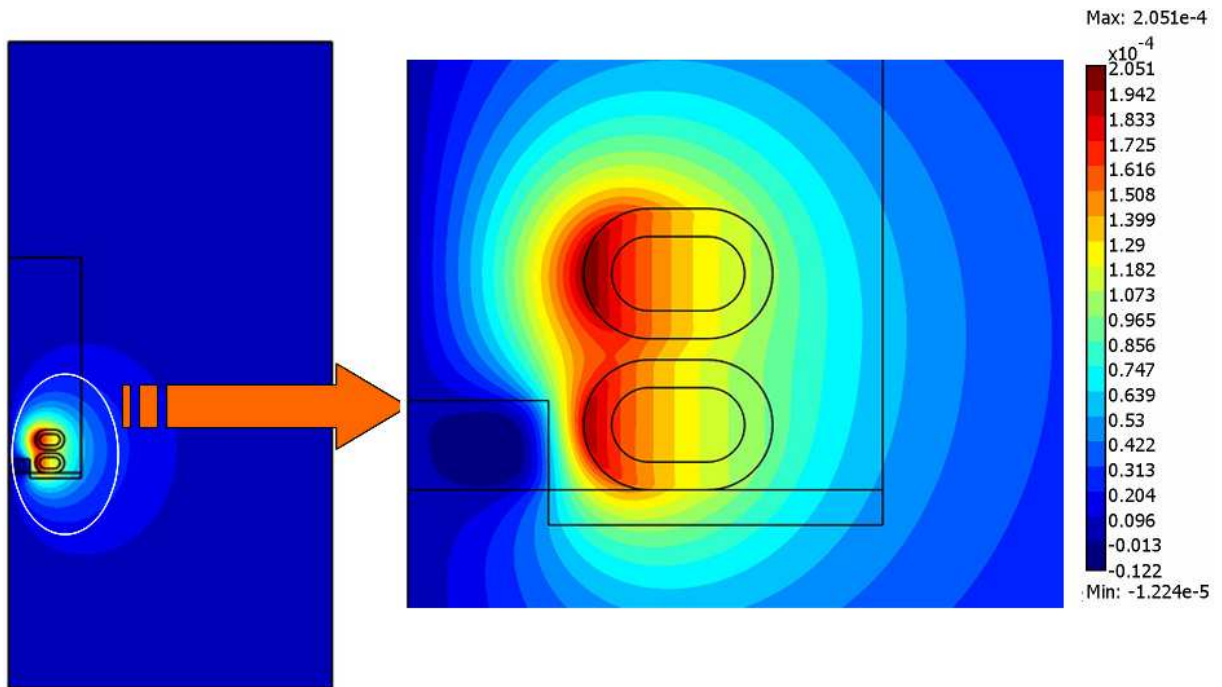
Fig. 5.10 Magnetic Potential Distribution for Sample Thermocouple Temperature of 700 ^{o}C: left) Entire Domain; right) Closeup near Bottom Region of Ceramic Cylinder

Fig. 5.11 Norm Magnetic Flux Density Distribution and Skin Depth for Sample Thermocouple Temperature of 700 ^{o}C: left) entire domain; right) Closeup near Bottom Region of Ceramic Cylinder

Fig. 5.12 Induced Current Density Distribution inside Induction Coils and The Sample for Sample Thermocouple Temperature of 700 $^{\circ}$C
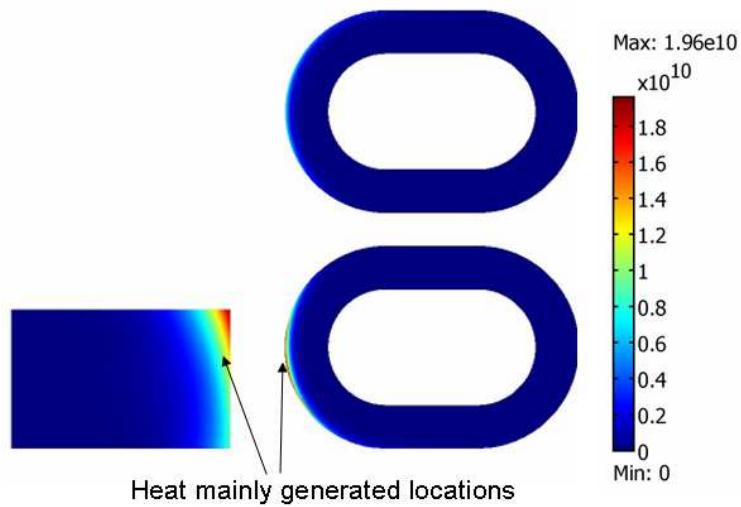
Fig. 5.13 Heat Source Distribution inside Sample and Induction Coils for Sample Thermocouple Temperature of 700 $^{\circ}$C
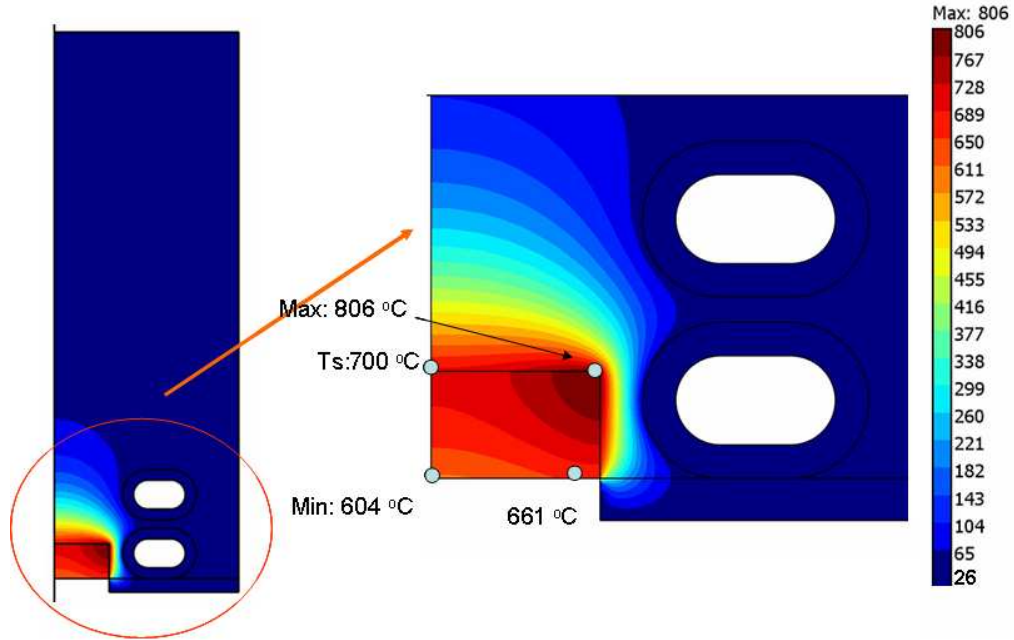
Fig. 5.14 Temperature Distribution in Heat Transfer Domain for the Sample Thermocouple
Temperature of 700°C: left) Entire Ceramic Cylinder Domain; right) Closeup near Front Region
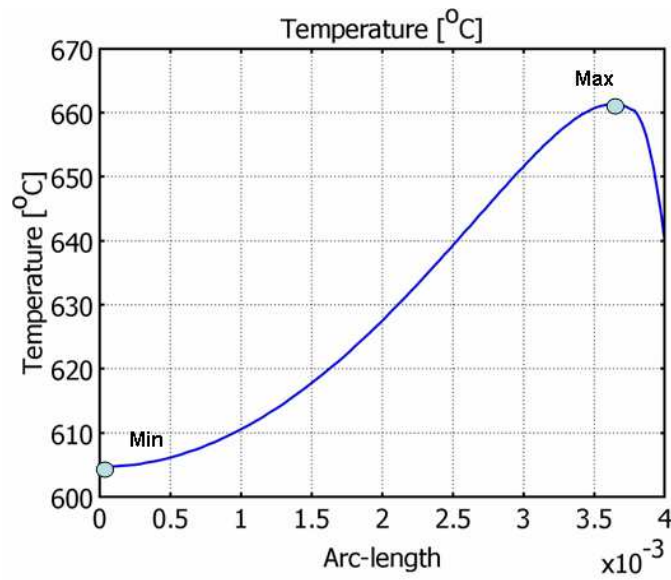
Fig. 5.15 Temperature Distribution along the Frontal Sample Surface for Sample Thermocouple
Temperature of 700 $^\circ$C
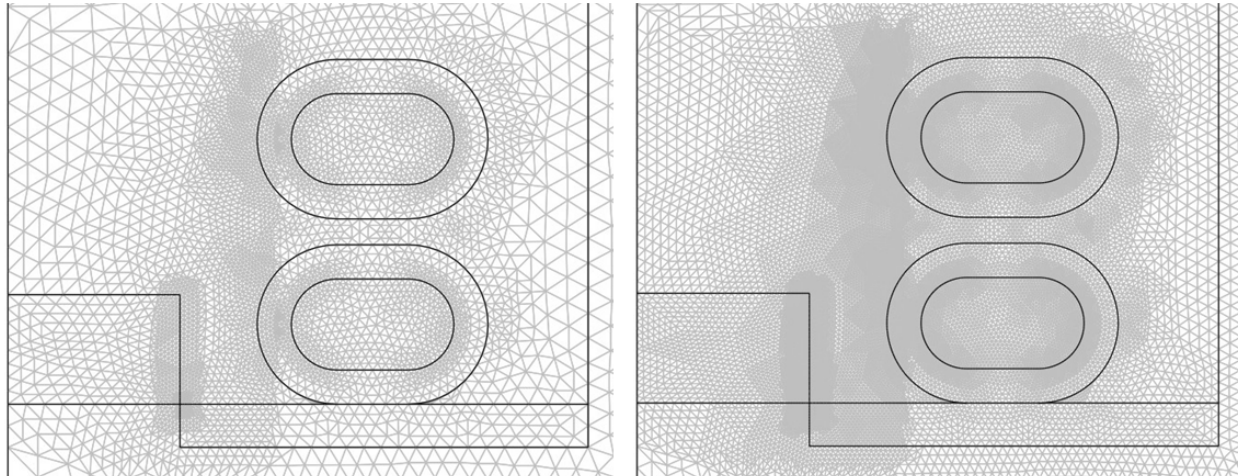
Fig. 5.16 Coarse and Fine Meshes Comparison
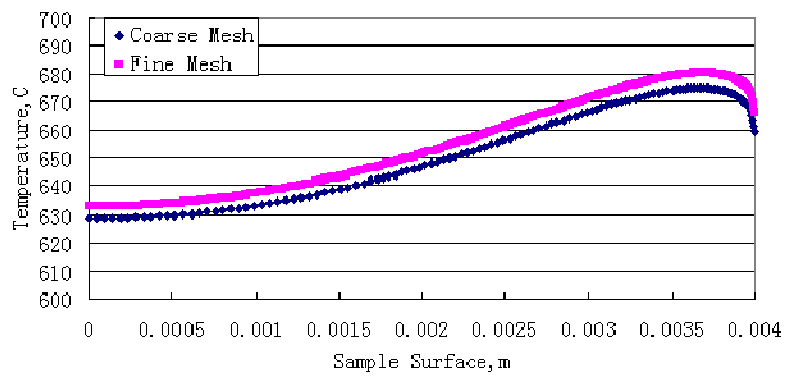
Fig. 5.17 Sample Front Surface Temperature Distribution Comparison
by Coarse and Fine Meshes
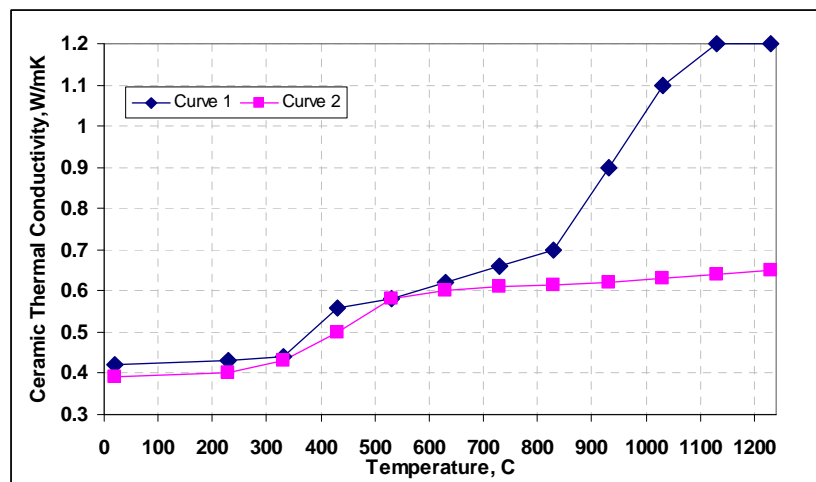
Fig. 5.18 Two Calibrated Temperature Dependent Ceramic Thermal Conductivity Curves
(Curve 1 with emissivity from Fig. 4.4; Curve 2 with emissivity=1)

Fig. 5.19 Experiment Setup for Investigation Magnetic Field Effect on Thermocouples
Measurements
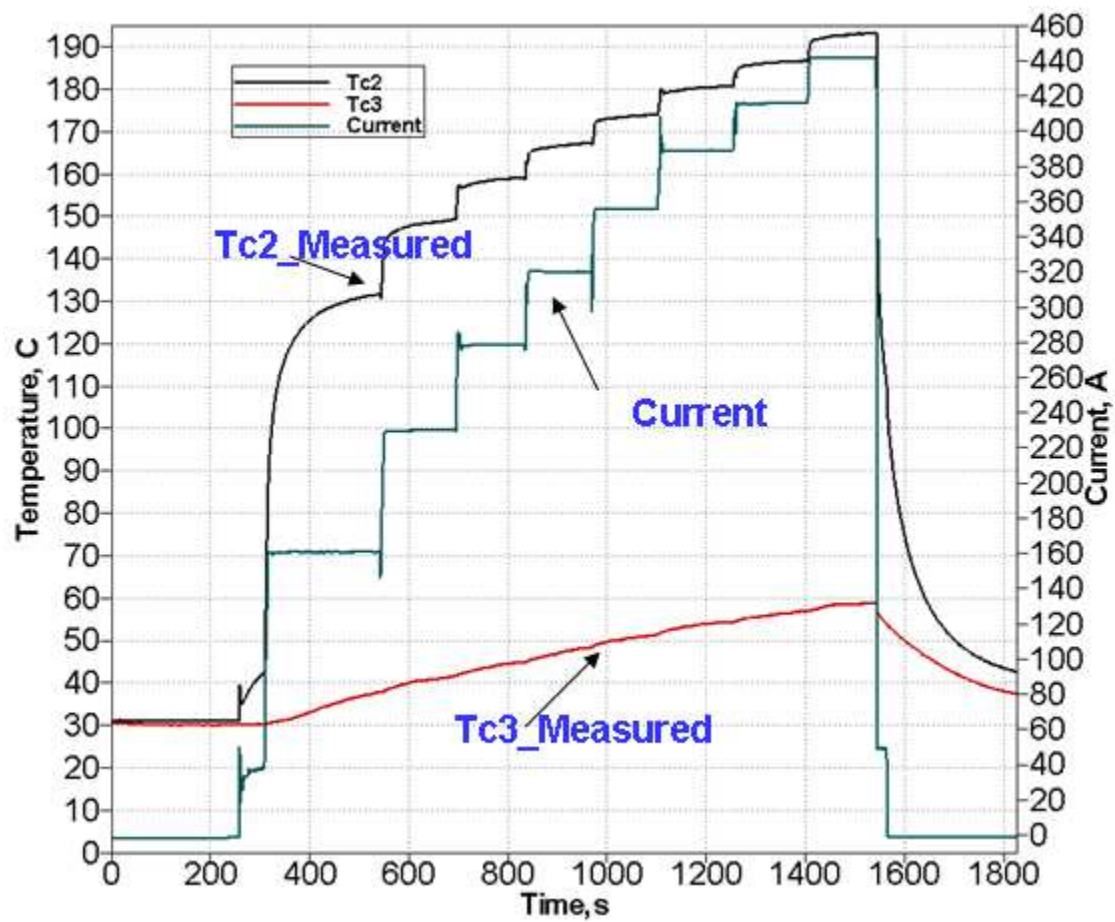
Fig. 5.20 Total Current and Two Thermocouple Measurements

(a)

(b)
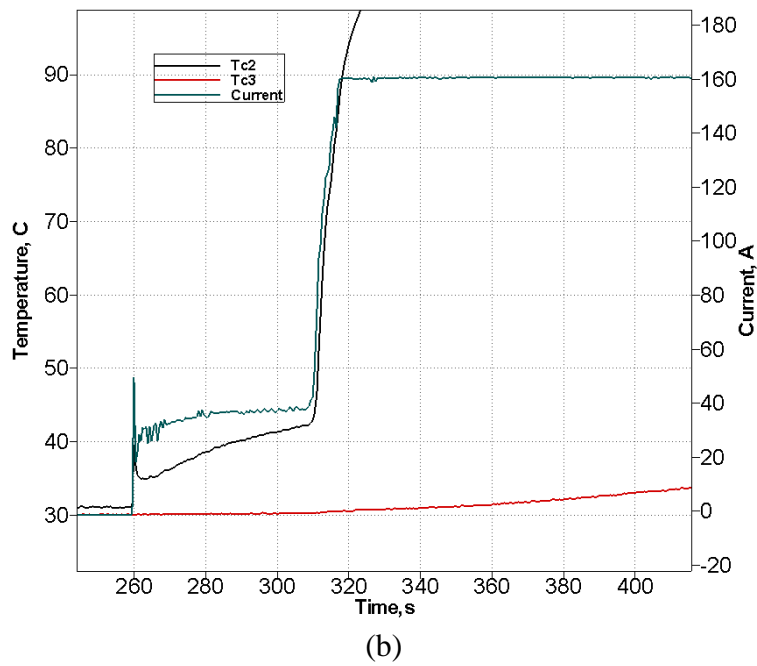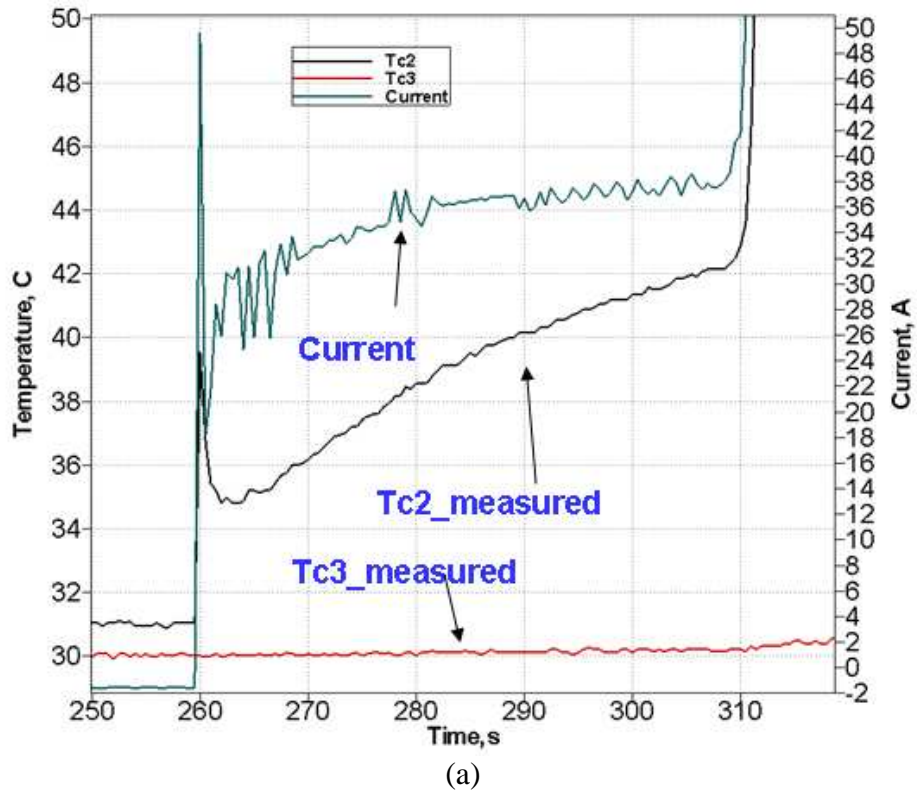
Fig. 5.21 Close-up Total Current and TC2 and TC3 Measurements
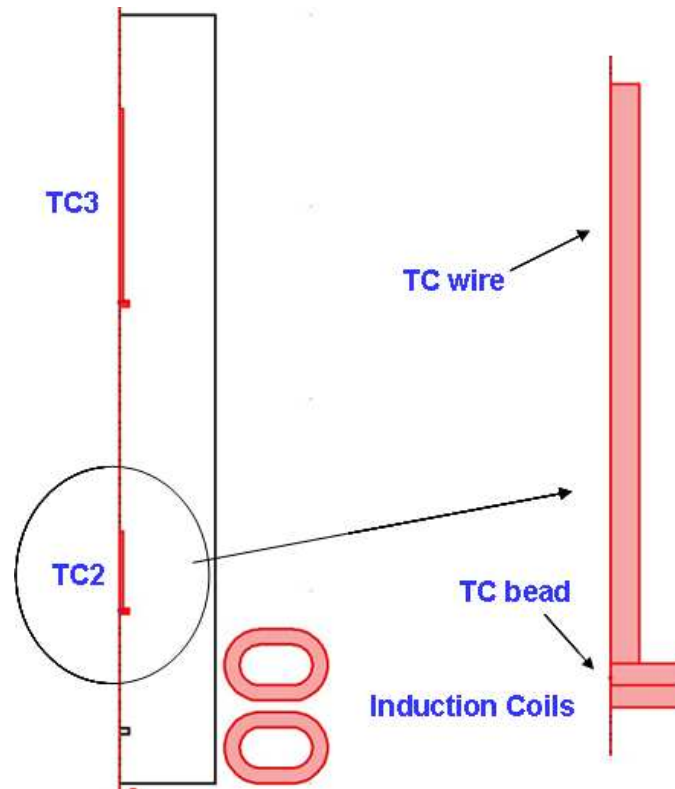
Fig. 5.22 Modeling Domain with Thermocouples
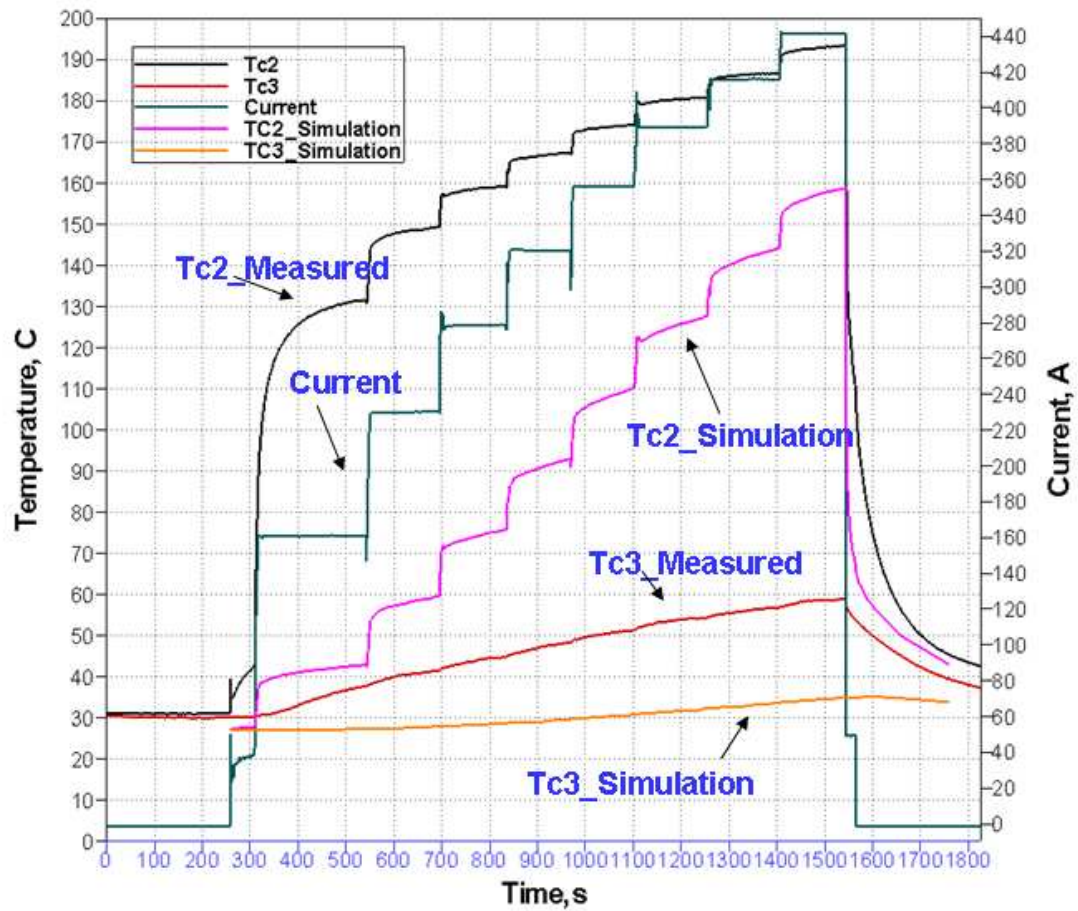
Fig. 5.23 Comparison between Transient Simulation Results of TC2 and TC3 and Measurements
(Please refer to Section 5.3.3 for the explanation of the discrepancy
between measurements and predictions)
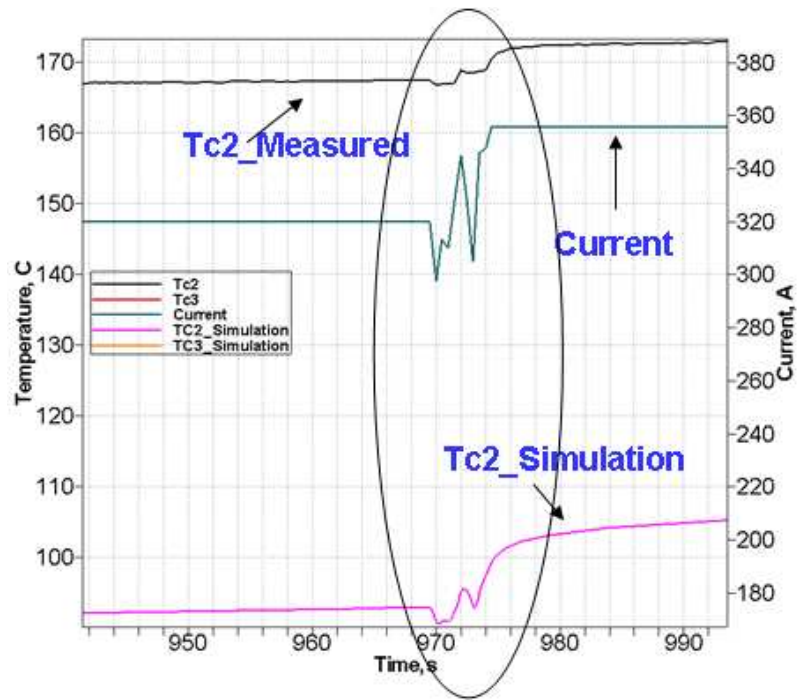
(a)
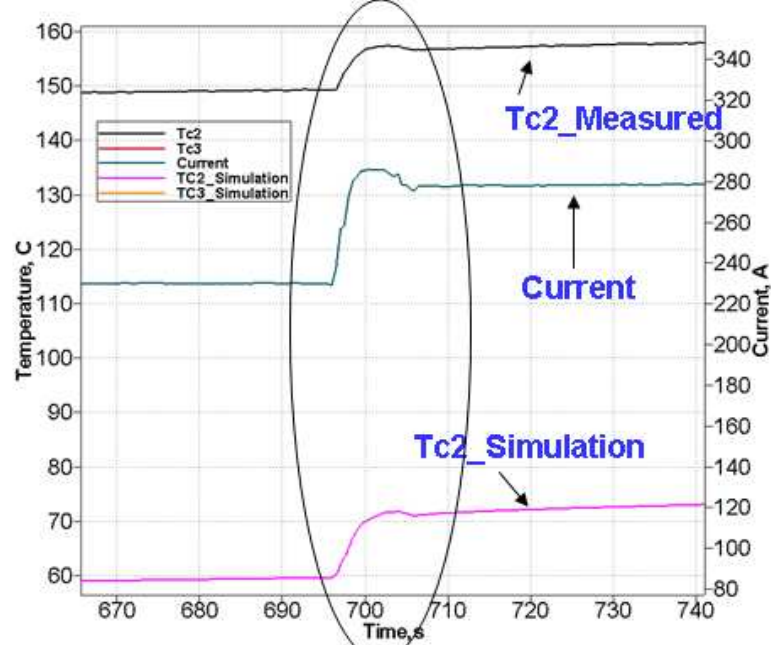
(b)

Fig. 5.24 Close-up of Figure 5.12 for Glitches Observation
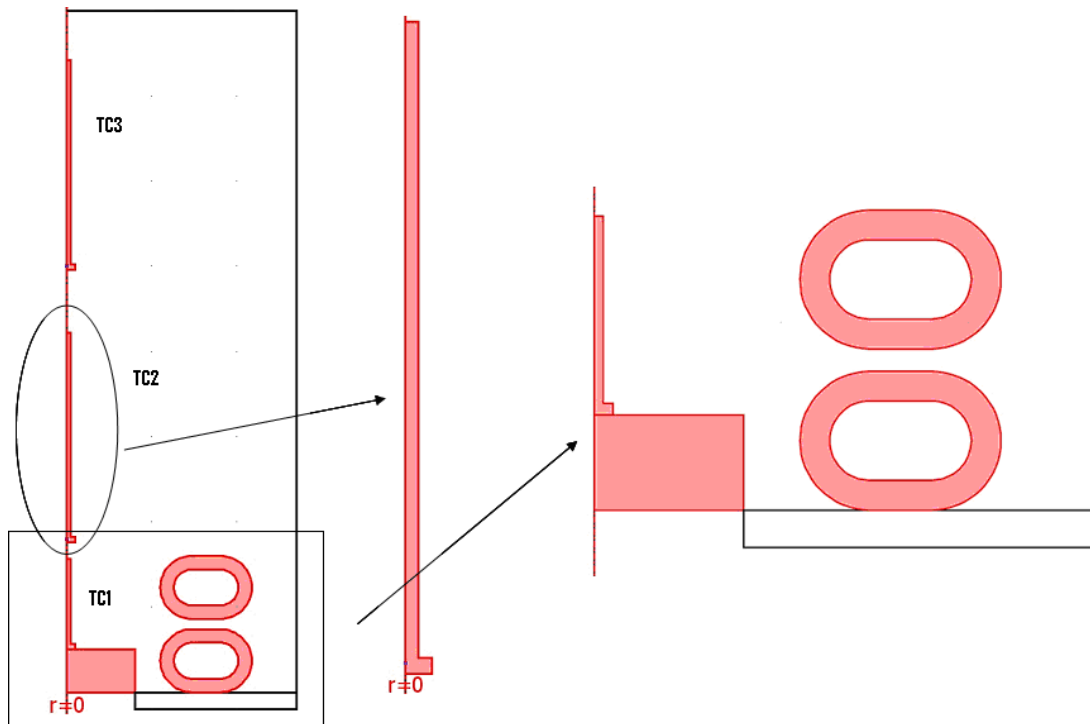
Fig. 5.25 Modeling with Thermocouples in Spray Cooling Experiments Simulation

Chapter 6: Wet Experiments Modeling Results and Discussions

As discussed in Section 5.2, for wet experiment modeling, the materials properties in Table 4.1, the calibrated ceramic thermal conductivity and the loop inner radius are used. The current is taken from the average value of the last 30 seconds for each sample thermocouple temperature. Air convection heat transfer coefficient is 10W/m2K. The heat transfer coefficient of the cooling water through the copper coil is estimated by Sleicher&Rouse relation. Spray heat transfer coefficient is chosen to match the temperature prediction with the sample thermocouple measurement using steady state simulation.

6.1 Input and Output Data for Modeling All Wet Experiments

Every sample thermocouple temperature in the wet experiments was modeled using steady state induction heating. Table 6.1 gives an example of the input data and output results for modeling a typical experiment with nozzle operating conditions: water flow rate=3.5lpm; air flow rate=95lpm; nozzle centered. Specific heat transfer boundary conditions including spray heat transfer coefficients, as well as the total current, are clearly shown in Table 6.1. I_tot/loop is the total current for each loop. h_spray is the spray heat transfer coefficient. h_front is the heat transfer coefficient used at the front window. h_air is the calibrated natural convective heat transfer coefficient. T_cw is the cooling water temperature. Tcoil is the mean temperature over the induction coil. The output results of spray heat flux and power loss through the front window are also shown in Table 6.1. Pspray is the power taken away by the spray. Pfront is the power taken away by the spray from the front window. Tsurf_min and Tsurf_max are the minimum and maximum sample surface temperatures, respectively. Other input and output data for all wet experiments modeling are presented in Appendix B for reference.

6.2 Spray Heat Transfer Coefficients and Fluxes for Different Conditions

Spray heat transfer coefficients versus sample surface temperatures for the three sets of nozzle flow rates are shown in Figure 6.1. The sample surface temperature is always a little lower than the sample thermocouple temperature, especially as the spray heat transfer coefficient increases, and so the results in Figure 6.1 (and Figure 6.2-6.6) are plotted against the surface temperature to be more relevant. The surface temperatures for those figures are obtained by averaging the maximum and minimum sample surface temperatures. The associated maximum and minimum surface temperatures are shown as x-error bars in those figures. Increasing water flow rate increases heat transfer coefficient. During heating, the heat transfer coefficient peaks around 150~200 ^{o}C, then decreases as sample surface increases. During cooling, heat transfer coefficient keeps decreasing gradually. Hysteresis is clearly present in the heat transfer coefficient curves. The associated spray heat fluxes versus sample surface temperature are shown in Figure 6.2. Increasing temperature difference compensates for the decrease in heat transfer coefficient, so heat flux is more constant with temperature. Increasing water flow rate increases spray heat flux. Spray heat flux also shows hysteresis with heating versus cooling. The minimum heat flux, ie. Leidenfrost temperature, is found at around 850 ^{o}C. The spray heat transfer rate results from both the current steady state measurement and previous transient measurements [52] are compared, as also shown in Figure 6.2. Steady measurements give more than about 3 times higher heat flux than transient measurements. The reason is that transient experiments started with a high sample (which actually is steel) temperature and then quenched the steel plate by water spray. Time was too short for establishing steady state heat transfer during transient experiments. Water droplets impinged on the steel surface, bounced off before boiling and took

86

less heat away compared to steady state experiments, where droplets have time to form intimate contact, get boiled and take away a lot of heat.

Spray heat transfer coefficients and spray heat fluxes for three different sample positions (Y=0mm, 9mm, 18mm) are shown in Figure 6.3, 6.4, 6.5, 6.6, respectively. Hysteresis exists for different location from spray centerline. Moving further away from spray centerline decreases heat transfer coefficient. All results highly suggest the need to correlate heat transfer rates and spray dynamics (droplet distribution, size, velocity, etc, --collaboration work at CINVESTAV, Mexico)

6.3 Proposed Mechanism of Spray Heat Transfer Hysteresis

Hysteresis is clearly observed in the measured spray heat transfer rates. During the heating portion of each experiment, spray droplets impinge on the surface, boil, and take heat away, forming a continuous water layer, as shown in Figure 6.7(a). Spray droplets can easily penetrate this thin water layer, contact the hot surface, get boiled, turn into steam and take much heat away, which gives large heat fluxes. However, during cooling experiments, which start at high sample surface temperature (>~860 ^{o}C), a stable steam layer has formed on the sample surface, in addition to a thick water layer on top the steam layer, as shown in Figure 6.7 (b). Spray droplets are easily absorbed or bounce off this water layer and have great difficulty to penetrate it. They cannot impact the hot surface, and thus rarely achieve good enough contact to boil and remove much heat. Thus, heat flux is low. The low thermal conductivity of this steam layer acts acts as a barrier to heat transfer to maintain a heat removal rate that is roughly 50% lower than during heating. This steam layer survives to low temperatures before droplets finally can penetrate through, disrupt the vapor barrier, and return to the high heat transfer rates

encountered during heating experiments. Therefore, a difference appears in heat transfer at intermediate temperatures according to history (heating versus cooling).

6.4 Evaluation and Comparison with Nozaki Correlation

As shown in Figure 3.7, seven different water flux rates at three locations were measured. A wet experiment (both heating and cooling) was run for each of these flux rates. So, for each sample thermocouple temperature, heat fluxes can be obtained for all seven water flux rates. Figure 6.8 presents the modeling results for the three sample thermocouple temperatures (600 $^{\circ}$C, 700 $^{\circ}$C, 800 $^{\circ}$C during heating stage). The main trend is that heat flux decreases as the water flux rate decreases. A possible secondary effect is that further away from the nozzle centerline, the heat flux is higher than expected. This is perhaps due to the smaller droplets found in the mist which are able to drift away from the spray centerline, or perhaps due to extra water from the adjacent high flow-rate spray jet impacting at the centerline and running across the surface to augment heat extraction in the low flow-rate extremities of the jet.

The Nozaki empirical correlation is given in Equation 4.29 which correlates spray water flux rate and spray water temperature with spray heat transfer coefficient. The current modeling results of steady wet experiments are compared with Nozaki empirical correlation results (A=1), as shown in Figure 6.8. The Nozaki correlation results compare closely with spray heat transfer coefficients extracted from the current work at the sample surface temperatures of from 600~800 $^{\circ}$C over the water flux rates of 0.2~20l/m^{2}s. Parameter A in the Nozaki correlation is usually set to be 0.25 for the steel caster [66]. The difference is likely due to significant surface oxide scale formation, deep surface roughness, water quality, or other phenomena in the steel caster, which decrease spray heat transfer rate.

Tables

Unit	Ts	Input							Output				
		l_tot/loop	h_spray	h_front	h_air	h_cw	T_cw	Tcoil	Pspray	Spray heat flux	Pfront	Tsurf_min	Tsurf_max
Unit	C	A	kW/m^2K	kW/m^2K	W/m^2K	W/m^2K	C	C	W	MW/m^2	W	C	C
Heat	100	292.5	23.00	5	10	3.59	29	36	72	1.43	2	77	93
	200	443.7	24.20	5	10	3.75	34	39	176	3.50	4	148	185
	300	472.3	17.20	5	10	3.81	37	39	207	4.12	6	236	282
	400	487.1	13.30	5	10	3.78	36	40	225	4.48	7	330	380
	500	489.4	10.50	5	10	3.83	37	40	231	4.60	9	427	480
	600	481.0	8.25	5	10	3.84	38	40	224	4.46	11	530	580
	700	452.0	5.97	5	10	3.80	37	39	195	3.88	13	639	683
	800	454.4	5.22	5	10	3.84	38	40	197	3.92	15	737	780
	900	436.1	4.08	5	10	3.76	36	40	176	3.50	17	843	880
	1000	447.1	3.80	5	10	3.82	37	40	183	3.64	20	940	977
	1100	450.8	3.37	5	10	3.79	36	40	182	3.62	24	1045	1080
	1200	466.9	3.27	5	10	3.80	37	40	193	3.84	27	1141	1178
Cool	1100	463.2	3.65	5	10	3.85	38	42	195	3.88	24	1038	1077
	1000	445.8	3.76	5	10	3.73	37	42	182	3.62	20	943	980
	900	429.7	3.92	5	10	3.77	38	42	170	3.38	17	846	882
	800	452.4	5.17	5	10	3.34	38	42	195	3.88	15	737	780
	700	441.0	5.62	5	10	3.32	37	42	184	3.66	13	642	683
	600	423.2	6.03	5	10	3.34	38	42	167	3.32	11	547	585
	500	384.3	5.83	5	10	3.28	36	42	134	2.67	9	458	488
	400	354.6	6.15	5	10	3.25	35	40	111	2.21	7	366	392
	300	342.8	7.92	5	10	3.23	34	37	103	2.05	5	267	292
	200	356.6	14.20	5	10	3.24	35	37	111	2.21	4	165	190
	100	253.5	15.90	5	10	3.17	33	37	53	1.05	2	84	96

Table 6.1 Input and Output Data for Modeling Experiment with Nozzle Operating Conditions: Water flow rate=3.5lpm; Air flow rate=95lpm; Y=0mm (Case 3)
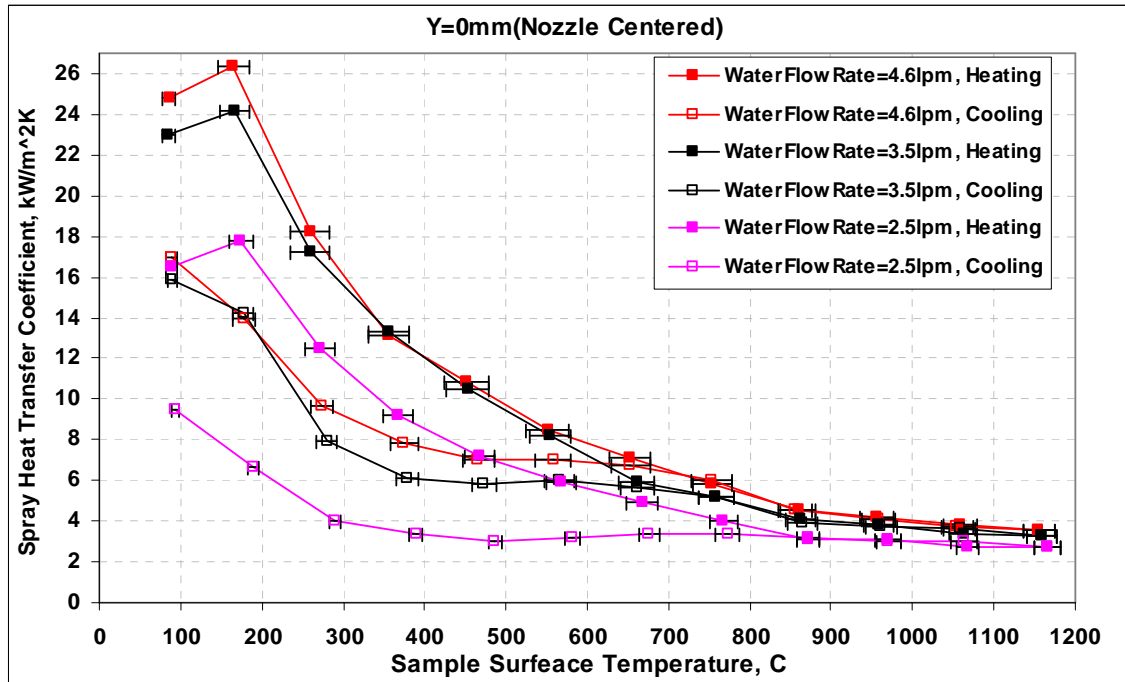
Fig. 6.1 Spray Heat Transfer Coefficients for Different Nozzle Flow Rates As Sample Centered (Y=0mm)
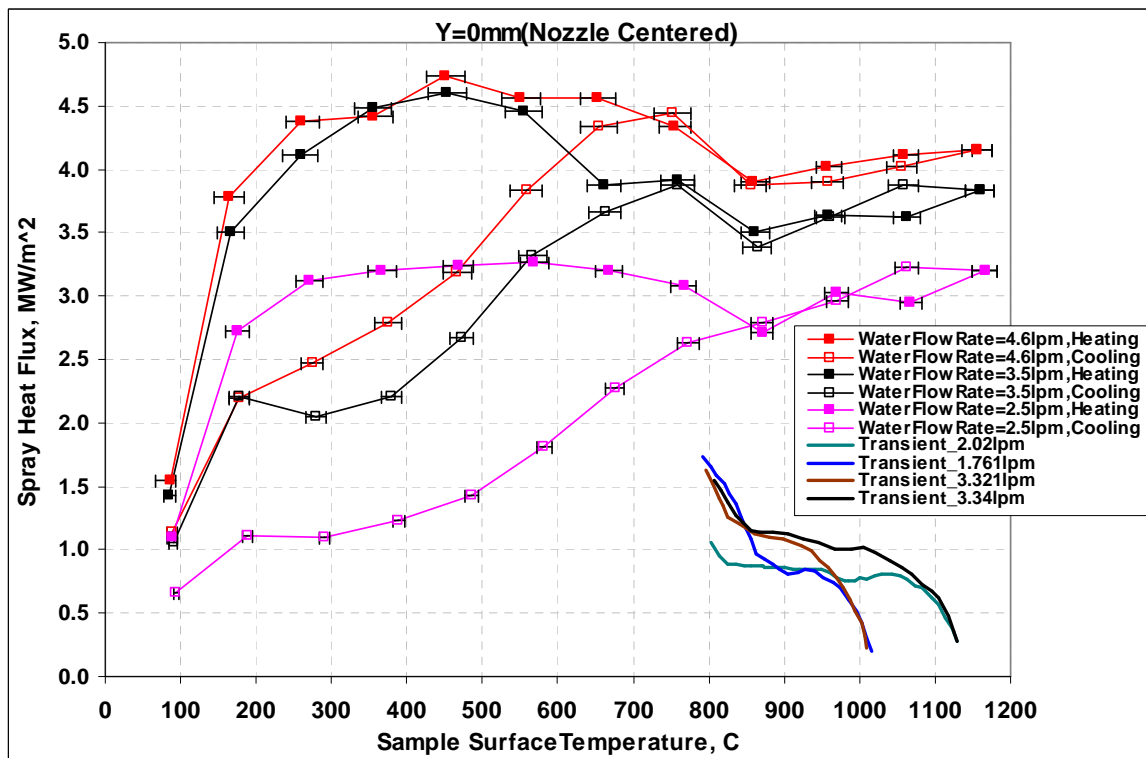
Fig. 6.2 Spray Heat Fluxes for Different Nozzle Flow Rates As Sample Centered (Y=0mm)
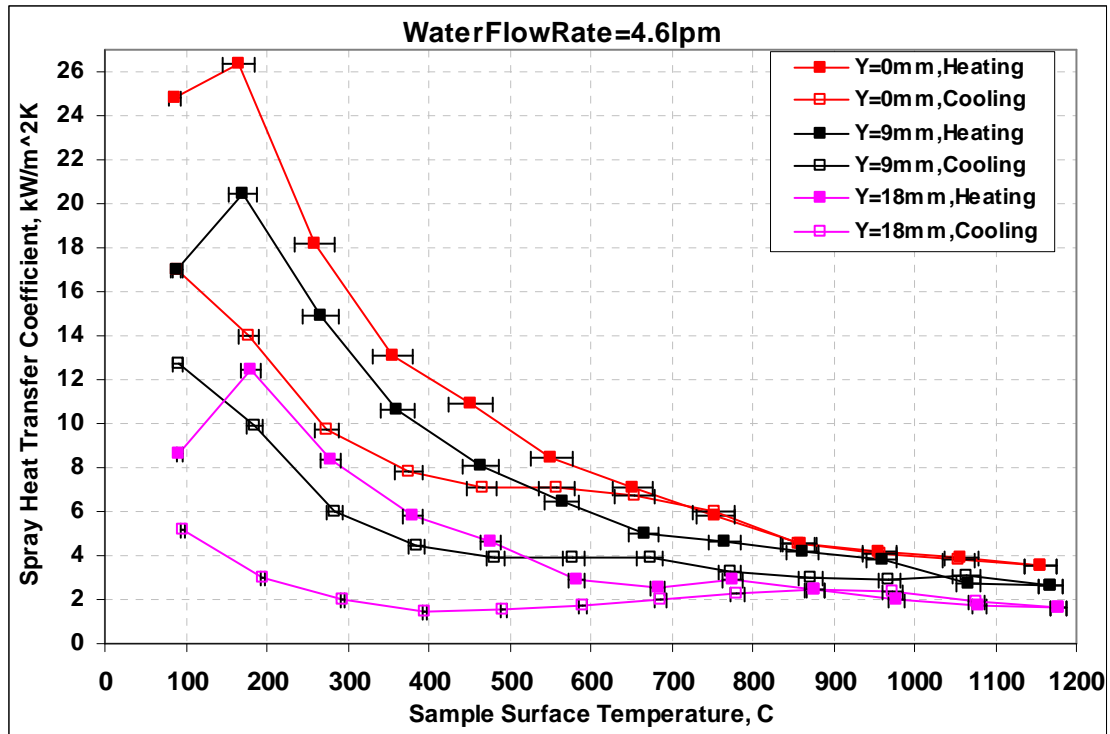
Fig. 6.3 Spray Heat Transfer Coefficients for Different Sample Positions
As Water Flow Rate is 4.6 lpm
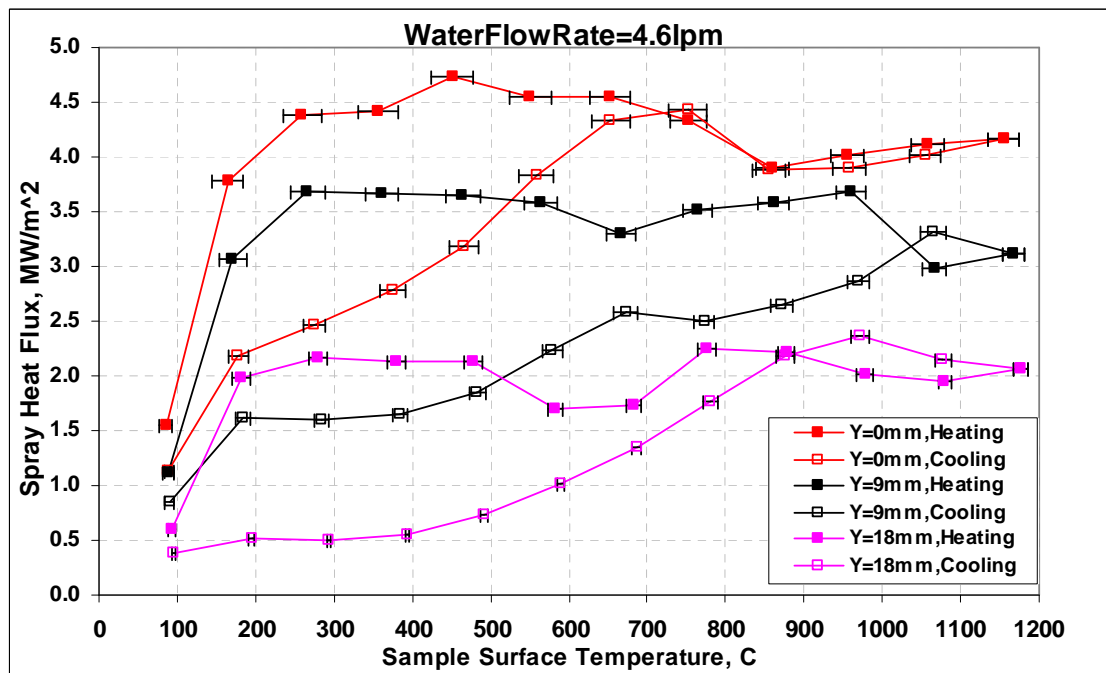
Fig. 6.4 Spray Heat Fluxes for Different Sample Positions
As Water Flow Rate is 4.6 lpm

91
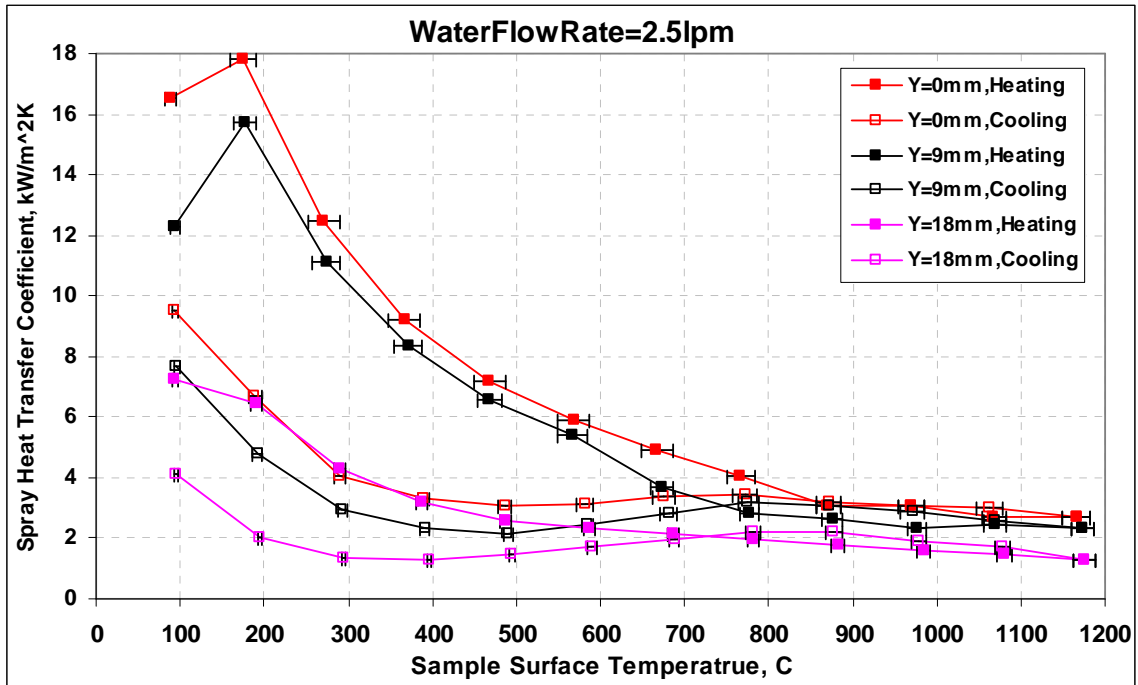
Fig. 6.5 Spray Heat Transfer Coefficients for Different Sample Positions
As Water Flow Rate is 2.5 lpm
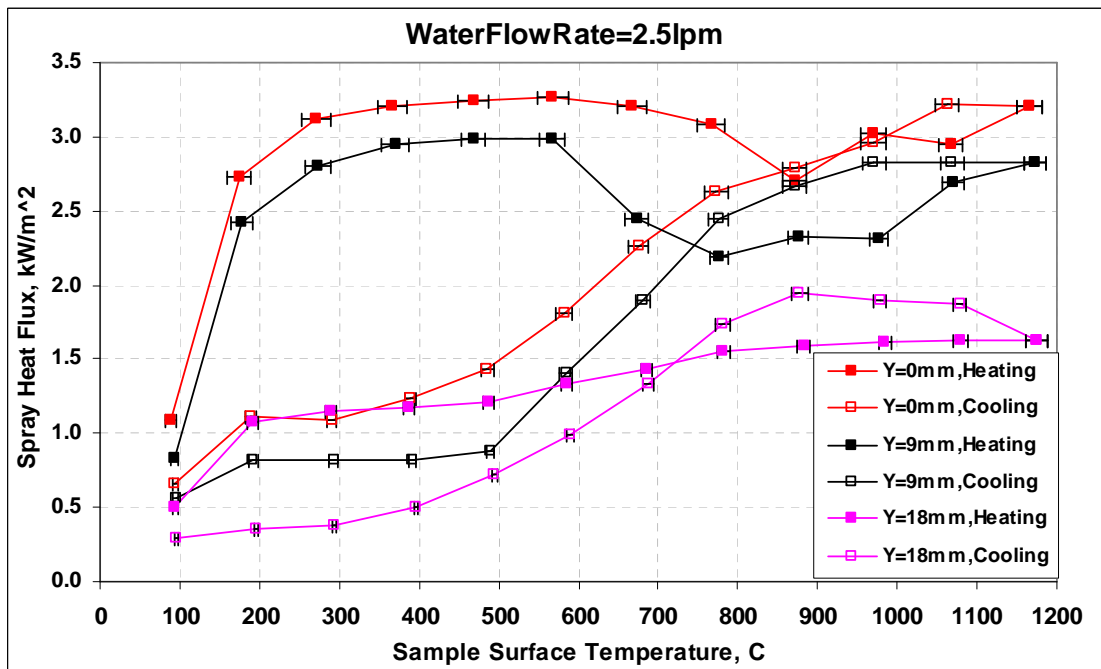
Fig. 6.6 Spray Heat Fluxes for Different Sample Positions
As Water Flow Rate is 2.5 lpm
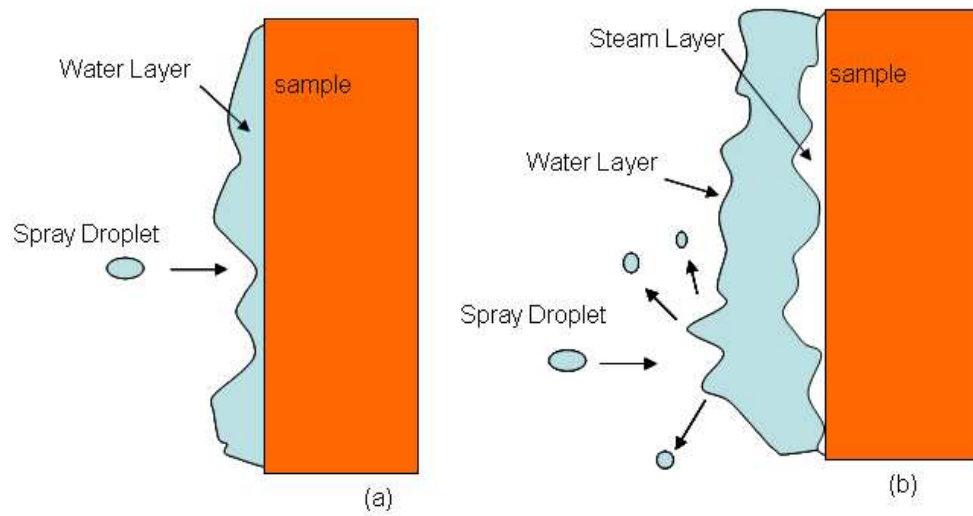
Fig. 6.7 Schematic of Heat Transfer Hysteresis Mechanism
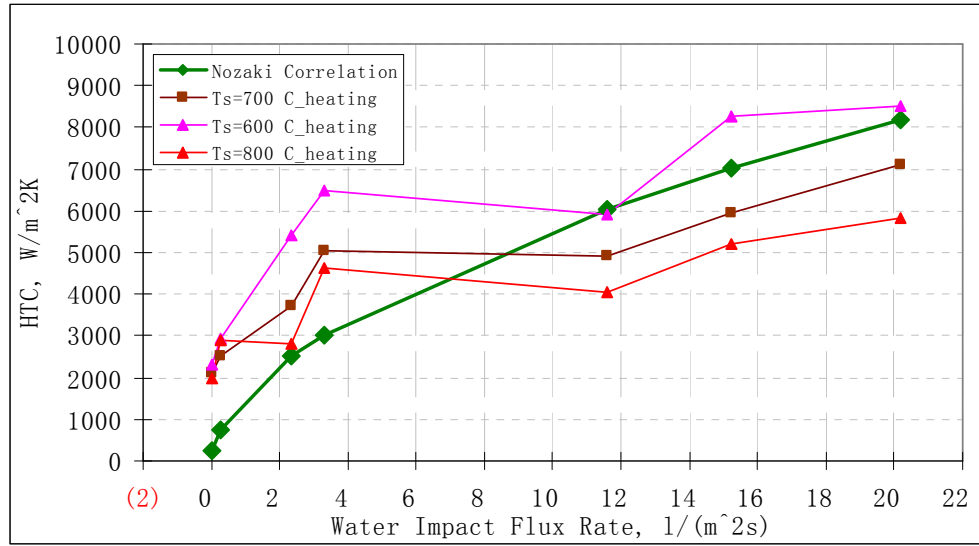
Fig. 6.8 Comparison between Current Modeling Results and Nozaki Correlation Results

Chapter 7: Summary and Future Work

In this work, an experimental apparatus is developed to conduct induction heating to heat up a platinum sample at a specified steady-state sample thermocouple temperature, while being spray-cooled by various nozzle flow rates. A computational model of induction heating using COMSOL is developed, validated, calibrated and employed to extract heat transfer rates of spray water cooling from the steady experiments. The spray heat-transfer coefficient varies from 1000 W/m^{2}K to 26,000 W/m^{2}K for the sample surface temperature ranging from 100 ^{o}C to 1200 ^{o}C. Spray heat transfer rates increase with increasing spray water flow rate. Spray heat transfer rate decreases as the sample moves away from spray centerline, due to the lower water flow. A Leidenfrost temperature exists at around 850 ^{o}C. Heat transfer hysteresis is found to exist between heating and cooling at different nozzle flow rates. Spray heat transfer results compare closely with the Nozaki empirical correlation, but greatly exceed the results of corresponding transient experiments. Oxidization and scale formation are likely to explain the observed lower spray heat extraction rates observed in real casters.

Future work may include:

(a) Lab experiments using steel with surface oxidization, (scale formation layer), roughness, and water quality variations, which happen in the real caster.

(b) Pyrometer temperature measurements in the plant to validate with the heat transfer coefficients from the lab experiments using steel in the experimental apparatus developed in this work.

Appendix A

A. Measured RMS Current and Sample Thermocouple Temperature for Each Case.
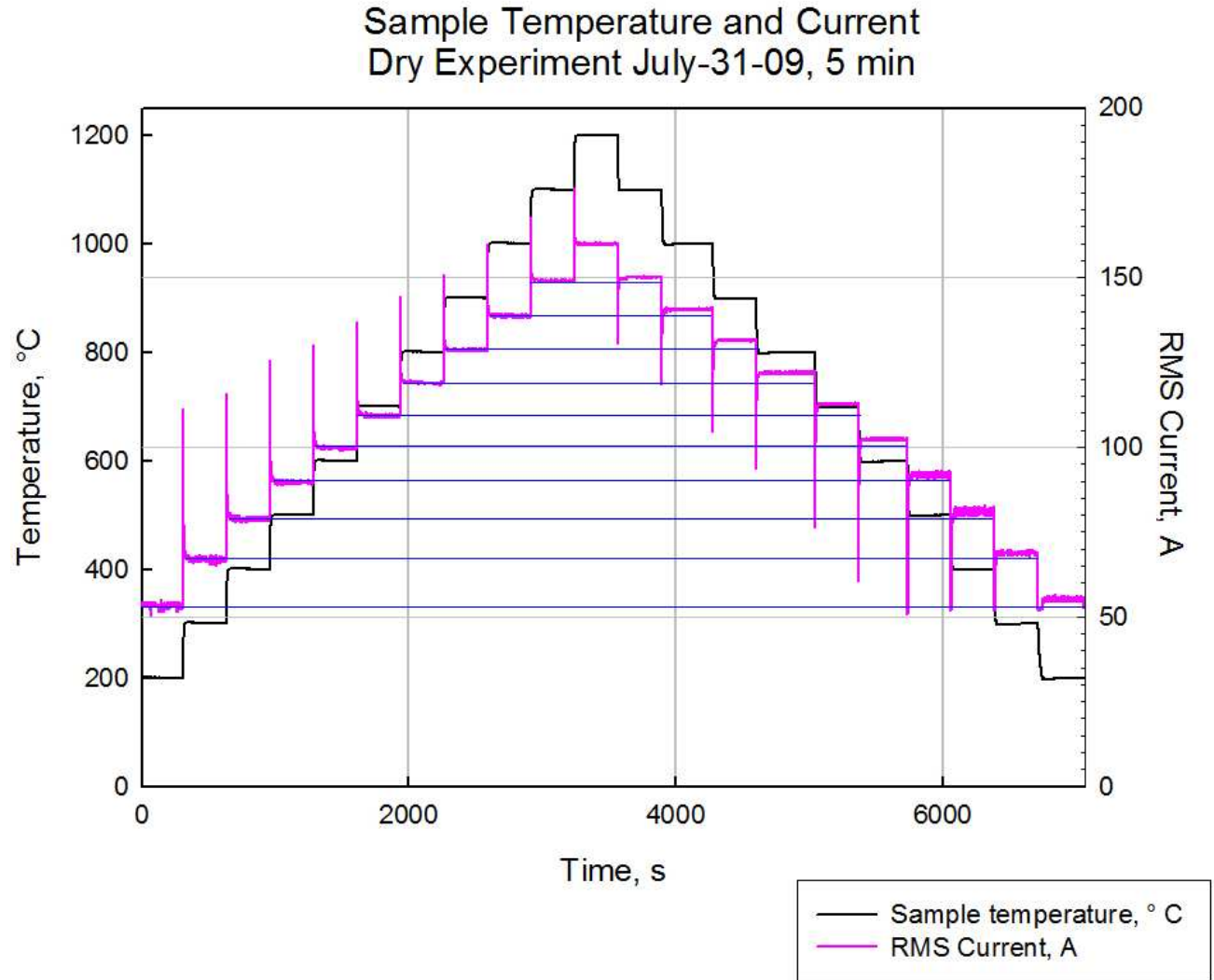
Fig. A-1 Measured RMS Current and Sample Thermocouple Temperature for Case 1

(Dry Experiment)
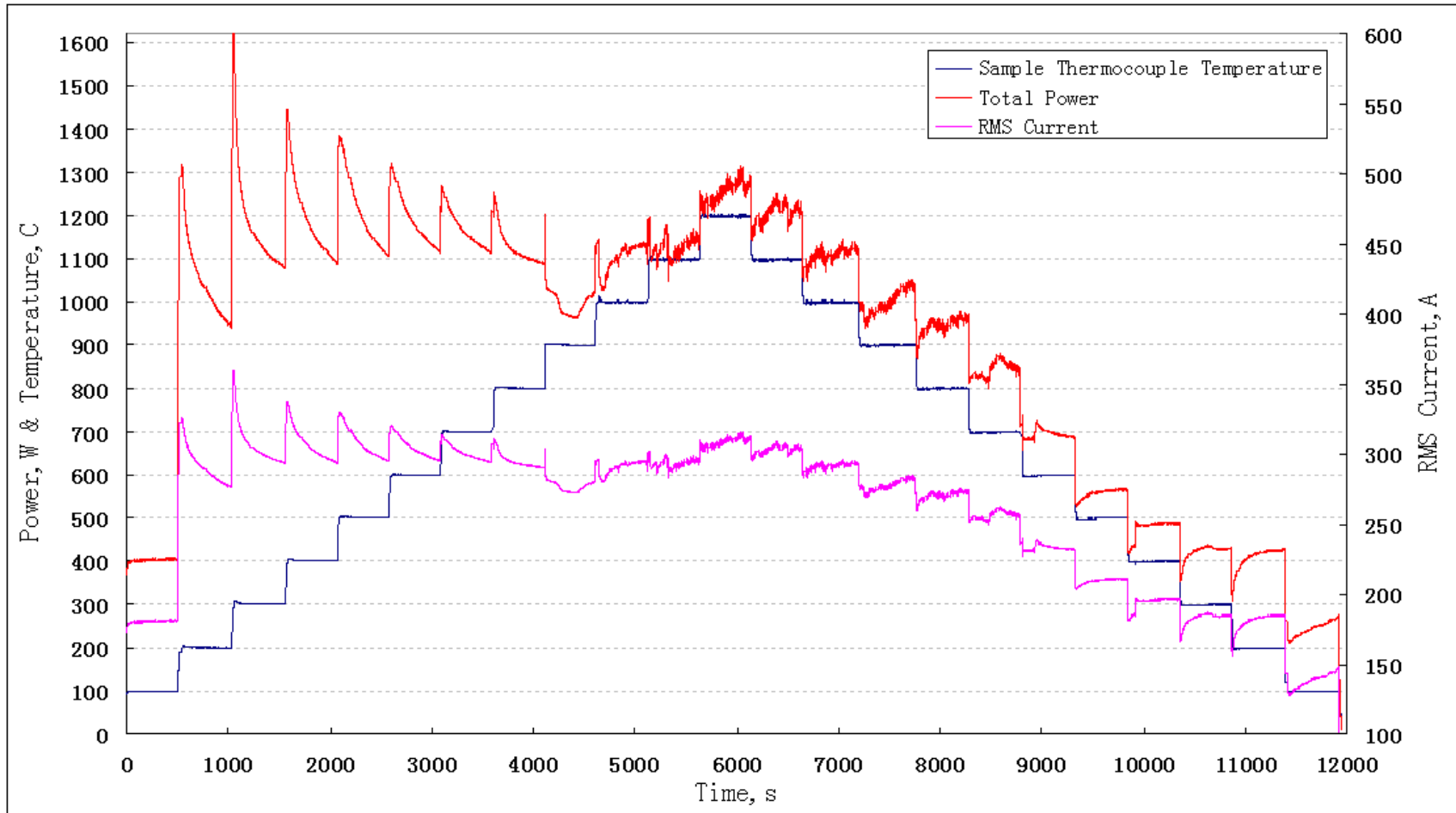
Fig. A-2 Measured RMS Current and Sample Thermocouple Temperature for Case 2
(Wet Experiment, Y=0mm, WaterFlowRate=2.5lpm)
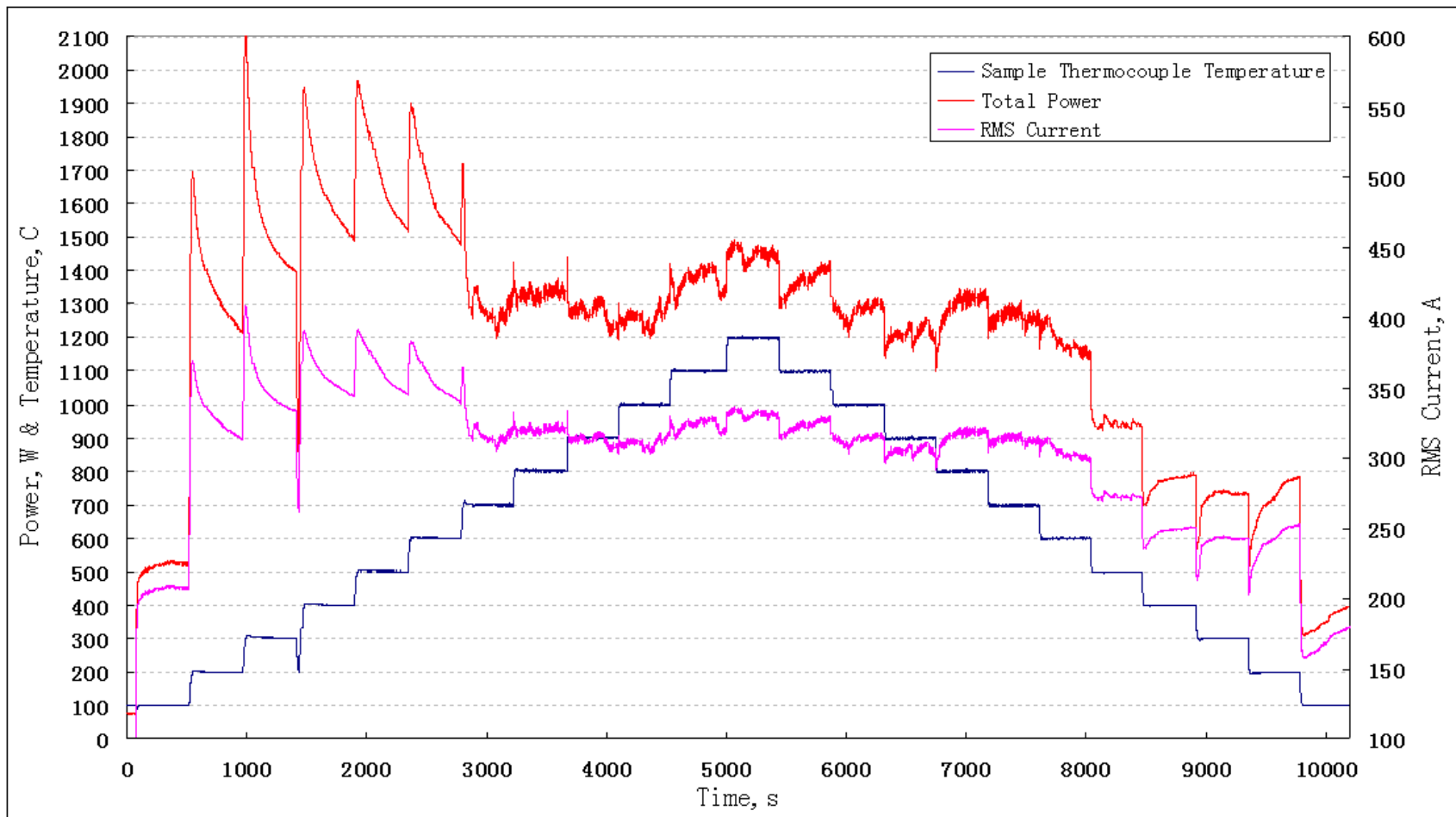
Fig. A-3 Measured RMS Current and Sample Thermocouple Temperature for Case 3
(Wet Experiment, Y=0mm, WaterFlowRate=3.5lpm)
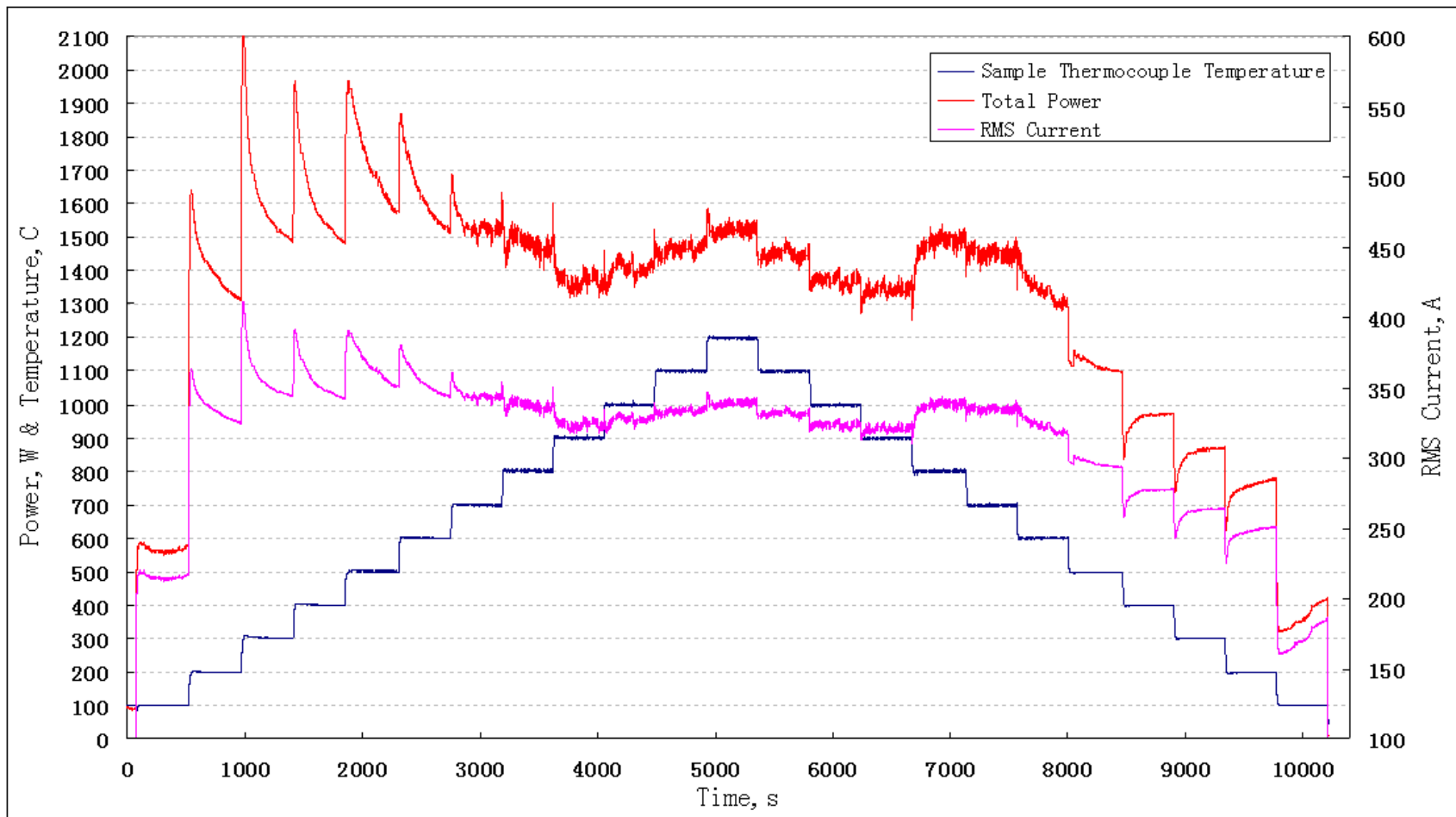
Fig. A-4 Measured RMS Current and Sample Thermocouple Temperature for Case 4
(Wet Experiment, Y=0mm, WaterFlowRate=4.6lpm)
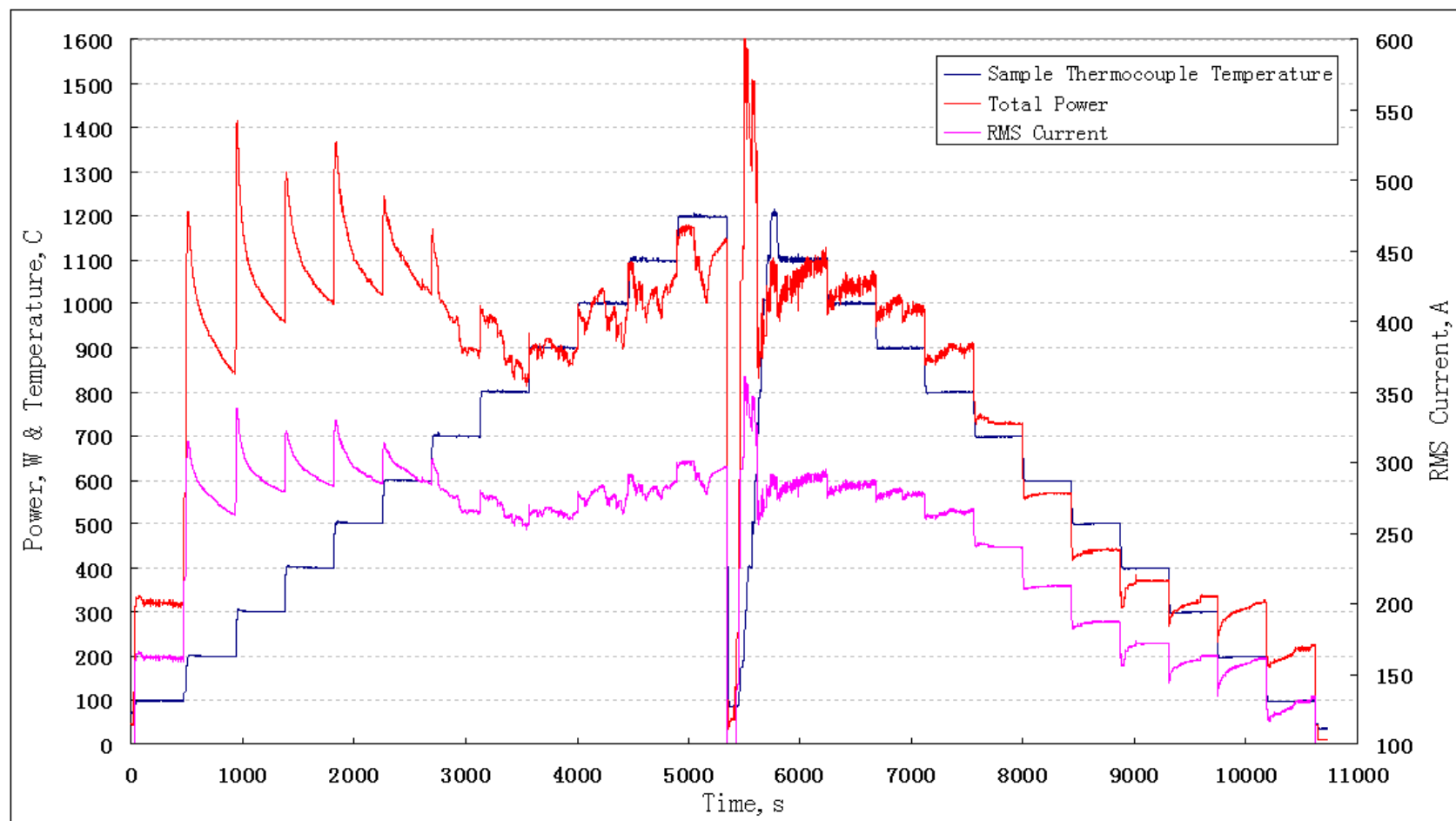
Fig. A-5 Measured RMS Current and Sample Thermocouple Temperature for Case 5
(Wet Experiment,Y=9mm, WaterFlowRate=2.5lpm)
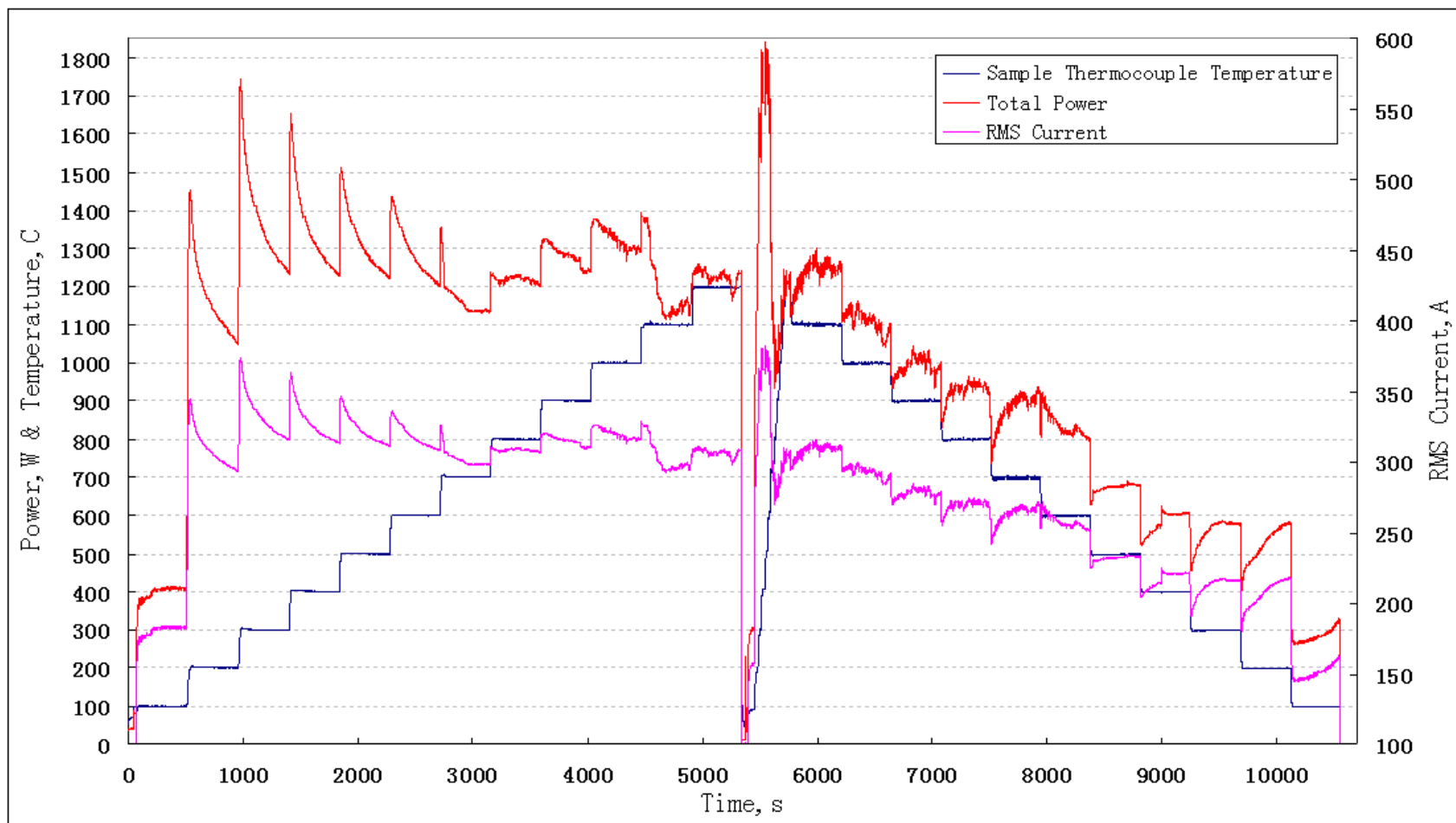
Fig. A-6 Measured RMS Current and Sample Thermocouple Temperature for Case 6
(Wet Experiment, Y=9mm, WaterFlowRate=4.6lpm)
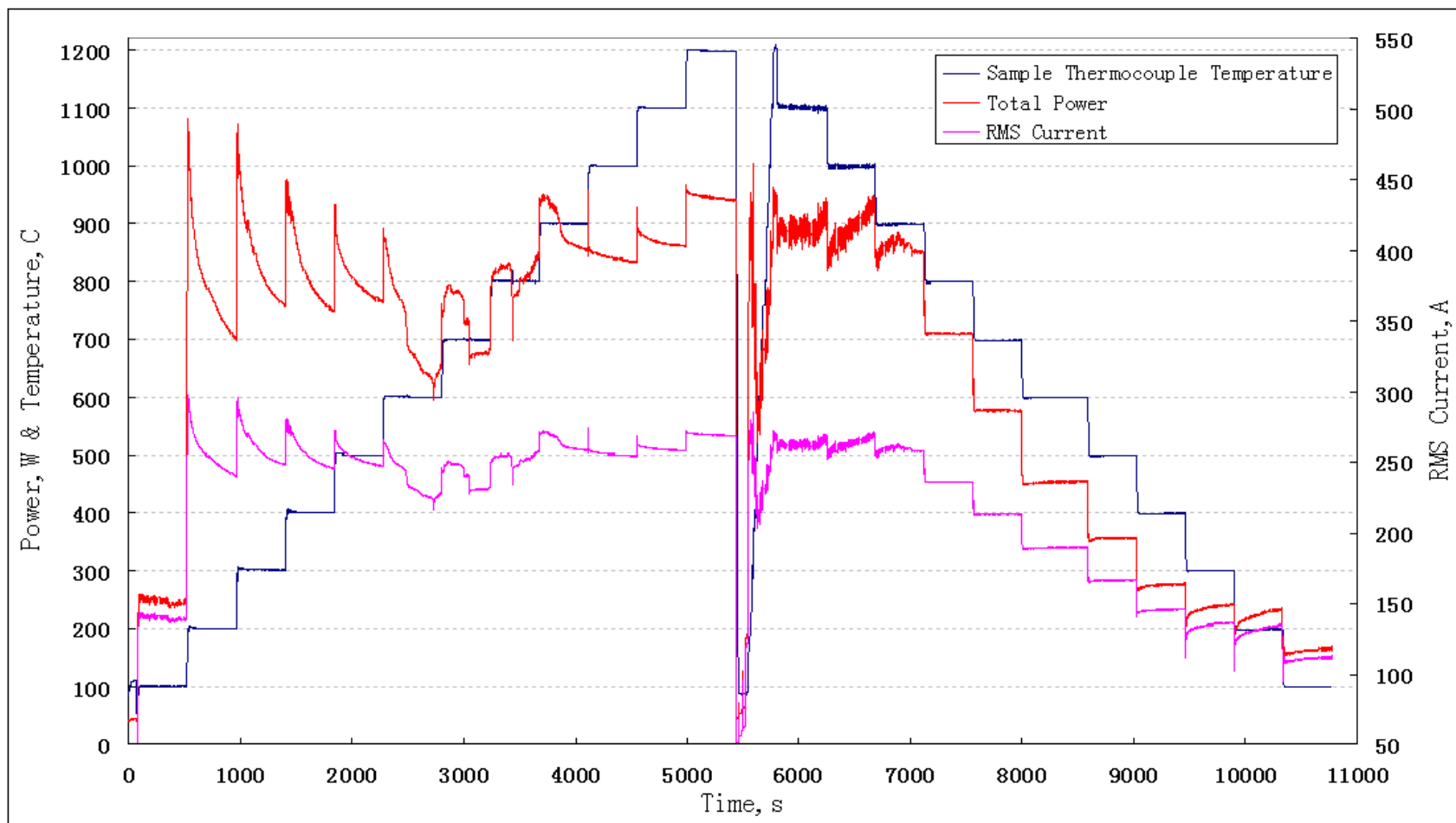
Fig. A-7 Measured RMS Current and Sample Thermocouple Temperature for Case 7
(Wet Experiment, Y=18mm, WaterFlowRate=2.5lpm)
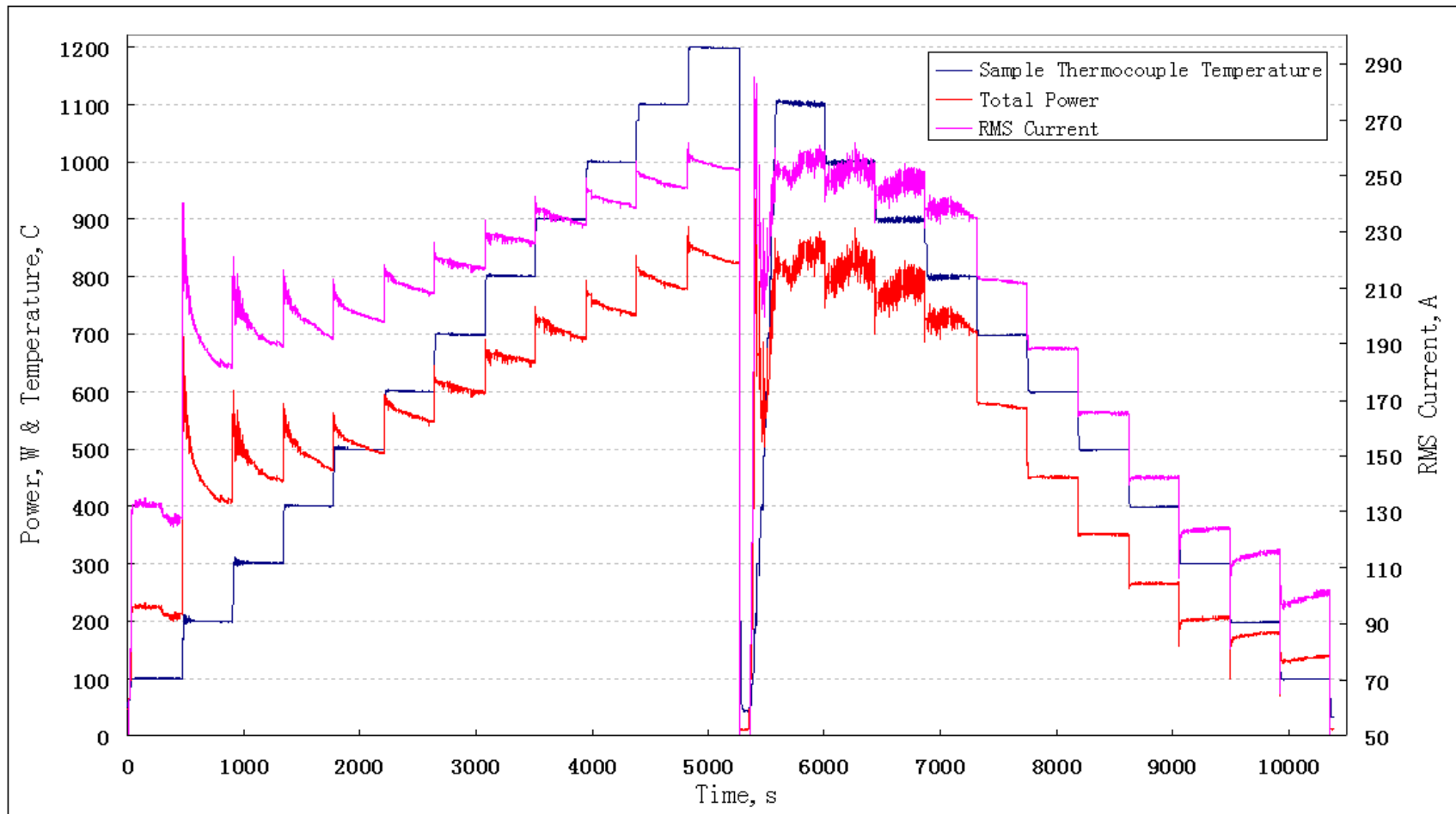
Fig. A-8 Measured RMS Current and Sample Thermocouple Temperature for Case 8
(Wet Experiment, Y=18mm, WaterFlowRate=4.6lpm)

Appendix B

B. Input and Output Modeling Results for Wet Experiments.

	Ts	I_tot/loop	h_spray	h_front	h_air	h_cw	T_cw	Tcoil	Pspray	Spray heat fllux	Pfront	Tsurf_min	Tsurf_max
					Input					*Output*			
Unit	C	A	kW/m^2K	kW/m^2K	W/m^2K	10kW/m^2K	C	C	W	MW/m^2	W	C	C
Heat	100	256.4	16.50	4	10	3.49	30	33	55	1.09	2	83	96
	200	393.4	17.80	4	10	3.60	34	36	137	2.73	4	159	190
	300	415.8	12.50	4	10	3.66	35	41	157	3.13	5	253	289
	400	417.4	9.20	4	10	3.68	36	41	161	3.20	7	348	385
	500	419.1	7.20	4	10	3.66	35	41	163	3.24	9	449	487
	600	419.4	5.90	4	10	3.66	36	41	164	3.26	11	549	587
	700	417.1	4.90	4	10	3.69	37	41	161	3.20	12	649	686
	800	411.1	4.05	4	10	3.71	36	41	155	3.09	14	750	784
	900	393.5	3.10	4	10	3.69	36	41	136	2.71	17	857	885
	1000	415.6	3.10	4	10	3.69	35	41	152	3.03	20	954	985
	1100	418.2	2.73	4	10	3.65	37	41	148	2.95	23	1053	1082
	1200	436.9	2.70	4	10	3.68	36	41	161	3.20	26	1150	1182
Cool	1100	431.2	3.00	4	10	3.69	36	41	162	3.22	23	1047	1078
	1000	413.3	3.05	4	10	3.68	36	41	149	2.97	19	955	985
	900	398.4	3.20	4	10	3.66	35	40	140	2.79	16	857	886
	800	385.9	3.42	4	10	3.65	35	39	132	2.63	14	758	787
	700	362.1	3.40	4	10	3.66	35	39	114	2.27	12	663	688
	600	328.6	3.16	4	10	3.63	35	38	91	1.81	10	572	592
	500	297.9	3.05	4	10	3.60	34	37	72	1.43	8	478	494
	400	277.4	3.34	4	10	3.58	33	35	62	1.23	6	382	396
	300	260.9	4.05	4	10	3.56	33	35	55	1.09	5	284	297
	200	261.4	6.70	4	10	3.54	32	35	56	1.11	4	182	196
	100	203.7	9.50	4	10	3.50	31	34	33	0.66	2	90	98

Table B.1 Input and Output Data for Modeling Experiment with Nozzle Operating Conditions: Water flow rate=2.5lpm; Air flow rate=125lpm; Y=0mm (Case2)

Unit	Ts	I_tot/loop	h_spray	h_front	h_air	h_cw	T_cw	Tcoil	Pspray	Spray heat fllux	Pfront	Tsurf_min	Tsurf_max
							Input			Output			
	C	A	kW/m^2K	kW/m^2K	W/m^2K	W/m^2K	C	C	W	MW/m^2	W	C	C
Heat	100	292.5	23.00	5	10	3.59	29	36	72	1.43	2	77	93
	200	443.7	24.20	5	10	3.75	34	39	176	3.50	4	148	185
	300	472.3	17.20	5	10	3.81	37	39	207	4.12	6	236	282
	400	487.1	13.30	5	10	3.78	36	40	225	4.48	7	330	380
	500	489.4	10.50	5	10	3.83	37	40	231	4.60	9	427	480
	600	481.0	8.25	5	10	3.84	38	40	224	4.46	11	530	580
	700	452.0	5.97	5	10	3.80	37	39	195	3.88	13	639	683
	800	454.4	5.22	5	10	3.84	38	40	197	3.92	15	737	780
	900	436.1	4.08	5	10	3.76	36	40	176	3.50	17	843	880
	1000	447.1	3.80	5	10	3.82	37	40	183	3.64	20	940	977
	1100	450.8	3.37	5	10	3.79	36	40	182	3.62	24	1045	1080
	1200	466.9	3.27	5	10	3.80	37	40	193	3.84	27	1141	1178
Cool	1100	463.2	3.65	5	10	3.85	38	42	195	3.88	24	1038	1077
	1000	445.8	3.76	5	10	3.73	37	42	182	3.62	20	943	980
	900	429.7	3.92	5	10	3.77	38	42	170	3.38	17	846	882
	800	452.4	5.17	5	10	3.34	38	42	195	3.88	15	737	780
	700	441.0	5.62	5	10	3.32	37	42	184	3.66	13	642	683
	600	423.2	6.03	5	10	3.34	38	42	167	3.32	11	547	585
	500	384.3	5.83	5	10	3.28	36	42	134	2.67	9	458	488
	400	354.6	6.15	5	10	3.25	35	40	111	2.21	7	366	392
	300	342.8	7.92	5	10	3.23	34	37	103	2.05	5	267	292
	200	356.6	14.20	5	10	3.24	35	37	111	2.21	4	165	190
	100	253.5	15.90	5	10	3.17	33	37	53	1.05	2	84	96

Table B.2 Input and Output Data for Modeling Experiment with Nozzle Operating Conditions: Water flow rate=3.5lpm; Air flow rate=95lpm; Y=0mm (Case 3)

		Input							Output				
	Ts	I_tot/loop	h_spray	h_front	h_air	h_cw	T_cw	Tcoil	Pspray	Spray heat fllux	Pfront	Tsurf_min	Tsurf_max
Unit	C	A	kW/m^2K	kW/m^2K	W/m^2K	10kW/m^2K	C	C	W	MW/m^2	W	C	C
Heat	100	304.6	24.80	5.5	10	2.87	27	30	78	1.55	1	78	94
	200	459.4	26.40	5.5	10	2.99	33	39	190	3.78	4	145	184
	300	486.1	18.20	5.5	10	3.09	36	43	220	4.38	6	235	284
	400	484.1	13.10	5.5	10	3.09	38	44	222	4.42	8	330	381
	500	496.9	10.90	5.5	10	3.03	38	44	238	4.74	10	424	478
	600	486.3	8.50	5.5	10	3.03	38	44	229	4.56	11	525	577
	700	484.6	7.10	5.5	10	2.96	37	44	229	4.56	14	627	677
	800	474.9	5.83	5.5	10	2.96	37	44	218	4.34	16	730	777
	900	456.0	4.57	5.5	10	2.96	37	44	196	3.90	18	838	880
	1000	464.5	4.20	5.5	10	2.87	38	44	202	4.02	21	935	977
	1100	473.9	3.87	5.5	10	2.79	37	44	207	4.12	25	1037	1078
	1200	480.9	3.56	5.5	10	2.81	37	44	209	4.16	28	1135	1175
Cool	1100	469.2	3.78	5.5	10	2.81	37	44	202	4.02	25	1035	1075
	1000	459.4	4.07	5.5	10	2.80	37	44	196	3.90	21	937	978
	900	454.4	4.55	5.5	10	2.74	37	44	195	3.88	18	835	877
	800	479.4	5.98	5.5	10	2.77	38	44	223	4.44	16	727	777
	700	474.3	6.75	5.5	10	2.75	37	44	218	4.34	14	629	678
	600	450.5	7.05	5.5	10	2.76	38	44	193	3.84	11	537	580
	500	415.3	7.06	5.5	10	2.72	37	42	160	3.18	9	448	485
	400	392.5	7.82	5.5	10	2.72	36	42	140	2.79	8	358	392
	300	372.9	9.70	5.5	10	2.69	35	42	124	2.47	6	260	288
	200	355.0	14.00	5.5	10	2.62	34	39	110	2.19	4	165	191
	100	260.7	17.00	5.5	10	2.62	32	39	57	1.13	2	83	96

Table B.3 Input and Output Data for Modeling Experiment with Nozzle Operating Conditions: Water flow rate=4.6lpm; Air flow rate=104lpm; Y=0mm (Case 4)

Unit	Ts	Input							Output				
		l_tot/loop	h_spray	h_front	h_air	h_cw	T_cw	Tcoil	Pspray	Spray heat fllux	Pfront	Tsurf_min	Tsurf_max
Unit	C	A	kW/m^2K	kW/m^2K	W/m^2K	10kW/m^2K	C	C	W	MW/m^2	W	C	C
Heat	100	227.2	12.30	4	10	3.47	28	35	42	0.84	2	89	99
	200	373.1	15.70	4	10	3.57	31	37	122	2.43	3	163	191
	300	395.5	11.10	4	10	3.63	33	38	141	2.81	5	257	290
	400	401.9	8.35	4	10	3.66	34	38	148	2.95	7	354	388
	500	404.0	6.60	4	10	3.67	34	38	150	2.99	8	453	483
	600	403.6	5.40	4	10	3.68	35	38	150	2.99	10	550	584
	700	373.6	3.70	4	10	3.66	34	38	123	2.45	12	659	687
	800	359.7	2.82	4	10	3.64	34	38	110	2.19	14	765	788
	900	373.1	2.66	4	10	3.64	33	38	117	2.33	16	864	888
	1000	377.6	2.34	4	10	3.65	34	38	116	2.31	19	965	988
	1100	405.1	2.48	4	10	3.66	34	38	135	2.69	22	1057	1083
	1200	418.7	2.36	4	10	3.68	35	38	142	2.83	26	1160	1187
Cool	1100	412.0	2.61	4	10	3.67	34	38	142	2.83	22	1055	1083
	1000	405.4	2.89	4	10	3.68	35	38	142	2.83	19	957	985
	900	391.8	3.06	4	10	3.67	34	38	134	2.67	16	857	886
	800	376.1	3.18	4	10	3.65	34	38	123	2.45	14	763	788
	700	338.5	2.82	4	10	3.62	33	38	95	1.89	12	671	691
	600	300.3	2.47	4	10	3.58	32	36	71	1.41	10	577	592
	500	263.5	2.17	4	10	3.54	30	36	52	0.88	8	484	495
	400	242.4	2.33	4	10	3.51	30	32	44	0.82	6	386	396
	300	230.5	2.94	4	10	3.49	29	31	41	0.82	4	288	298
	200	227.7	4.80	4	10	3.48	29	31	41	0.82	3	187	197
	100	187.9	7.70	4	10	3.46	28	31	28	0.56	1	92	99

Table B.4 Input and Output Data for Modeling Experiment with Nozzle Operating Conditions: Water flow rate=2.5lpm; Air flow rate=125lpm; Y=9mm (Case5)

	Ts	Input							Output				
		I_tot/loop	h_spray	h_front	h_air	h_cw	T_cw	Tcoil	Pspray	Spray heat fllux	Pfront	Tsurf_min	Tsurf_max
Unit	C	A	kW/m^2K	kW/m^2K	W/m^2K	10kW/m^2K	C	C	W	MW/m^2	W	C	C
Heat	100	258.9	17.00	5.5	10	3.52	29	30	56	1.11	1	82	95
	200	415.6	20.50	5.5	10	3.68	33	35	154	3.07	4	154	188
	300	447.8	14.90	5.5	10	3.78	36	41	185	3.68	6	245	288
	400	444.2	10.68	5.5	10	3.81	37	40	184	3.66	7	340	383
	500	441.1	8.12	5.5	10	3.82	37	41	183	3.64	9	443	486
	600	436.1	6.47	5.5	10	3.82	37	41	180	3.58	11	544	585
	700	422.4	5.03	5.5	10	3.81	37	41	166	3.30	12	647	685
	800	434.1	4.62	5.5	10	3.82	37	41	177	3.52	14	745	784
	900	439.0	4.14	5.5	10	3.83	37	41	180	3.58	17	842	881
	1000	447.9	3.80	5.5	10	3.82	37	41	185	3.68	20	941	979
	1100	420.2	2.74	5.5	10	3.81	37	41	150	2.99	23	1052	1082
	1200	434.4	2.62	5.5	10	3.82	37	41	157	3.13	28	1153	1182
Cool	1100	437.9	3.09	5.5	10	3.81	37	41	167	3.32	24	1048	1082
	1000	409.0	2.94	5.5	10	3.79	36	41	144	2.87	20	955	983
	900	391.7	3.03	5.5	10	3.76	36	39	133	2.65	17	858	886
	800	379.4	3.24	5.5	10	3.74	35	39	126	2.51	14	759	786
	700	382.0	3.88	5.5	10	3.72	34	39	130	2.59	12	658	688
	600	357.2	3.90	5.5	10	3.72	34	39	112	2.23	10	566	592
	500	329.6	3.94	5.5	10	3.70	33	37	93	1.85	8	472	493
	400	312.3	4.50	5.5	10	3.65	32	36	83	1.65	6	375	394
	300	305.5	6.00	5.5	10	3.64	32	36	80	1.59	5	275	294
	200	307.8	9.90	5.5	10	3.63	32	36	81	1.61	3	175	194
	100	228.5	12.70	5.5	10	3.57	30	36	43	0.86	2	85	96

Table B.5 Input and Output Data for Modeling Experiment with Nozzle Operating Conditions: Water flow rate=4.6lpm; Air flow rate=104lpm; Y=9mm (Case6)

Unit	Ts	Input							Output				
		I_tot/loop	h_spray	h_front	h_air	h_cw	T_cw	Tcoil	Pspray	Spray heat fllux	Pfront	Tsurf_min	Tsurf_max
Unit	C	A	kW/m^2K	kW/m^2K	W/m^2K	10kW/m^2K	C	C	W	MW/m^2	W	C	C
Heat	100	180.5	7.22	4	10	3.43	27	28	25	0.50	1	91	97
	200	257.9	6.42	4	10	3.47	29	29	54	1.07	3	184	197
	300	268.0	4.32	4	10	3.50	30	29	58	1.15	5	283	297
	400	272.5	3.20	4	10	3.50	29	29	59	1.17	6	381	394
	500	280.3	2.58	4	10	3.52	30	29	61	1.21	8	481	494
	600	294.2	2.32	4	10	3.52	30	29	67	1.33	10	579	593
	700	307.0	2.12	4	10	3.53	30	29	72	1.43	12	679	693
	800	319.7	1.99	4	10	3.55	31	29	78	1.55	14	774	789
	900	328.7	1.80	4	10	3.56	31	29	80	1.59	16	875	890
	1000	337.9	1.62	4	10	3.58	32	29	81	1.61	19	977	992
	1100	347.6	1.47	4	10	3.60	32	29	82	1.63	23	1071	1089
	1200	356.7	1.32	4	10	3.62	33	31	82	1.63	27	1162	1188
Cool	1100	361.7	1.70	4	10	3.61	33	36	94	1.87	23	1070	1087
	1000	354.5	1.92	4	10	3.61	33	36	95	1.89	20	969	987
	900	351.2	2.22	4	10	3.64	34	38	98	1.95	17	867	888
	800	332.6	2.24	4	10	3.60	32	37	87	1.73	14	772	790
	700	299.2	1.96	4	10	3.58	32	37	67	1.33	12	681	694
	600	265.9	1.71	4	10	3.55	31	36	50	1.00	10	585	595
	500	233.6	1.49	4	10	3.52	30	32	36	0.72	8	491	498
	400	201.3	1.32	4	10	3.49	29	31	25	0.50	6	393	398
	300	175.4	1.35	4	10	3.49	28	31	19	0.38	4	292	296
	200	163.9	2.04	4	10	3.45	28	30	18	0.36	3	193	197
	100	143.2	4.14	4	10	3.43	27	29	15	0.30	1	94	98

Table B.6 Input and Output Data for Modeling Experiment with Nozzle Operating Conditions: Water flow rate=2.5lpm; Air flow rate=125lpm; Y=18mm (Case7)

	Ts	Input							Output				
		I_tot/loop	h_spray	h_front	h_air	h_cw	T_cw	Tcoil	Pspray	Spray heat fllux	Pfront	Tsurf_min	Tsurf_max
Unit	C	A	kW/m^2K	kW/m^2K	W/m^2K	10kW/m^2K	C	C	W	MW/m^2	W	C	C
Heat	100	195.4	8.68	5.5	10	3.39	26	27	30	0.60	1	88	97
	200	340.0	12.48	5.5	10	3.50	29	32	100	1.99	3	169	193
	300	351.3	8.34	5.5	10	3.55	31	34	109	2.17	5	267	292
	400	347.5	5.86	5.5	10	3.58	32	34	107	2.13	6	367	392
	500	349.8	4.61	5.5	10	3.57	32	36	107	2.13	8	465	490
	600	321.2	2.95	5.5	10	3.56	31	36	85	1.69	10	574	592
	700	327.2	2.54	5.5	10	3.56	31	36	87	1.73	12	674	692
	800	363.5	2.88	5.5	10	3.60	32	36	113	2.25	14	764	788
	900	365.4	2.48	5.5	10	3.62	33	36	111	2.21	16	867	888
	1000	359.9	2.00	5.5	10	3.62	33	37	101	2.01	19	968	987
	1100	365.1	1.74	5.5	10	3.62	33	37	98	1.95	22	1071	1088
	1200	380.2	1.68	5.5	10	3.64	33	37	104	2.07	26	1168	1187
Cool	1100	376.1	1.93	5.5	10	3.62	33	37	108	2.15	22	1067	1087
	1000	380.6	2.39	5.5	10	3.62	33	37	119	2.37	19	961	984
	900	364.1	2.46	5.5	10	3.62	33	37	110	2.19	16	865	888
	800	333.8	2.25	5.5	10	3.59	32	37	89	1.77	14	772	790
	700	301.1	1.98	5.5	10	3.56	31	35	68	1.35	12	680	693
	600	267.2	1.72	5.5	10	3.52	30	35	51	1.02	10	584	594
	500	235.5	1.52	5.5	10	3.49	29	34	37	0.74	8	488	496
	400	206.5	1.42	5.5	10	3.47	28	34	28	0.56	6	392	397
	300	192.3	1.96	5.5	10	3.48	29	33	25	0.50	4	292	297
	200	189.8	3.00	5.5	10	3.45	28	29	26	0.52	3	192	198
	100	157.8	5.20	5.5	10	3.43	27	29	19	0.38	1	93	98

Table B.7 Input and Output Data for Modeling Experiment with Nozzle Operating Conditions: Water flow rate=4.6lpm; Air flow rate=104lpm; Y=18mm (Case8)

References

1. Bryan Petrus, Kai Zheng, X. Zhou, Brian G. Thomas and Joseph Bentsman, "Real-Time Model-Based Spray-Cooling Control System for Steel Continuous Casting", Metallurgical and Materials Transactions B, submitted July, 2009

2. L. Huang, P. Ayyaswamy. "Heat Transfer of A Nuclear Reactor Containment Spray Drop." Nuclear Engineering and Design, 101 (1987), 137-148.

3. P. Lemaitre, E. Porcheron. "Study of Heat and Mass Transfer in A Spray for Containment Application: Analysis of the Influence fo the Spray Mass Flow Rate." Nuclear Engineering and Design, Volume 239, Issue 3, 2009, pp: 541-550.

4. R. Clift, J. R. Grace and M. E. Weber, "Bubbles, Drops and Particles," Academic Press, New York, 1987

5. H. R. Jacobs and D. S. Cook, "Direct Contact Condensation on A Non-circulating Drop," Proc. 6th Intern, Heat Transfer Conf., Vol. 2, Toronto, 1978, pp. 389-393.

6. Y. S. Lou and L. S. Yang, "Quasi-steady Theroy of Non-equilibrium Droplet evaporation and Condensation," J. Appl. Phys. 50 (1978) 5331-5338

7. I. Kh. Rakhmatulina, "Nonsteady Evaporation and Growth of Drops in Gaseous Medium," Intern. J. Engrg. Sci. 19 (1981) 1114-1122

8. J. S. Ford and A. Lekic, "Rate of Growth of Drops During Condensation," Intern. J. Heat Mass Transfer 16 (1973) 61-64

9. E. Kulic, E. Rhodes and G. Sullivan, "Heat Transfer Rate Predictions in Condensation on Droplets from Air-steam Mixture," Can. J. Chem. Engrg. 53 (1975) 252-258

10. J. N. Chung and P. S. Ayyaswamy, "The Effect of Internal Circulation on the Heat Transfer of a Nuclear Reactor Containment Spray Droplet," Nucl. Technol. 47 (1980) 268-281

11. M. Tanaka, "Heat Transfer of a Spray Droplet in A Nuclear Reactor Containment, " Nucl. Technol. 47 (1980) 268-281

12. E. Kulic and E. Rhodes, "Heat Transfer Rates to Moving Droplets in Air-steam Mixtrue," Proc. 6th Intern. Heat Transfer Conf., Toronto, 1978, pp. 464-474

13. S. S. Sadhal and P. S. Ayyaswamy, "Flow past A Liquid Drop with A Large Non-uniform Radial Velocity," J. Fluid Mech. 133 (1983) 65-81

14. J. N. Chung and P. S. Ayyaswamy, "Laminar Condensation Heat and Mass Transfer of a Moving Drop," AIChE J. 27 (1981) 372-377

15. H. Anglart, F. Alavyoon, R. Novarini. "Study of Spray Cooling of a Pressure Vessel Head of a Boiling Water Reactor." Nuclear Engineering and Design (In press).

16. http://ccc.illinois.edu/introduction/concast.html

17. F. McGinnis, J. Holman, "Individual Droplet Heat Transfer Rates for Splattering on Hot Surfaces." Int. J. Heat Mass Transfer, Vol 12, 1969, pp. 95-108.

18. C. Pedersen, Int. J. Heat and Mass Transfer, Vol. 13, 1970, pp. 369-379.

19. L. Wachters, N. Westerling, "The Heat Transfer from a Hot Wall to Impinging Water Drops in the Spheroidal State." Chem, Eng. Sc., Vol. 21, 1966, pp1047-1056.

20. K. Choi, S. Yao, "Mechanisms of Film Boiling Heat Transfer of Normally Impacting Spray." Int, J. Heat Mass Transfer, Vol. 30, 1987, pp.311-318

21. N. Sozbir, Y, Chang, S. Yao, Trans, ASME, Vol. 125, 2003, pp. 71-74.

22. G. Guido Lavalle, P. Carrica, V. Garea and M. Jaime, "A Boiling Heat Transfer Paradox," Am. J. Phys. Vol. 60(7), 1992, pp. 593-597

23. Y. Buyevich, and V. Mankevich, "Cooling of a. Superheated Surface with a Jet Mist Flow." Int. J. Heat Mass Transfer, Vol. 38, 1995, pp. 731-744.

24. N. Hatta, H. Fujimoto, R Ishii and J-i. Kodado, "Analytical Study of Gas-Particle Two-Phase Free Jets Exhausted from a Subsonic Nozzle." ISIJ Int., Vol. 31, 1991, pp. 53-61

25. N. Hatta, H Fujimoto and R Ishiim ISIJ Int., "Numerical Analysis of a Gas-Particle Subsonic Jet Impinging on a Flat Plate." Vol. 31, 1991, pp. 342-349.

26. R. Issa and S. Yao, "A Numerical Model for Spray-Wall Impactions and Heat Transfer at Atmospheric Conditions." J. Thermophysics and Heat Transfer, Vol. 19, 2005, pp. 441-447.

27. I. Hernandez, F. Acosta, A. Castillejos and J. Minchaca, "The Fluid Dynamics of Secondary Cooling Air-Mist Jets." Metall. Trans, B, Vol. 39, 2008, pp. 746-763.

28. M. Shimada and M. Mitsutsuka, "On Heat Transfer Coefficient by Forced Water Cooling to Carbon Steel," Tetsu-to-Hagane, vol. 52, 1966, pp. 1643

29. T. Nozaki, J.I. Matsuno, K. Murata, H. Ooi, and M. Kodama: Trans. Iron Steel Inst. Jpn., 1978, vol. 18 (6), pp. 330–338.

30. J.K. Brimacombe, P.K. Agarwal, S. Hibbins, B. Prabhakar, and L.A. Baptista: in *Continuous Casting Vol. II: Heat Flow, Solidification and Crack Formation*, J.K. Brimacombe, I.V. Samarasekera, and J.E. Lait, eds., ISS-AIME, Warrendale, PA, 1984, pp. 109–2

31. J. Sengupta, B.G. Thomas and M. A. Wells, "The Use of Water Cooling during the Continuous Casting of Steel and Aluminum Alloys," Metall. Mat. Trans. A. vol. 36(1), 2005. pp 187-204

32. H. Yu, "Method of Preventing Cracking in Direct Chill Cast Ingots," United States Patent, Patent No.: 7152662B2, Patent Date: Dec 26, 2006

33. K. Choi and S. Yao, "Mechanisms of Film Boiling Heat Transfer of Normally Impacting Spray." Int. J. Heat and Mass Transfer 30 (1987) 311-318.

34. E. Mizikar, "Spray Cooling Investigation for Continuous Casting of Billets and Blooms." Iron Steel Enging, June, 53-70 (1970).

35. M. Ciofalo, I. Piazza, and V. Brucato, "Investigation of the Cooling of Hot Walls by Liquid Water Sprays." Int. J. Heat Mass Transfer, 42, pp. 1157-1175, (1999).

36. H. Al-Ahamdi and S. Yao, "Experimental Study of the Spray Cooling of High Temperature Metal Using Full Cone Industrial Sprays."
www.spray.com/applications/steel_pdf/exp_study_full-cone.pdf

37. C. Dodd and W. Deeds, "Analytical Solutions to Eddy-current Probe-Coil Problems." Journal of Applied Physics, Vol. 39(6), 1968, pp. 2829-2838.

38. J. Donea, S. Giuliani and A. Philippe, "Finite Elements in the Solution of Electromagnetic Induction Problems." Int. J. Num. Mech. Eng., 8, 359-367 (1974).

39. M. Chari, "Finite Element Solution of the Eddy-current Problem in Magnetic Structures." IEEE Trans. PAS-93(1), 62 (1973).

40. G. Meunier, D. Shen and J. Coulomb, "Modelisation of 2D and Axisymmetric Magnetodynamic Domain by the Finite Element Method." IEEE Trans. Magnetics, 24 (1), 166-169 (1958).

41. R. Baker, "Classical Heat Flow Problems Applied to Induction Billet Heating." AIEE Trans., 77, 106-112, May (1958).

42. Ch. Marchand and A. Foggia, "2D Finite Element Program for Magnetic Induction Heating." IEEE Trans. Vol. MAG-19 (6), Nov (1983).

43. K. Wang, S. Chandrasekar and H. Yang, "Finite Element Simulation of Induction Heating Treatment." Journal of Materials Engineering and Performance, Vol. 1(1), 1992, pp. 97-112.

44. C. Chaboudez, S. clain, R. Glardon, D. Mari, J. Rappaz and M. Swierkosz, "Numerical Modeling in Induction Heating for Axisymmetric Geommetries." IEEE Trans. Vol. 33(1), 1997, pp. 739-745.

45. R. Jafrai-Shapoorabdi, A. Konrad and A. Sinclair, "Comparison of Three Formulations for Eddy-Current and Skin Effect Problems." IEEE Trans., Vol. 38(2), 2002, pp. 617-620.

46. H. Kim, J, Jung, K. Park, C, Im and H. Jung, "Efficient Technique for 3-D Finite Element Analysis of Skin Effect in Current-Carrying Conductors." IEEE Trans., Vol. 40(2), 2004, pp. 1326-1329.

47. http://www.ansys.com/

48. http://www.comsol.com/

49. A. F. Mills, "Heat Transfer," Second Edition, Section 7.4, Prentice Hall, Upper Saddle River, New Jersey 07458

50. Sami Vapalahti, Humberto Castillejos, Andres Acosta, Brian G. Thomas and Seppo Louhenkilpi, "Modeling of CC Secondary Cooling Sprays: An Experimental Study." Continuous Casting Consortium Annual Report, June, 2006

51. J. Walker, "Boiling and the Leidenfrost Effect", www.wiley.com

52. Sami Vapalahti, Humberto Castillejos, Andres Acosta, Brian G. Thomas and Seppo Louhenkilpi, "Delavan Nozzle Characterization at CINVESTAV," Continuous Casting Consortium Report, 2007

53. J. Jackson, "Classical Electrodynamics," 3rd Edition, Wiley Press, 2004.

54. L.C. Burmesiter: Convective Heat Transfer, 2 ed., Wiley, New York, 1993, p. 484

55. http://www.platinummetalsreview.com/jmpgm/data/datasheet.do?record=1219&database=cesdatabase&showGraphs=#Electrical%20Conductivity%20v%20Temperature

56. P.D. Foote, "The Total Emissivity of Platinum and the Relation between Total Emissivity and Resistivity", 1914.

57. A.H. Sully, E.A. Brandes, R.B. Waterhouse, "Some Measurements of the Total Emissivity of Metals and Pure Refractory Oxides and the Variation of Emissivity with Temperature," Oct, 1952.

58. D. Bradley, A.G. Entwistle, "Determination of the Emissivity, for Total Radiation, of Small Diameter Platinum-10% Rhodium Wires in the Temperature Range 600-1450 ^{o}C," Aug 1961.

59. L.N. Aksyutov, "Normal Spectral Emissivity of Gold, Platinum, and Tungsten," 1974.

60. H. Jehn, "Platinum Losses During High Temperature Oxidization," 1981.

61. G. Neuer, G. Jaroma-Weiland, "Spectral and Total Emissivity of High-Temperature Materials ," 1998.

62. W. Sabuga, R. Todtenhaupt, "Effect of Roughness on the Emissivity of the Precious Metals Silver, Gold, Palladium, Platinum, Rhodium and Iridium," High Temperature-High Pressure, 2001, vol. 33, pp. 261-169.

63. AC/DC Module, Model Library, COMSOL Multiphysics 3.5, pp. 19

64. "Couple-Field Analysis Guide," ANSYS Release 9.0 Documentation

65. A. F. Mills, "Heat Transfer," Second Edition, Section 4.4, Prentice Hall, Upper Saddle River, New Jersey 07458

66. Y. Meng and B. G. Thomas, "Heat Transfer and Solidification Model of Continuous Slab Casting: CON1D," Metallurgical & Materials Transactions, Vol. 34B, No. 5, Oct. 2003, pp. 685-705

Author's Biography

Xiaoxu Zhou was born on November 08, 1983 in Anhui, China. He obtained his Bachelor's degree in the Department of Modern Physics at the University of Science and Technology of China (USTC) in 2007. After graduating from USTC, he continued his study in the Nuclear, Plasma and Radiological Engineering Department (NPRE) at University of Illinois at Urbana-Champaign (UIUC). During August 2007 ~ December 2007, he worked as a teaching assistant in NPRE. After that, he obtained a research assistant position in Professor Brian G. Thomas' laboratory. Under the direction of Professor Thomas, he has worked on heat transfer during spray water cooling using induction heating and improving the comprehensive continuous casting code CON1D. In December 2009, he will obtain his Master's degree in the Nuclear Engineering. following the completion of his M.S., he will continue to work with Professor Thomas on his PhD in Mechanical Engineering.